

Spring 2009

# Chasing $\mu$

Joseph P. Cannon  
*Louisiana Tech University*

Follow this and additional works at: <https://digitalcommons.latech.edu/dissertations>

 Part of the [Electrical and Computer Engineering Commons](#), and the [Polymer Chemistry Commons](#)

---

## Recommended Citation

Cannon, Joseph P., "" (2009). *Dissertation*. 483.  
<https://digitalcommons.latech.edu/dissertations/483>

This Dissertation is brought to you for free and open access by the Graduate School at Louisiana Tech Digital Commons. It has been accepted for inclusion in Doctoral Dissertations by an authorized administrator of Louisiana Tech Digital Commons. For more information, please contact [digitalcommons@latech.edu](mailto:digitalcommons@latech.edu).

**CHASING  $\mu$**

by

Joseph P. Cannon, B. S.

A Dissertation Presented in Partial Fulfillment  
of the Requirements for the Degree  
Doctor of Philosophy

COLLEGE OF ENGINEERING AND SCIENCE  
LOUISIANA TECH UNIVERSITY

May 2009

UMI Number: 3358253

### INFORMATION TO USERS

The quality of this reproduction is dependent upon the quality of the copy submitted. Broken or indistinct print, colored or poor quality illustrations and photographs, print bleed-through, substandard margins, and improper alignment can adversely affect reproduction.

In the unlikely event that the author did not send a complete manuscript and there are missing pages, these will be noted. Also, if unauthorized copyright material had to be removed, a note will indicate the deletion.

UMI<sup>®</sup>

---

UMI Microform 3358253  
Copyright 2009 by ProQuest LLC  
All rights reserved. This microform edition is protected against  
unauthorized copying under Title 17, United States Code.

---

ProQuest LLC  
789 East Eisenhower Parkway  
P.O. Box 1346  
Ann Arbor, MI 48106-1346

LOUISIANA TECH UNIVERSITY

THE GRADUATE SCHOOL

4/24/2009

Date

We hereby recommend that the dissertation prepared under our supervision  
by Joseph Cannon

entitled Chasing  $\mu$

be accepted in partial fulfillment of the requirements for the Degree of  
Doctorate of Philosophy in Engineering



Supervisor of Dissertation Research

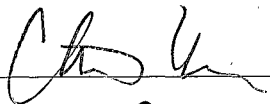


Head of Department

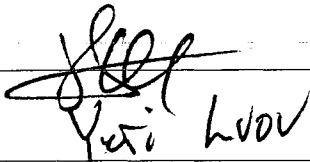
Department

Recommendation concurred in:

Sandra Selmic



Advisory Committee



Approved:

  
Director of Graduate Studies

Approved:

  
Dean of the Graduate School

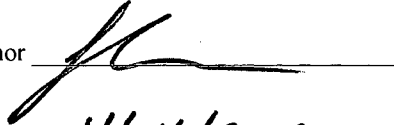
  
Dean of the College

## APPROVAL FOR SCHOLARLY DISSEMINATION

The author grants to the Prescott Memorial Library of Louisiana Tech University the right to reproduce, by appropriate methods, upon request, any or all portions of this Dissertation. It is understood that "proper request" consists of the agreement, on the part of the requesting party, that said reproduction is for his personal use and that subsequent reproduction will not occur without written approval of the author of this Dissertation. Further, any portions of the Dissertation used in books, papers, and other works must be appropriately referenced to this Dissertation.

Finally, the author of this Dissertation reserves the right to publish freely, in the literature, at any time, any or all portions of this Dissertation.

Author



Date

4/24/2009

## ABSTRACT

Conducting and semiconducting,  $\pi$ -conjugated polymers are promising materials for micro- and nano-optoelectronic applications because of their widely tunable physical, electrical, and optical properties. These polymers have been used to fabricate a number of electronic devices including field-effect transistors, light-emitting diodes, and photovoltaic cells. However, widespread commercial application of these devices has yet to be realized, due in part to poor electronic transport characteristics and device degradation.

Nanostructuring of conjugated polymers by various methods has demonstrated marked improvements in molecular ordering and electronic transport. In this research, nanoscale, tubular structures of semiconducting polymers fabricated by template wetting nanofabrication procedures are explored. In particular, confinement-induced effects on the electronic carrier transport property mobility,  $\mu$ , were investigated for both highly ordered and amorphous polymers. Analysis of space-charge-limited currents provided the key means of monitoring transport characteristics and molecular order. The effects of chemical filtration, nanotube diameter, solvent selection, and temperature are examined in detail.

## TABLE OF CONTENTS

ABSTRACT .....	iv
LIST OF TABLES .....	viii
LIST OF FIGURES.....	ix
ACKNOWLEDGMENTS.....	xii
CHAPTER 1 INTRODUCTION .....	1
CHAPTER 2 LITERATURE REVIEW .....	7
Organic Electronics.....	8
Carrier Transport in Organic Materials.....	8
Device Physics .....	10
Nanostructuring of Organic Materials .....	18
Electrospinning .....	19
Template Synthesis .....	23
Template Wetting.....	25
CHAPTER 3 EXPERIMENTAL METHODS.....	28
Materials.....	28
Wetting of Nanoporous Alumina with Polymer Solutions .....	30
Electronic Devices .....	35
Electrical Testing .....	38
Ultraviolet-Visible Spectroscopy .....	39
CHAPTER 4 CONFINEMENT-INDUCED ENHANCEMENT OF HOLE MOBILITY IN MEH-PPV.....	41

Introduction .....	41
Experimental .....	43
Materials.....	43
Methods.....	44
Results and Discussion.....	48
Conclusions .....	54
<b>CHAPTER 5 SOLVENT EFFECTS ON SOLUTION-BASED TEMPLATE WETTING FABRICATION WITH SEMICONDUCTING POLYMERS.....</b>	<b>55</b>
Introduction.....	55
Experimental .....	57
Materials.....	57
Methods.....	57
Device Model.....	60
Results and Discussion.....	61
Electrical Characterization.....	61
Ultraviolet-Visible Spectroscopy.....	67
Solubility Analysis.....	68
Conclusions .....	76
<b>CHAPTER 6 SOXHLET EXTRACTION OF POLYTHIOPHENE FOR IMPROVED POLYMER PURITY FOR NANOTUBE FABRICATION .....</b>	<b>79</b>
Introduction.....	79
Experimental .....	81
Materials.....	81
Methods.....	82
Results and Discussion.....	84

Soxhlet Extraction.....	84
Electrical Characterization.....	88
Conclusion .....	91
CHAPTER 7 CONCLUSION .....	93
Future Work .....	95
APPENDIX SAMPLE GROUP CONTRIBUTION CALCULATION .....	97
Group Contribution Calculations.....	98
REFERENCES.....	100

## LIST OF TABLES

Table 2.1. Hole mobilities in common semiconducting materials at 300 K. ....	10
Table 2.2. Basic conduction models for semiconducting polymers.....	18
Table 3.1. Nanotube based device area and wall thickness for solution-based template wetting procedures with 2 mg/mL polymer solutions.....	33
Table 5.1. Hole mobility and concentration determined from analysis of space- charge-limited currents in MEH-PPV and P3HT nanotube-based electronic devices. ....	63
Table 5.2. Solubility parameters for MEH-PPV, P3HT, and common solvents.....	72
Table 6.1. Solubility parameters for P3HT and solvents used in the Soxhlet extraction process.....	84
Table 6.2. Percentage of material extracted in each cycle of the Soxhlet extraction procedure for experimental work done here and elsewhere. ....	88
Table 6.3. Hole mobility data for various fractions of P3HT. ....	90
Table A.1. Group contributions to molar mass, molar volume, and cohesive energy following [114]. ....	98

## LIST OF FIGURES

Figure 2.1. Overlapping $p$ orbitals from the $sp^2$ carbons along the conjugated backbone of $trans$ -CH <sub>x</sub> form $\pi$ -bonding and $\pi$ -anti-bonding molecular orbitals, giving rise to two continua of energetic states which the bonding electrons may occupy.....	9
Figure 2.2. Injection barrier heights for thermionic emission models illustrated by example with actual energy levels for MEH-PPV [47] and P3HT [48] with and common contact materials. Values are positive with respect to vacuum. ....	12
Figure 2.3. Ideal J-V characteristics following the formalism of space-charge-limited conduction in a) the absence of and b) the presence of an energetic trap distribution. ....	15
Figure 2.4. Schematic of a typical electrospinning system, following [71]. The circular inset illustrates the use of an alternate capillary which is concentric to the normal nozzle configuration. This setup is described in [74].....	20
Figure 3.1. General chemical structure of a) poly( $p$ -phenylene vinylene) and b) polythiophene, shown with general side chains $R$ . ....	29
Figure 3.2. Illustration of the solution-based template wetting procedure employed throughout this work. The process is illustrated here for a MEH-PPV/chloroform wetting solution. ....	32
Figure 3.3. SEM micrograph of MEH-PPV coated templates a) before and b) after plasma etching to remove residual surface polymer. Figure 3.3b is courtesy of CAMD at LSU Baton Rouge. ....	34
Figure 3.4. SEM imaging of a) MEH-PPV and b) P3HT nanotubes created using solution-based template wetting procedures.....	35
Figure 3.5. The generalized device structure used throughout this work is illustrated in a), while b) illustrates the degree of barrier height minimization due to anode and cathode material choice of Au in the construction of hole-only devices. Gray sections in a) represent the aluminum oxide template, and the squiggly lines represent incorporated polymer. ....	36

Figure 4.1. Molecular structures of a) MEH-PPV, b) PEDOT, and c) the PSS dopant present in conductive PEDOT:PSS.....	44
Figure 4.2. Scanning-electron micrographs of a) a mat of 100 nm MEH-PPV nanotubes, and b) open-ended 100 nm MEH-PPV nanotubes.....	45
Figure 4.3. Device structures for a) hole-only and b) photovoltaic devices constructed from MEH-PPV nanotubes.....	46
Figure 4.4. $J$ - $V$ characteristics observed in hole-only devices fabricated from both 100 nm and 200 nm MEH-PPV nanotubes.....	49
Figure 4.5. Arrhenius behavior of the low-field hole mobility in MEH-PPV nanotubes. ....	51
Figure 4.6. Leading edges of absorption spectra obtained for MEH-PPV in various forms created from a chloroform solution. ....	52
Figure 4.7. Illustration of the photovoltaic fill-factor calculation. ....	53
Figure 4.8. Photocurrent densities observed in MEH-PPV nanotube-based photovoltaic cells. ....	53
Figure 5.1. Scanning electron micrographs of a) MEH-PPV and b)P3HT nanotubes created using template wetting in 100 nm diameter alumina nanopores with chloroform as the solvent for the wetting solution. ....	59
Figure 5.2. Average $J$ - $V$ characteristics for electronic devices fabricated from 100 nm nanotubes of a) MEH-PPV and b) P3HT, created by template wetting using various solvents. Accompanying solid lines represent least-squares-regression fits to (5.3).....	62
Figure 5.3. Internal electric field distributions for a) MEH-PPV and c) P3HT nanotube-based electronic devices operating at 90 V. Corresponding hole concentration distributions for b) MEH-PPV and d) P3HT are also illustrated.....	65
Figure 5.4. Voltage dependent carrier concentration profiles for a) MEH-PPV/THF and b) MEH-PPV/TOL 100 nm nanotube-based electronic devices.....	67
Figure 5.5. Energetic onsets of absorbance spectra for a) MEH-PPV and b) P3HT nanotubes created by template wetting from various solvents. ....	69
Figure 5.6. Ternary representation of the relationship between fractional solubility parameters for MEH-PPV, P3HT, and solvents used here. ....	73
Figure 5.7. Molecular weight dependence of the solvent interaction parameters $\chi_{H,1}$ and $\chi_{H,2}$ for methyl-terminated MEH-PPV (a,c) and P3HT (c,d).....	74

Figure 5.8. Measured hole mobilities in 100 nm nanotube-based electronic devices plotted against solvent interaction parameters calculated using (5.17) and (5.18). Mobilities for MEH-PPV and P3HT plotted versus $\chi_{H,1}$ (a,b) and $\chi_{H,2}$ (c,d). .....	75
Figure 6.1. Examples of the halogenated monomers commonly reacted to produce poly(3-alkylthiophene)s including P3HT. These include a) 3-alkyl-2,5-dibromothiophene [131], b) 2-bromo-5-(bromomagnesio)-3-alkylthiophene [130], and c) 3-alkyl-2,5-diiodothiophene [129]. The side chain, R, is $(\text{CH}_2)_5\text{CH}_3$ for P3HT.....	80
Figure 6.2. Ternary plot illustrating relative locations of extraction solvents and various molecular weights of Me-(3HT) <sub>n</sub> -Me as determined from solubility parameters. ....	85
Figure 6.3. Ternary plots illustrating relative locations of extraction solvents and various molecular weights of a) Br-(3HT) <sub>n</sub> -Br and b) Br-(3HT) <sub>n</sub> -Me as determined from solubility parameters. ....	86
Figure 6.4. Molecular weight dependence of the solvent interaction parameters, a) $\chi_{H,1}$ and b) $\chi_{H,2}$ , for Me-(3HT) <sub>n</sub> -Me.....	87
Figure 6.5. <i>J-V</i> characteristics for nanotube-based electronic devices created with various fractions of P3HT material. Characteristics for devices created using ADS polymer are given for a) 100 nm and b) 200 nm nanotubes. Like characteristics for devices fabricated from polymer obtained from Sigma-Aldrich are provided for c) 100 nm and d) 200 nm nanotubes. Solid lines represent regression fits to (5.3).....	89
Figure 6.6. Hole mobilities for 100 nm and 200 nm nanotube-based electronic devices from various fractions of a) ADS-P3HT and b) SA-P3HT.....	91
Figure A.1. Molecular structure of a P3HT dimer. ....	99

## ACKNOWLEDGMENTS

First, I would like to thank my wife, Thủy, as well as the rest of my family and friends, for their unyielding support while I have been working toward my doctoral degree.

I would also like to extend my thanks to my advisor and mentor, Dr. Scott A. Gold, who has supported me throughout my doctoral research. I would like to thank my committee members Dr. Sandra Selmic and Dr. Pedro Derosa for close collaboration, discussion, and review of the work. Other members of my advisory committee, Dr. Yuri Lvov, and Dr. Chester Wilson, also deserve commendation and gratitude for their support and discussion of the work.

Special thanks needs to be extended to Steven Bearden for his efforts and contributions to some of the experimental work presented herein. I would like to thank Dr. Mangilal Agrawal, Keith Chambers, Fauzia Khatkhatay, Dr. Malcolm Prouty, and Dr. Difei Qi for their guidance, insightful discussion, and review of the work. Further, I cannot forget my fellow group members, past and present, for their advice and assistance in the laboratory. Additionally, the IfM faculty and staff have always been there when needed, and their assistance is greatly appreciated.

## CHAPTER 1

### INTRODUCTION

Since the first reporting of electrically conductive polyacetylene (PA) [1-3], the field of organic electronics has made rapid progress. While conductivities measured in polyacetylene were small, a host of other electronic, organic materials demonstrating far better properties have been synthesized and characterized over the last three decades. For example, electronic transport properties of polythiophene-based systems improved by as much as five orders of magnitude from the first reporting of functional, field-effect transistors in 1986 [4-6]. These advances were due largely to development of synthetic procedures which produced higher levels of regioregularity [7] and purity [8], along with better understandings of charge transport mechanisms as a function of molecular ordering [9].

Conjugated polymers have been demonstrated in a wide range of electronic devices, most notably light-emitting diodes [10-12], photovoltaics [12-14], and thin-film, field-effect transistors [4, 15, 16]. Much of the research interest surrounding these materials has been generated due to their inexpensive processing from solutions at ambient temperatures using techniques such as inkjet printing, spin casting, microstamping, and reel-to-reel fabrication [17, 18]. Due to rapid developmental research activities, commercially viable products from organic electronic materials are beginning to surface, though the extent of their application is narrow [6, 18, 19].

The idea that semiconducting polymers might one day compete head-on with conventional, inorganic materials is overly ambitious. Relatively poor device performance characteristics, along with limited lifetimes and reliability, continue to plague research efforts [6, 18]. However, their viability in niche applications like low-cost, disposable electronics such as radio frequency identification tags and smart cards is more promising [17]. Possibilities for the production of complementary logic from conjugated polymers were often overlooked in the past, due to the belief that most available high quality organic materials were p-type. However, recent work has not only demonstrated successful development of high quality n-type materials [20, 21], but has also shown that many materials commonly thought to be p-type also behave as if n-type when paired with proper electrode materials [22]. Now, with both n- and p-type materials, transistors of either type may be produced, allowing research efforts in organic logic to move forward.

Beyond generic semiconducting devices, the optoelectronic properties of these materials are also finding commercial applications. The potential use of organic light-emitting diodes as backlighting systems for portable electronic devices such as wireless handsets and other personal electronics has received much attention in industrial research [19, 23]. Perhaps the most exciting possibilities lie in what IBM perceives to be their largest potential markets for such devices: inexpensive, flexible flat-panel displays [17] and entertainment headsets [23]. There is little doubt that the commercial potential for these materials is vast, but further progress in device performance is necessary to enable the realization of marketable products.

From a device engineering standpoint, numerous material deficiencies exist for conjugated polymer systems. For the most part, these problems are application specific. For example, contact limited injection properties hinder light-emitting diode efficiencies [24], while high band gaps and narrow absorption bandwidths limit applicability of conjugated polymers in photovoltaics [25]. However, the issue of poor carrier transport properties within the bulk material, namely very low hole and electron mobilities, presents a far more universal problem [26].

Conducting and semiconducting properties of  $\pi$ -conjugated polymers stem from the alternating carbon double bonds along the primary backbone of the molecule. Delocalization of  $\pi$ -electrons allows for electronic transport along the molecule as the  $\pi$ -orbitals overlap, with bonding and anti-bonding orbitals producing molecular valence and conduction wave functions, respectively [27]. The degree of intermolecular orbital overlap can significantly affect carrier transport. It is commonly observed that *intrachain* transport is significantly faster than *interchain* processes where charge carriers must hop between nearest neighbor molecules [6, 9]. Steric effects of side chains added to the  $\pi$ -conjugated backbone, which facilitate solubility in common organic solvents, can further hinder interchain carrier transfers. For example, studies of polythiophenes made soluble by the addition of alkyl groups of various lengths exhibited carrier mobilities that varied inversely with side chain length [28].

Highly regioregular polythiophenes [6, 9] and semiconducting, small molecules like pentacene [29, 30], have demonstrated the highest carrier mobilities commonly observed. These exceptional values are explained by the very high levels of molecular ordering and relatively small intermolecular spacing found in these systems [6, 9]. As

mentioned above, hopping from molecule to molecule is recognized to be the dominant charge transfer mechanism in organic, electronic materials at room temperature. However, research examining the temperature dependence of mobility in highly ordered pentacene suggests that there exists a transition between a thermally activated hopping process which dominates at higher temperatures and a band type process at lower temperatures [29].

The thermally activated nature of the hopping mechanism itself seems to indicate a theoretical upper bound to carrier mobility on the order of  $10 \text{ cm}^2 \text{ V}^{-1} \text{ s}^{-1}$ , due to weak cohesive interactions within conjugated polymer systems [6]. Van der Waals interactions are recognized as the dominant binding forces between molecules, and can be on the order of thermally generated molecular vibrations, causing the material to act *electronically* as though it were in a high-pressure, gaseous phase [31]. These vibrations can interrupt  $\pi$ -orbital overlapping, and make band-type transport nearly impossible because carrier scattering frequency becomes exceedingly high [6].

It is suspected that phase transitions occurring in the material reduce the effect of thermally activated hopping mechanisms, allowing band transport characteristics to become relevant. If organic molecules can be forced into structures in which the molecules are tightly packed, and their vibrational movement is sufficiently constricted, enhancements of mobility should be observed. The present work examines the effects of confinement on conjugated polymers by incorporation into nanoporous aluminum oxide membranes using a template wetting nanofabrication procedure [32].

Chapter 2 gives an overview of the background work related to research and experimental methods presented in this dissertation. Device physics are reviewed with

attention given primarily to the presence of field-dependent mobilities, carrier trapping phenomena, and bulk limited conduction in semiconducting polymers. Further, methods used to measure carrier transport properties, such as mobility, in these materials are reviewed, and key findings are discussed in brief. Different methods for fabricating polymer nanostructures are reviewed with special attention given to those focused on creating nanotubes and nanowires of  $\pi$ -conjugated polymers. In particular, template wetting procedures and the underlying scientific phenomena are discussed in detail.

Chapter 3 details experimental methods used in this work including intricacies of template wetting procedures and device fabrication. Methods used for collection of current-voltage measurements and ultraviolet-visible (UV-Vis) spectroscopy are described, and the mathematical analysis of the space-charge-limited (SCL) currents to obtain values of mobility is explained. Soxhlet extraction processes used in this work as a means of purification for P3HT are also discussed.

Chapter 4 discusses findings related to nanotubes created with a soluble derivative of the commonly studied, optoelectronic polymer poly(phenylene vinylene). Carrier transport in these structures is determined to be space-charge-limited, and low-field mobilities are shown to be enhanced as molecular confinement increases. Optoelectronic properties of the polymer are retained in the nanostructure, with significant increases in photovoltaic fill-factor observed.

It has been observed that solvent selection can play key roles in conduction processes in conjugated polymer systems. Chapter 5 explores the effects of solvent choice in solution-based template wetting nanofabrication. Two of the most commonly investigated semiconducting polymers are dissolved in a variety of common organic

solvents, and nanotubes created from these solutions are characterized. Current densities are shown to vary between space-charge-limited and ohmic, and hole mobilities are observed to increase by as much as four orders of magnitude, depending on the choice of solvent.

Chapter 6 investigates the effect of impurities on electronic properties of polythiophene nanotubes. Soxhlet extraction has been shown as an effective means of removing residual catalyst particles and other impurities from polythiophene, and is used here to filter bulk polymer before the template wetting process. Group contribution methods are used to predict solvent interaction parameters for various end groups and molecular weights of the polymer that may be present in the bulk material. Hole mobility in nanotube-based, electronic devices is shown to vary with both template pore diameter and extraction solvent.

Finally, Chapter 7 concludes the dissertation; reiterating key results from the work and discussing possible research paths for future work.

## **CHAPTER 2**

### **LITERATURE REVIEW**

Semiconducting polymers have been employed in a wide range of electronic devices including light-emitting diodes [10, 11], photovoltaics [13, 14], and thin-film, field-effect transistors [4, 15, 16]. While some such devices have found potential commercial use, poor device performance metrics have prevented wide spread application of organic electronics [18]. The understanding of the physical phenomena responsible for these limitations has increased rapidly since organic electronics were first conceived, and now points to a clear path to device improvement. The universal limitation for organic electronics is now widely recognized to be poor carrier transport due to the amorphous nature of organic materials, thus enhanced molecular ordering in organic systems is essential [9, 33].

Chapter 2 is broken in to two major sections, Organic Electronics and Nanostructuring of Organic Materials. In the first section, Organic Electronics, carrier transport mechanisms in organic systems, and the means by which they are measured, are briefly reviewed. This is followed by a discussion of device physics and models commonly used to describe conduction in electronic devices, and a review of their application in relevant literature. Nanostructuring of Organic Materials reviews three important techniques for producing nanotubules and nanofibers from polymers, and discusses observations of enhanced molecular ordering in such structures.

## Organic Electronics

### Carrier Transport

Semiconducting behavior in conjugated organic materials originates from the alternating  $\pi$ - and  $\sigma$ -bonding due to  $sp^2$  hybridization of the carbon bonding along the polymer backbone. The formation of the carbon double bond converts the two individual  $p$  orbitals into low-energy bonding,  $\pi$ , and high-energy anti-bonding,  $\pi^*$ , molecular orbitals [26]. The two  $\pi$ -electrons in the bond will occupy the  $\pi$  energy level, absent the presence of optical or thermal excitation energy greater than the difference between the  $\pi$  and  $\pi^*$  levels. For molecules with extensive conjugation, such as *trans*-polyacetylene (*trans*-CH<sub>x</sub>), this phenomenon of overlapping  $\pi$ -orbitals repeats along the full length of conjugation. This creates two orbital configurations (one  $\pi$  and one  $\pi^*$ ) for every  $sp^2$  carbon, and equally many possible electron wavefunctions,  $\psi_i$ . This is illustrated in Figure 2.1 following [34] for a brief segment of *trans*-CH<sub>x</sub>.

The energetic separation between two separate  $\pi$ -orbitals (or  $\pi^*$ -orbitals) becomes negligible as the number of bonding sites increases, and the distribution of energies form a continuum, like those observed in inorganic semiconductors. These  $\pi$ - and  $\pi^*$ -continua of semiconducting organics are analogous to the valence and conduction bands in inorganic counterparts. The valence and conduction band edges are analogous to the highest-occupied-molecular orbital (HOMO) and the lowest-unoccupied-molecular orbital (LUMO), while the forbidden energy region between the HOMO and LUMO is likewise analogous to the bandgap,  $E_g$ . The interchangeability of these terms is controversial, but is nonetheless commonality in the literature.

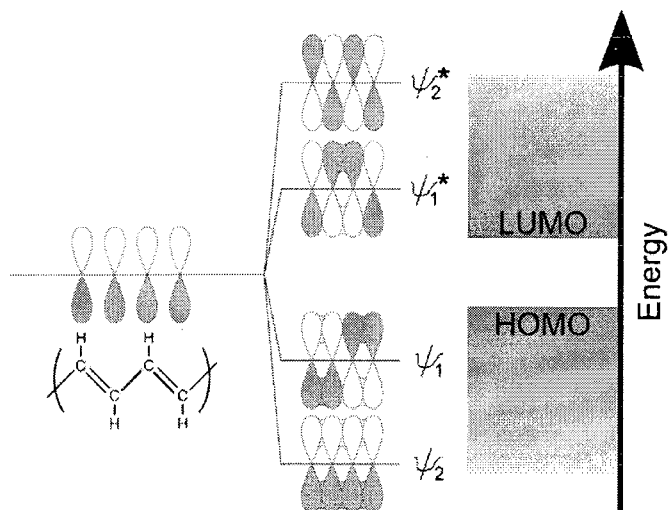


Figure 2.1. Overlapping  $p$  orbitals from the  $sp^2$  carbons along the conjugated backbone of  $trans$ - $CH_x$  form  $\pi$ -bonding and  $\pi$ -anti-bonding molecular orbitals, giving rise to two continua of energetic states which the bonding electrons may occupy.

Carrier transport in organic systems is primarily due to delocalization of  $\pi$ -electrons along the length of molecular conjugation [27]. Delocalized charge carriers are then relatively free to move along the molecule within the confines of the effective conjugation length, tunnel between conjugated segments on the same molecule if separated by molecular defect, or even hop between adjacent molecules, with decreasing probability [35]. The least probable, and thus least efficient, means of transport is intermolecular hopping [35], and it has been shown as the limiting factor in charge transport through thin films of organic materials [9, 36].

Carrier transport through solid media is most easily described by charge carrier mobility. The concept of carrier mobility arises from the need to quantify the ease with which charge is transported by a material. The mobility,  $\mu$ , is defined as the velocity with which a free carrier will drift,  $v_d$ , through the material in question per unit of applied electric field,  $F$ , following

$$\mu = \frac{v_d}{F}, \quad (2.1)$$

and is typically reported in  $\text{cm}^2 \text{V}^{-1} \text{s}^{-1}$  [37]. Hole (positive charge carrier) and electron mobilities,  $\mu_p$  and  $\mu_n$  respectively, are measurable and contribute to current density,  $J$ , as

$$J = (q\mu_p p + q\mu_n n)F, \quad (2.2)$$

where  $q$  is the electronic charge, and  $p$  and  $n$  are the number of free holes and electrons per cubic centimeter of material, respectively. Table 2.1 provides some typical values for hole mobilities in some common inorganic and organic semiconducting materials.

Table 2.1. Hole mobilities in common semiconducting materials at 300 K.

Material	$\mu_p$ ( $\text{cm}^2 \text{V}^{-1} \text{s}^{-1}$ )	Ref.
Crystalline Ge (Intrinsic)	1900	[38]
Crystalline Si (Intrinsic)	480	[38]
Crystalline GaAs (Intrinsic)	400	[38]
Pentacene	0.25	[30]
Poly(3-hexylthiophene) (Regioregular)	$10^{-4} \sim 10^{-2}$	[39]
	0.1	[9]
Poly(3-hexylthiophene) (Non-Regioregular)	$\sim 10^{-5}$	[4]
Poly(2-methoxy,5-(2'-ethyl-hexyloxy)-1,4-phenylene vinylene	$\sim 10^{-6}$	[40]

## Device Physics

Organic electronic devices, such as light-emitting diodes and photovoltaic cells, are typically fabricated by sandwiching the organic layer between two conducting materials [19]. In such structures, current density behavior is defined by both the injection properties at the contact/organic interface and the bulk transport properties of the organic material itself. Charge carriers are injected into the organic layer by means of either thermionic emission over the injection barrier,  $\phi_b$ , tunneling through the barrier, or a combination of the two [41]. Bulk transport of the injected charge is in turn described

by the free carrier mobility and the effective density of trapping states within the material [42]. While carrier injection and bulk transport occur simultaneously under an applied bias, the least efficient mechanism will dominate the observed current density characteristics.

Early work on the subject of carrier injection by Parker described the primary injection mechanism in devices made from the semiconducting poly(2-methoxy,5-(2'-ethyl-hexyloxy)-1,4-phenylene vinylene (MEH-PPV) as Fowler-Nordheim (FN) tunneling [43]. FN tunneling assumes the tunneling injection barrier,  $\phi_{FN}$ , is triangular in shape, and that current density is described by

$$J \propto F^2 \exp\left(\frac{-c\phi_{FN}^{3/2}}{F}\right), \quad (2.3)$$

where  $c$  is a constant [37]. Using this model, Parker determined that current densities in MEH-PPV devices were injection limited, and thus dominated by the FN mechanism for electric field strengths greater than  $5 \times 10^5$  V/cm [43]. However, Parker contended that the model may not hold when the work function of the contact was very near either band edge, and that ohmic contacts might be possible [43]. Indeed, work immediately following by Antoniadis et al. demonstrated that ohmic contact was possible in PPV devices, and that space charge injected into the material acted to limit sustainable current densities [44]. Blom later demonstrated that current densities were not only space-charge-limited, rather than limited by FN tunneling, but also that FN mechanisms did not accurately explain conduction in devices with ohmic contact at all [42].

Thermionic emission was then used to explain carrier injection in semiconducting polymers [41, 42, 45]. Thermionic emission theory suggests that injected current varies

with the Schottky barrier height,  $\phi_B$ , the applied bias  $V$ , and the temperature,  $T$ , according to

$$J = A^*T^2 \exp\left(-\frac{q\phi_B}{kT}\right) \left(\exp\left(\frac{qV}{kT}\right) - 1\right), \quad (2.4)$$

where  $A^*$  is the effective Richardson coefficient, and  $k$  is Boltzmann's constant [37]. Once charge carriers are given enough energy to overcome  $\phi_B$ , they are injected into the material. This model more accurately explained the injection properties into semiconducting polymer devices dominated by bulk (ohmic contacts,  $\phi_B < 0.4$  eV) and injection limited (non-ohmic contacts,  $\phi_B > 0.4$  eV) transport [46]. Schottky barrier heights for both holes,  $\phi_{Bp}$ , and electrons,  $\phi_{Bn}$ , into MEH-PPV and poly(3-hexylthiophene) (P3HT) are readily calculated for a variety of metallic contacts using the metal work functions,  $\Phi_m$ , listed at right in Figure 2.2. These two polymers are studied throughout this work, and are described in detail in Chapter 3.

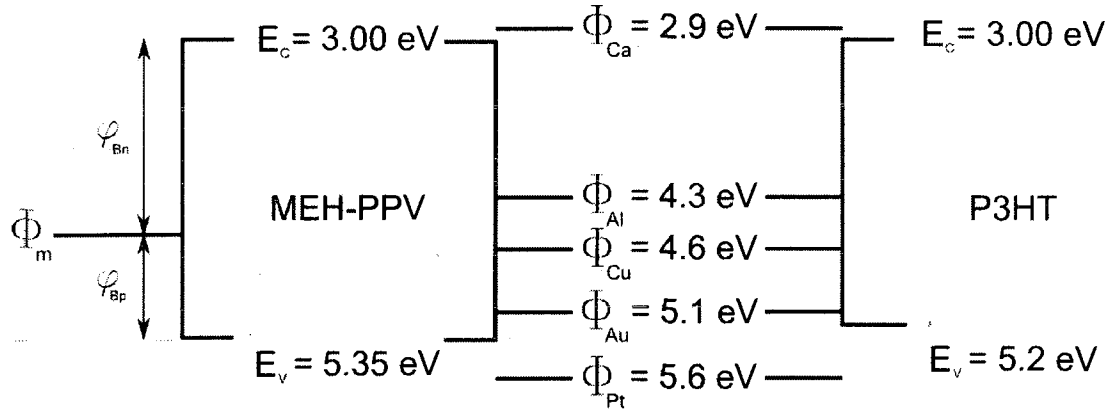


Figure 2.2. Injection barrier heights for thermionic emission models illustrated by example with actual energy levels for MEH-PPV [47] and P3HT [48] with and common contact materials. Values are positive with respect to vacuum.

Thermionic emission of charge carriers into a medium in which the mobility is too small to effectively transport all injected charge through the material between electrodes will inevitably create a layer of space charge in the material [49]. Space charge accumulation in a medium was first observed by C. D. Child when examining emissions from CaO electrodes in vacuum diodes [50]. The currents flowing through the diodes became limited by the presence of ionized, gaseous species present in the vacuum tube – space charge. Child reckoned that if the concentration of ionic species of one type exceeded that of the other, the electric field created by their presence must be relevant and potentially in opposition to the applied field. He then demonstrated mathematically and experimentally that the buildup of this space charge would limit attainable current densities [50].

Later, N. F. Mott and R. W. Gurney described presence of space-charge-limited (SCL) currents in insulating layers, and the possibility of their existence in semiconductors [51]. Due to the near nonexistent carrier transport in insulators, they hypothesized that if charges could be injected into an insulating layer, these charges would form significant space-charge and act to inhibit further increases in current density [51], just as was observed with Child's ionic gas. They suggested that the injection of such currents into insulators should be facilitated by proper selection of the electrode materials, such that these materials work functions nearly align with conduction band edge when electrons are the majority carriers or the valence band edge when hole conduction is dominant [51]. In an ideal situation where the insulating layer is free of trapping states [51], demonstrated that the behavior of these SCL currents should be

quadratically dependent on the applied voltage. Presented here in the most commonly published form following [37] the Mott-Gurney Law for current density,  $J$ , follows

$$J = \frac{9}{8} \epsilon_0 \epsilon_r \mu \frac{V^2}{L^3}, \quad (2.5)$$

where  $L$  is the device length. Equation (2.5) is often referred to as the trap-free space-charge-limited conduction model, TF-SCLC.

Research carried out in the 1950s at RCA Laboratories by Smith and Rose demonstrated SCL currents to be dominant in thin films or slices of the insulating materials like cadmium sulfide [52, 53]. This work went beyond that of Mott and Gurney by examining effects of the presence of trapping energy levels within the bandgap. They demonstrated that the filling of these trapping levels could have significant effects on the current-voltage characteristics. Concurrent work at Bell Laboratories described the presence of SCL currents in semiconductors both theoretically [54] and experimentally [55].

Work by Murray Lampert consolidated theories of SCL conduction, demonstrating that the idealized case described by (2.5) was in fact a limiting case [56]. Lampert proposed that the magnitude of the lower limit of currents flowing within a poorly conducting material should be described by (2.2) where currents were injection limited, while the upper limit is described by the trap-free model of (2.5) as shown in Figure 2.3a [56]. He further demonstrated that the transition between the two limiting cases varied with the density and energetic ordering of charge trapping sites. Given an insulator in which a significant number of trap levels exist within the forbidden energy levels in the material, be they due to impurities or material defects, the SCL currents in the material should be less than that of the trap-free case [52, 56]. Currents were shown to

rise toward the quadratic relation when a high concentration of traps at a given energy level became filled, as in Figure 2.3b [56].

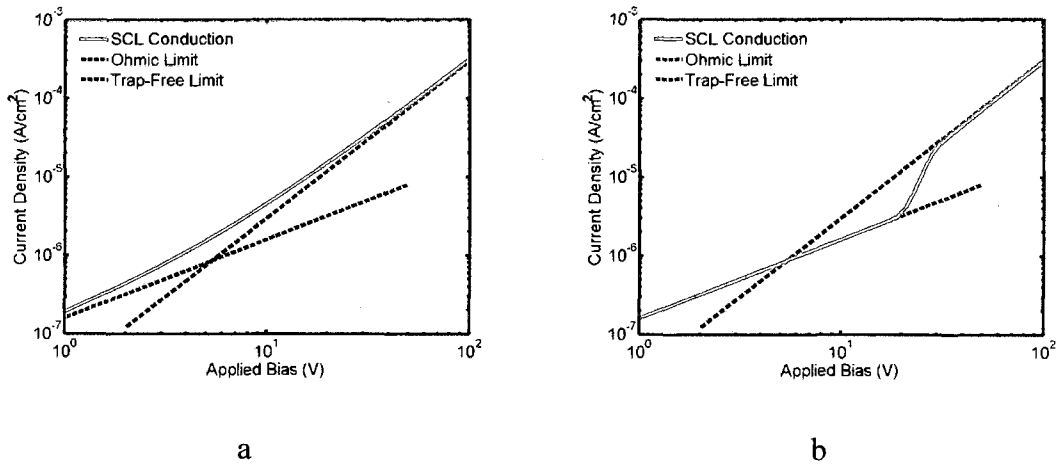


Figure 2.3. Ideal J-V characteristics following the formalism of space-charge-limited conduction in a) the absence of and b) the presence of an energetic trap distribution.

While the theory of SCL currents was developed out of insulator physics, the model has been widely used for describing carrier transport in semiconducting polymers with ohmic contacts. Reference [42] demonstrated that carrier transport in a poly(dialkoxy-*p*-phenylene vinylene) was space-charge limited as described by (2.5), contrary to the widely accepted idea (at the time) that transport in conjugated systems was injection limited rather than bulk limited [43]. Reference [42] applied the model to semiconducting polymers by assuming that conduction in a semiconducting polymer with some significant distribution of trapping states ought to behave similar to that of an insulator with traps due to exceptionally low carrier mobilities when compared to their inorganic counter parts. As anticipated, current density in polymers was shown take on a quadratic dependence on electric field at low field strengths.

Later work by Chiguvare et al. with semiconducting poly(3-hexylthiophene) (P3HT) suggested that the linear behavior of currents, as described by [56] and illustrated in Figure 2.3, in low-mobility materials could be accounted for mathematically by a simple linear combination of the ohmic behavior described in (2.2) and trap-free SCL conduction following (2.5) written as

$$J = q\mu_p p \frac{V}{L} + \frac{9}{8} \epsilon_0 \epsilon_r \mu_p \frac{V^2}{L^3}, \quad (2.6)$$

where  $\mu_p$  is the hole mobility, and  $p$  is the intrinsic carrier concentration [57, 58]. This carrier concentration is understood to be the concentration of free carriers within the material before space-charge accumulation becomes significant.

Reference [42] further explained that the presence of the space charge must alter the injection properties, and determined that carrier transport could be well described by a variation of thermionic emission model. It was also suggested by [42] that the most accurate description of injection into low-mobility organic semiconductors must follow the thermionic-emission-diffusion theory developed by Sze and Cromwell [59]. This model improves upon standard thermionic emission by accounting for the effects of carriers diffusing through the semiconductor [37, 42]. These carriers create internal electric fields, known as the imaging forces, which act to lower the Schottky barrier; a model consistent with observations and effects of space charge accumulation within organic semiconductors [42]. Following [42], the effective Schottky barrier in (2.4) is equivalent to

$$\varphi_B = \varphi_{B0} - \Delta\varphi = \varphi_{B0} - \sqrt{\frac{qF(0)}{4\pi\epsilon_0\epsilon_r}}, \quad (2.7)$$

where  $\varphi_{B0}$  is the uncorrected Schottky barrier,  $\Delta\varphi$  is the image force,  $\epsilon_0\epsilon_r$  is the dielectric permittivity, and  $F(0)$  is the electric field at the contact. When significant space charge is

present, the internal electric fields within the semiconductor vary greatly [60], and are well described by

$$F(x) = \sqrt{F(0)^2 + \frac{2Jx}{\epsilon_0 \epsilon_r \mu}}, \quad (2.8)$$

where  $x$  is the distance from the injecting contact into the semiconductor [42]. Following this model in the ideal case,  $F(0) = 0$  for ohmic contact and  $F$  varies with  $x^{1/2}$ , while  $F(x) = F(0) = V/L$  for an injection limiting case [42].

The theory of SCL currents in semiconducting polymers was furthered by [42] by describing the temperature and field dependencies of the mobility [61]. TF-SCLC was observed to underestimate actual current densities at high electric fields, and a field-dependent mobility following

$$\mu(F) = \mu_p(0) \exp(\gamma \sqrt{F}), \quad (2.9)$$

where  $\mu_p(0)$  is the mobility of the TF-SCLC in (2.5) and (2.6) and observed in the low-field limit [61]. This behavior was also been observed in both time-of-flight [40] and current density studies of hole mobility in MEH-PPV [45, 46]. Reference [61] demonstrated the existence an Arrhenius dependence for  $\mu_p(0)$  given by

$$\mu(0, T) = \mu_0 \exp\left(-\frac{\Delta}{kT}\right), \quad (2.10)$$

where  $\Delta$  is the thermal activation energy, and  $\mu_0$  is a prefactor [61]. Such temperature dependent behavior is synonymous with carrier hopping models used to describe conduction in energetically disordered systems. The field and temperature dependent behavior of mobility was later confirmed by [46].

Modeling of current density characteristics using the SCL formalism described above is now nearly universally accepted, and is common place in the literature. These

models have been applied extensively to P3HT [57, 58, 62] and PPV derivatives [42, 63], including MEH-PPV [44-46, 60]. Table 2.2 consolidates the models used to describe conduction in semiconducting polymers and the conditions in which each model is valid.

Table 2.2. Basic conduction models for semiconducting polymers.

Model	Expression	Conditions	References
Fowler-Nordheim Tunneling	$J \propto F^2 \exp\left(\frac{-c\phi_{FN}^{3/2}}{F}\right)$	$\phi_{B0} > 0.4 \text{ eV}$ $F > 10^6 \text{ V/cm}$	[37, 43, 64]
Thermionic-Emission-Diffusion Theory	$J = A^*T^2 e^{-\frac{q\phi_B}{kT}} \left(\frac{qV}{kT} - 1\right)$ given $\phi_B = \phi_{B0} - \Delta\phi = \phi_{B0} - \sqrt{\frac{qF(0)}{4\pi\epsilon_0\epsilon_r}}$	Generally Applicable	[42, 46, 49, 59, 65]
Trap-Free Space-Charge-Limited Conduction	$J = \frac{9}{8}\epsilon_0\epsilon_r\mu\frac{V^2}{L^3}$	$\phi_{B0} < 0.4 \text{ eV}$ $F < 10^5 \text{ V/cm}$	[42, 44, 51, 56]
Temperature and Field Dependent Space-Charge-Limited Conduction	$J = \left(\frac{9}{8}\epsilon_0\epsilon_r\frac{V^2}{L^3}\right) e^{\gamma\sqrt{F} - \frac{A}{kT}}$	$\phi_{B0} < 0.4 \text{ eV}$	[40, 45, 46, 61, 66]
Ohmic to Space-Charge-Limited Conduction	$J = q\mu_p p \frac{V}{L} + \frac{9}{8}\epsilon_0\epsilon_r\mu_p\frac{V^2}{L^3}$	$\phi_{B0} < 0.4 \text{ eV}$ $F < 10^5 \text{ V/cm}$	[56-58]

### Nanostructuring of Organic Materials

Since the introduction of carbon nanotubes (CNTs) [67], strong interest in cylindrical nanostructures of various materials has arisen. CNTs have been considered for a wide range of applications, but have proven to be far less than perfect for most cases due mainly to the simple fact that carbon is by no means a universal, all-purpose material [68]. The discovery of CNTs did, however, open the minds of scientists to the idea that such structures might be possible in other materials, and that these materials might possess interesting properties not common to the bulk material.

The inherent one-dimensional nature of cylindrical nanostructures highlighted their potential uses, both pure and applied, in a wide variety of applications including electronics, fluidics, and catalysis, and thus motivated further research [69]. Nanotube structures possess nanoparticle like advantages including massive surface areas, electronic properties that often vary widely from that of the bulk material, and intrinsic anisotropy of structure [70]. Where the fabrication of nanotubes and nanowires from polymers is concerned, three commonly explored processes exist: electrospinning [71], template synthesis [72], and template wetting [32]. In general, the two latter approaches have been demonstrated to be far more universal with respect to the range of applicable materials; however, in the context of this work, electrospinning is an equally important technique.

### **Electrospinning**

Reneker and Chun first described electrospinning as an effective means of producing thin polymer fibrils from a wide range of polymers in 1996 [71]. They adapted a process described in 1934 by Formhals for mass manufacture of polymeric thread [73]. The process created thread from polymer solutions by passing a very fine stream of the solution through an electric field formed between two conductive surfaces, one of which was grounded and acted to collect the thread. In the case of Formhals, this was a conductive spool. Reneker used this idea to generate fibers using low concentration solutions and very high electric fields generated from voltages of between 5 kV and 20 kV which created very fine streams with diameters ranging from 40 nm to 2  $\mu\text{m}$  [71]. The process as described by Reneker is illustrated in Figure 2.4.

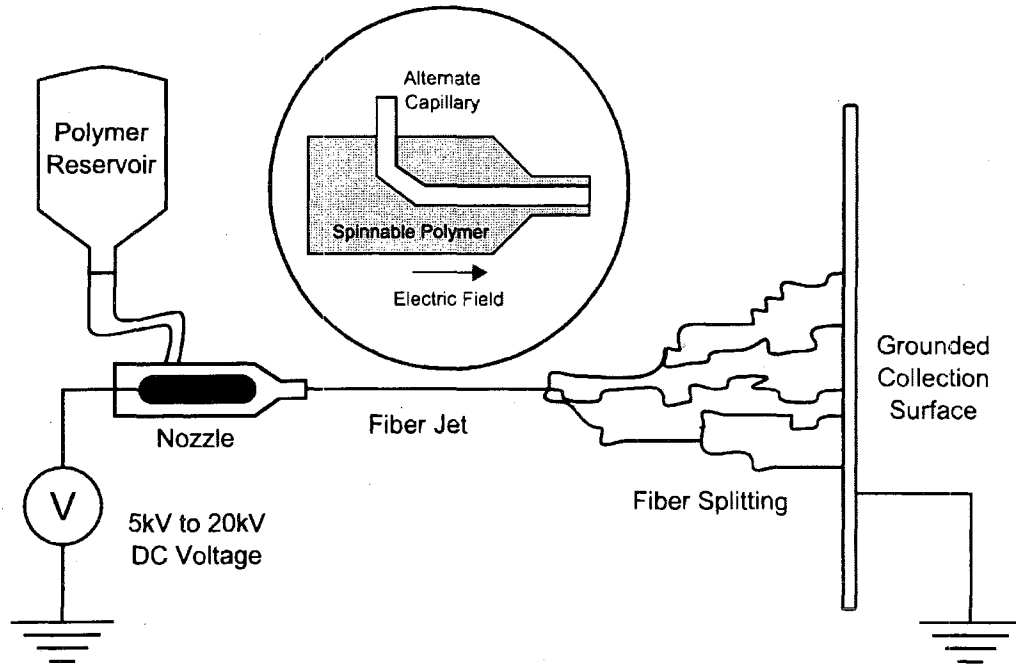


Figure 2.4. Schematic of a typical electrospinning system, following [71]. The circular inset illustrates the use of an alternate capillary which is concentric to the normal nozzle configuration. This setup is described in [74].

The electrospinning process calls for a reserve of liquid polymer, be it a melt or solution, which is fed to a nozzle. A very high electric field is applied to the polymer near the nozzle by either a high voltage probe, or by directly biasing a metallic nozzle. The electric field induces movement of charge in the solution, and the droplet at the tip of the nozzle begins to take a conical form rather than hemispherical; this is critical to the creation of ultra-thin fibers [75]. Once the electrical forces completely overcome the surface tension at the nozzle, a fine jet of solution will emerge from the tip of the cone.

This jet accelerates in the direction of the collecting electrode, causing the jet to shrink diametrically as elongational viscosity opposes the electrically induced force [71]. By design, one can alter the final diameter of the collected fibers by varying the distance between the nozzle and the collecting electrode and altering the conductivity of the spinning solution [76]. As the jet approaches the collector, the electrical field reduces,

and radial forces from the charges in the jet overcome the cohesive forces holding the jet intact. The jet splits into numerous thinner streams which whip about in tangled bunches which are finally deposited onto the collector, completing the process [75]. In depth dynamical analysis of the motion of these charged streams leading to fiber splitting is highlighted elsewhere, see [77] for example. This splitting effect makes controlled deposition of the nanofibers by this method very difficult, as the process typically results in a woven mesh of fibers. Research has aimed to eliminate this splitting effect [78], but has failed to do so in any cost effective manner.

Disadvantages aside, Reneker and Chun had demonstrated electrospinning as a viable means of producing nanofibers from a wide range of polymers including polyimides, nylon, polyaramid, conducting polyaniline, and even DNA [71]. Later work demonstrated its uses with poly(L-lactide) [76], polystyrene, polyethylene oxide, and polymethylmethacrylate to name a few [75]. Semiconducting polymers, on the other hand, posed a problem.

Electrospinning had proven difficult with most conjugated polymers, because of limited solubility in ionic solvents. The conducting polymer polyaniline had proven no problem in this respect due to its high solubility in dilute sulfuric acid [71], but this was not the case for semiconducting polymers like MEH-PPV and P3HT [74]. Problems of this nature are usually handled by co-dissolution of the low-solubility polymer into a highly spinnable polymer, like poly(vinyl pyrrolidone) (PVP) [74]. Li et. al. found this difficult, as the chloroform solutions of the conjugated polymers were immiscible with aqueous PVP [74]. They subsequently modified the process by electrospinning with what they called a “two-capillary spinneret” [74].

The key difference in this modified process was in the nozzle. Whereas the nozzle had traditionally consisted of only one opening, they used two concentric nozzles as shown in the inset of Figure 2.4 to flow the chloroform solution of MEH-PPV into the core of the PVP solution. This produced composite PVP/MEH-PPV fibers that were shown to retain optical properties of the MEH-PPV by ultra-violet/visible (UV-Vis) spectroscopy. Removal of the PVP by exposure to ethanol was shown to be possible, leaving behind MEH-PPV fibers that resembled ribbons or rods, depending on the starting concentrations of MEH-PPV solutions [74].

The two-capillary spinneret technique was also demonstrated with blends of MEH-PPV and other semiconducting polymers including P3HT and poly(9,9-dioctylfluorenyl) (PFO), a light-emitting polyfluorene [74, 79]. Field-effect transistors fabricated from electrospun nanofibers of P3HT/MEH-PPV blends were characterized, demonstrating hole mobilities varying from  $\sim 10^{-5} \text{ cm}^2 \text{ V}^{-1} \text{ s}^{-1}$  (70 %wt. MEH-PPV) to  $10^{-3} \text{ cm}^2 \text{ V}^{-1} \text{ s}^{-1}$  (20 %wt. MEH-PPV) [79]. UV-Vis spectroscopy of fibers also showed some familiar optical properties of each constituent in the composite as described above for MEH-PPV fibers. However, analysis showed much weaker absorbance from the MEH-PPV relative to that of the P3HT peak in blended nanowire form as compared to that of thin films created from the P3HT/MEH-PPV blend [74]. The authors suggested this was due enhanced charge transfer between the two conjugated polymers as a result of strong molecular interactions caused by extrusion induced confinement in the structure [74, 79]. Similar observations were also made for nanofibers created from PFO/MEH-PPV blends [79].

## Template Synthesis

The use of nanoporous membranes as molds for the creation of nanowires and nanotubes presented far simpler fabrication procedures while simultaneously broadening the range of useable materials. The fabrication of nanostructured materials using template-based synthesis processes was initially and most widely applied by C. R. Martin [72, 80]. Martin, among others, has demonstrated creation of both fibrillar and tubular structures by chemical synthesis, electro-polymerization, or electro-deposition of the desired material within porous media. Template synthesis processes of this type have been demonstrated with conductive polymers [81-92], metals [93-96], and inorganic semiconductors[97] among others [72, 80]. Electro-deposition of metallic and inorganic materials is detailed in the literature, but is largely irrelevant to the current work. The production of conjugated polymer nanostructures using template synthesis is usually accomplished by one of the first two methods, chemical synthesis or electro-polymerization.

Chemical synthesis involves a two chamber cell, in which the nanoporous membrane acts as a division. One chamber is filled with a solution containing the monomer of the desired nanotube material, while the other is filled with a solution containing an oxidant reagent [83, 86]. The reagent and monomer diffuse into the membrane, where they react to initiate polymerization. The polymerization occurs preferentially and uniformly on the pore walls and the macroscopic surfaces of the membrane [85]. This method has been demonstrated with conducting polyacetylene (PA) [82], polyaniline (PANi) [85], poly(3-methylthiophene) (P3MT) [84], and polypyrrole (PPy) [81,86].

Electro-polymerization, or electrochemical synthesis, involves the metallization of one side of the nanoporous membrane, which will serve as a working electrode. The membrane is subsequently submerged in an electrolytic solution containing the desired monomer. As current is passed through the solution, polymerization occurs within the nanopores. Tuning of processing parameters including polymerization time and temperature, applied current density, and monomer concentration have been shown to alter properties of nanotubes or nanowires formed with this process [90, 91]. Due to this enhanced control of processing, electro-polymerization has been more widely used in recent literature. This method has been demonstrated effective with conducting polymers including PPy [86], PANi [87], poly(3,4-ethylenedioxythiophene) (PEDOT) [87, 89], and P3MT [98]. Electro-polymerization of semiconducting polythiophene [98] and PPV [91] have also been demonstrated.

Martin's work demonstrated multiple order of magnitude increases in conductivity in PA [82], PANi, [85] PPy, and P3MT [81] chemically synthesized within nanoporous membranes. The origin of this increased conductivity was shown to be due to preferential alignment of the polymer chains during synthesis. Nanotubules of PA were investigated using polarized infrared spectroscopy, demonstrating molecular alignment believed to be parallel with the length axis of the nanotube [82]. Also noted was the fact that conductivity appeared to increase more rapidly with decreasing pore diameter in all polymers studied [72, 80-85]. As pore sizes increased much beyond 400 nm, the materials began to behave much more like similarly synthesized thin films [82]. Later work utilized polarized infrared spectroscopy and X-ray diffraction analyses to show not only preferential molecular alignment (as described above) in PA, PPy, and P3MT

materials, but also an enhancement of order as the nanopore diameter decreased, supporting earlier observations of increased conductivity [84]. The same methods were also used to show that PANi molecules aligned perpendicularly, rather than parallel, to the nanopore length axis, and that the molecules in closest proximity with the pore walls were most highly ordered [85].

### **Template Wetting**

Template wetting was first introduced by Steinhart and co-workers in 2002, and has proven to be a simple and effective method for the creation of nanostructured materials [32]. In this process (detailed in Chapter 3), wetting phenomena are exploited to create uniform coatings of low surface energy materials, including many polymer solutions and melts, on high energy pore surfaces such as in porous alumina. Using this method, nanowire and nanotube structures were created from a wide range of organic materials, including many structural and high-performance polymers such as polytetrafluoroethylene (PTFE) [32, 69] and poly(vinylidene difluoride) (PVDF) [99]. Later work demonstrated the effectiveness of the template wetting process with organic semiconducting materials including pentacene [100] and various the light-emitting polymers [101-103].

Nanostructures fabricated using template wetting have demonstrated interesting properties when compared to bulk materials. High degrees of molecular ordering have been observed in nanotubes created using the template wetting process, with molecules tending to orient themselves either parallel [103] or perpendicular [70, 99] to the nanopore wall. For example, Steinhart et. al. observed curvature-directed crystallization of PVDF when creating nanotubes of the material by template wetting with PVDF melts [99]. This confinement-induced ordering of molecules oriented perpendicular to the

nanopore wall, producing a brush-like structure along the inner wall [99]. However, such ordering was not observed in nanotubes created from PVDF solutions. Steinhart speculated that the lack of ordering observed in PVDF nanotubes created from solutions, rather than melts, may have been largely due to solvent quality, but this was not examined experimentally [99]. Although it was clear that organic nanostructures could be created using solution-based methods, this type of template wetting was not fully reviewed until 2008, when a former colleague of Steinhart examined the effects of a number of process parameters [104].

The first reported semiconducting polymer nanowires created by template wetting were created circa 2006, using solution solution-based processes [101, 102]. Later, solution-based template wetting was used to produce nanostructures from the light-emitting polymer poly(9,9-dioctylfluorene-2,7-diyl) (PFO), and strongly enhanced molecular ordering was again observed [103]. However, in the solution wetting case, molecules were observed to align parallel to the nanotube axis [103], similar to observations made with template synthesized polyacetylene [82]. While X-ray diffraction confirmed enhancement in the molecular ordering of PFO due to the nanopore-induced confinement [103], characterization of electronic properties was kept to a minimum.

As has been discussed above for other fabrication methods, enhanced ordering may lead to significantly different electronic properties for amorphous semiconducting polymers. Thus, the production of polymer nanostructures by template wetting processes is of great interest for both theoretical investigation of the  $\pi$ -conjugated, electronic system, and electronic device optimization. The *perpendicular* stacking of molecules observed when processing PVDF melts [99] is very similar in structure to molecular

stacking described in thin films of self-ordering polythiophenes [9]. Such an orientation should facilitate high degrees of intermolecular  $\pi$ -orbital overlapping, which is essential to increase carrier mobilities in less ordered organic electronic systems [6, 26]. Further, observations of molecular orientation *parallel* to the nanotube length axis [103] suggests that carrier transport in such systems may actually be governed predominately by intrachain charge transfer. This could reduce the number of intermolecular charge transfer events, and thus result in drastically improved carrier mobilities. Confinement of amorphous semiconducting polymers, such as MEH-PPV, by template wetting may lead to similar ordering, and thus improved electronic properties.

## CHAPTER 3

### EXPERIMENTAL METHODS

The majority of this work is concerned with fabrication and electronic characterization of semiconducting polymer nanostructures. Solution-based template wetting is employed in the creation of these nanostructures throughout this work, and is discussed in detail in this chapter. The primary means of electronic characterization is by analysis of space-charge-limited (SCL) currents and ultra-violet-visible (UV-Vis) spectroscopy. However, photovoltaic devices and temperature-dependent current measurements are also analyzed in Chapter 4. The effects of template nanopore diameter, solvent selection, and filtration are examined for both amorphous and semi-crystalline semiconducting polymers. Specific details of the nanotube fabrication and characterization procedures are described here.

#### Materials

Conjugated polymers owe their conductivity to the alternating single and double bonds between carbons along the polymer backbone. The simplest example of this chemical structure is that of the first observed electronic polymer, polyacetylene, as discussed in Chapter 1 [1-3]. However, any organic in which the carbon atoms of the backbone form  $sp^2$  hybrid orbital structures will exhibit similar characteristics. This type of molecular structure is present in many five- and six-atom ring structures [105, 106],

and is the basis of conduction in two of the most commonly studied electronic polymer systems, poly(phenylene vinylene), or PPV, and polythiophene. Pure forms of either of these materials are virtually insoluble [4, 10], but the addition of functional side chains permit solubility in a number of organic solvents [11, 28, 105, 107]. Chemical structures of PPV and polythiophene are illustrated with general side chains, denoted  $R$ , in Figures 3.1a and 3.1b, respectively.

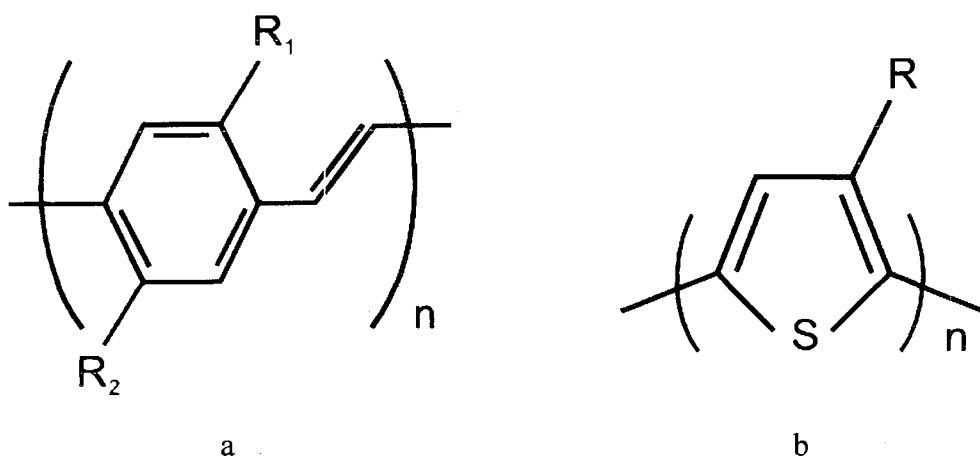


Figure 3.1. General chemical structure of a) poly(*p*-phenylene vinylene) and b) polythiophene, shown with general side chains  $R$ .

The soluble, light-emitting PPV, poly(2-methoxy-5-(2'-ethylhexyloxy)-1,4-phenylene vinylene) (MEH-PPV), has been widely studied for applications in both polymer LEDs [11, 12] and photovoltaic devices [12, 14]. Side chains for this polymer are  $R_1 = \text{OCH}_3$  and  $R_2 = \text{OC}_8\text{H}_{17}$ . MEH-PPV ( $M_n = 70,000 - 100,000$ , as powder) used in this study was obtained from Sigma-Aldrich, and used without modification.

Regioregular poly(3-hexylthiophene-2,5-diyl) (P3HT,  $R = (\text{CH}_2)_5\text{CH}_3$ ) is a soluble polythiophene typically investigated for applications in field-effect transistors[9] and photovoltaics [58]. P3HT was obtained from both Sigma-Aldrich ( $M_n = \sim 64,000$ , as

powder) and American Dye Source (MW = 20,000 – 70,000, as powder). In some instances, P3HT, was used as obtained, but was also investigated after successive filtration via Soxhlet extraction.

### **Wetting of Nanoporous Alumina with Polymer Solutions**

Template wetting procedures were first described by Steinhart et al., and were demonstrated as highly effective for creation of nanostructures from a wide array of materials [32]. Using ordered nanoporous ceramics such as porous aluminum oxide, one can create ordered structures from low surface energy materials such as polymers. The physical chemistry behind wetting, spreading, and penetrating is reviewed extensively elsewhere [108-113].

Template wetting with polymer melts was demonstrated for a number of polymers including polystyrene and insoluble, high-performance polymers such as PTFE [32]. When using this variation of the template wetting process with polymers, the polymer (in bulk form) is placed in intimate contact with the nanoporous template material, and the sample is heated slightly beyond the melting point of the polymer. The melting polymer then wets the high surface energy template, thereby infiltrating and coating the nanopore walls. This process is reviewed extensively by Steinhart elsewhere [68, 69]. While the range of compatible materials is extensive, melt-based wetting is problematic for creation of heat sensitive materials such like biomaterials and electronic polymers. Solution-based wetting is a useful alternative.

Solution-based wetting has been examined by Steinhart, but much of the work focused on the results from the melt-based process. Work with piezoelectric PVDF melts showed enhanced molecular ordering, but solution-processed material showed no such

result [99]. However, nanotubes of PVDF were still formed, and the ability to process such structures at room temperature has allowed for the creation of polymer nanostructures from a variety of materials, including semiconducting polymers [101-103]. Since then, solution-based wetting has been noted for the relatively high level of process control [104]. With the solution based process, the resultant nanostructure can be altered by solvent selection, composition and viscosity of the wetting solution, and molecular weight [104]. The process also facilitates creation of nanostructures from polymer blends with a high degree of uniformity.

In this work, commercially available anodic, porous aluminum oxide membranes (Anodisc®, Whatman Co.) were used as templates. These templates were 60 microns thick and 13 mm in diameter. Templates used had nominal pore diameters of either 100 nm or 200 nm, and pore densities of  $10^{10} \text{ cm}^{-2}$  and  $10^9 \text{ cm}^{-2}$ , respectively. Templates were placed on smooth PTFE surfaces to prevent sticking, and were wetted with polymer solutions. Wetting was accomplished by applying a known volume of polymer solution to the top of the template surface with a pipette. The solvent was allowed to evaporate for several hours before further processing. Elsewhere, work has demonstrated this process in the reverse manner, in which the template is placed onto the polymer drop [103]. The process used in this work, and illustrated in Figure 3.2, is expected to produce more accurate measures of polymer actually entering the pore, and improve repeatability, as templates tend to slide off the droplet when using the alternative approach.

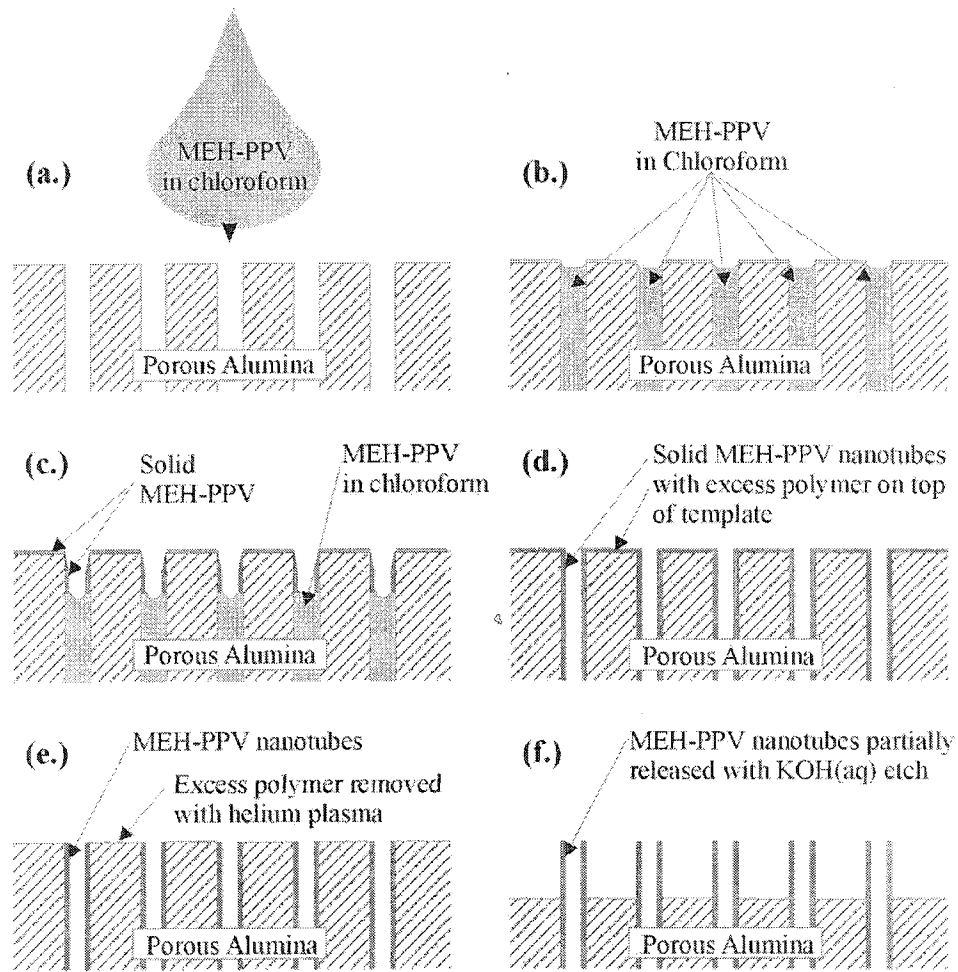


Figure 3.2. Illustration of the solution-based template wetting procedure employed throughout this work. The process is illustrated here for a MEH-PPV/chloroform wetting solution.

Applied solution volumes were calculated before wetting in order to achieve a known device area or nanotube wall thickness. The volume of solution applied to each template was calculated based on three key assumptions. Nanotube wall thicknesses were approximated by assuming that all polymer applied to the template enters the nanoporous material, and that all pores are perfect cylinders of exactly the nominal diameter,  $D_p$ .

These assumptions only approximate the actual nominal wall thickness,  $t_{wall}$ , of the formed nanotube, but these approximations are sufficient for this work. The actual densities of MEH-PPV and P3HT are  $1.12 \text{ g/cm}^3$  and  $1.23 \text{ g/cm}^3$ , as determined from

group contribution methods [114] (see Appendix), but are largely irrelevant because it is not possible to accurately determine how the confinement within the nanostructure may alter molecular packing densities. Further, the device area,  $A$ , used to calculate current densities throughout this work is largely independent of either nanotube wall thickness or polymer density, and is primarily affected by the mass of the polymer applied to the template. Calculated values for  $A$  and  $t_{wall}$  are illustrated in Table 3.1 for 100 nm and 200 nm nanotubes for proper values of  $\rho_{poly}$ .

Table 3.1. Nanotube based device area and wall thickness for solution-based template wetting procedures with 2 mg/mL polymer solutions.

$D_p$ (nm)	$\rho_{poly}$ (g cm <sup>-3</sup> )	$t_{wall}$ (nm)	$A$ (cm <sup>2</sup> )
100	1.1	0.75	0.0004
100	1.2	0.65	0.0004
200	1.1	3.75	0.0005
200	1.2	3.5	0.0004

While the area calculations discussed above assume that all polymer enters the template pores, early scanning electron micrographs (Figure 3.3a) showed that wetted template surfaces are covered with a significant amount of residual polymer, leading to overestimation of both  $t_{wall}$  and  $A$ . These overestimations in area will lead to underestimations of true current densities and carrier mobilities in electronic devices. Removal of this residual layer is necessary in order to clearly observe individual nanotubes, and confirm that any characteristics observed from the polymer are strictly from the nanotube structure. Template surfaces were etched with a non-reactive helium plasma following a process similar to that described in [115], in which He atoms basically sputter polymer away from substrate. Here, a PlasmaTherm RIE system was

used to etch template surface with a 100 W He plasma at 200 mtorr for 10 minutes on each surface. Figure 3.3b illustrates the physical removal of the residual polymer from the surface, as template pores become visible.

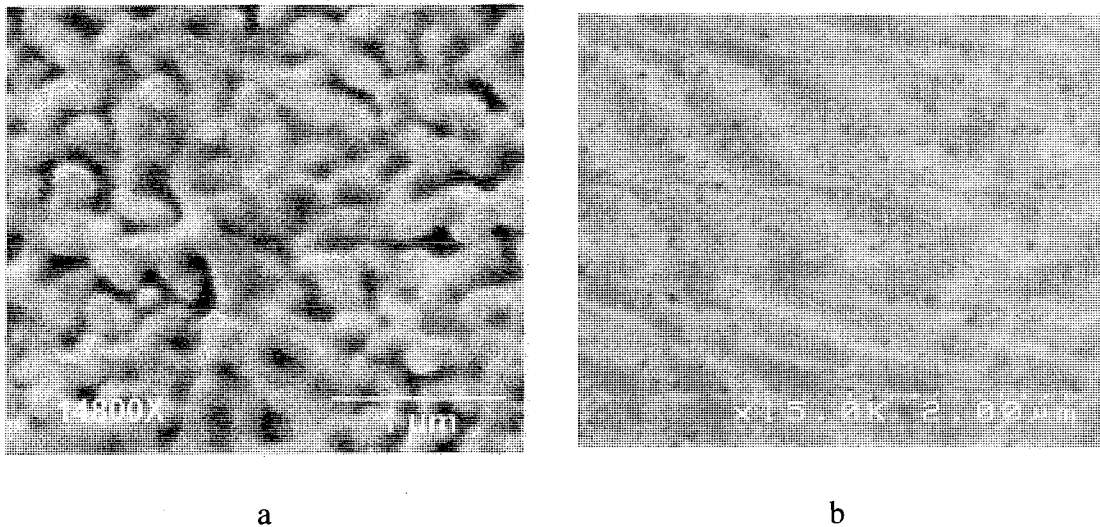


Figure 3.3. SEM micrograph of MEH-PPV coated templates a) before and b) after plasma etching to remove residual surface polymer. Figure 3.3b is courtesy of CAMD at LSU Baton Rouge.

Imaging of the tubular nature and surface morphology of the nanostructures is also desirable. A Hitachi S-4800 field-emission-gun SEM was used to physically characterize the nanotubes. Samples for this purpose were prepared for SEM by wet etching templates in 25 wt. % aqueous KOH after completion of the plasma etch. Examples of SEM imaging are presented in Figure 3.4 for nanotubes from MEH-PPV and P3HT.

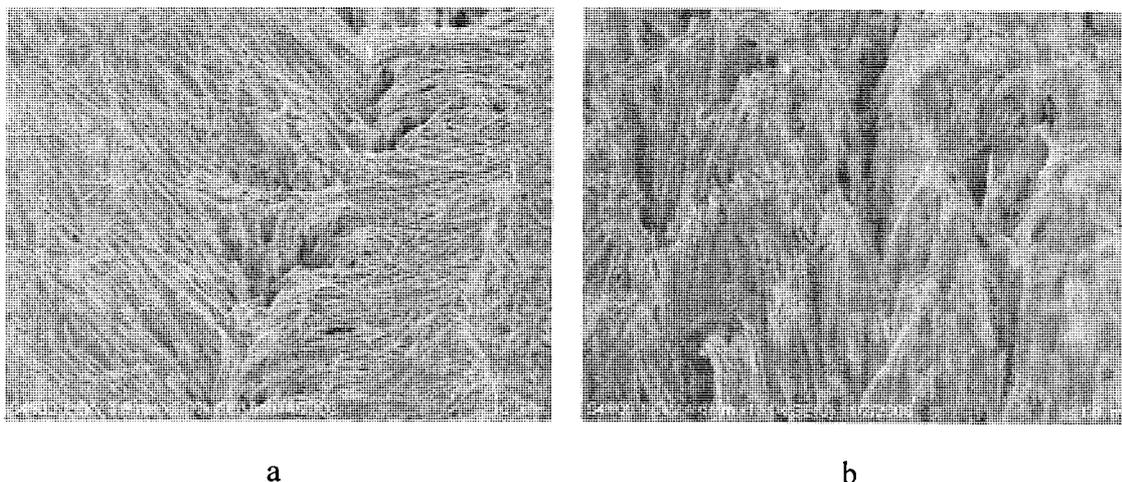


Figure 3.4. SEM imaging of a) MEH-PPV and b) P3HT nanotubes created using solution-based template wetting procedures

### **Electronic Devices**

All devices examined in this work were fabricated following the general structure of Figure 3.5a. The main device type examined in this work is the single-carrier device, following [43]. This device structure allows the researcher to examine current density contributions of either holes or electrons, without having to disentangle convoluted effects of actual two-carrier devices. Proper electrode material selection which provides for good alignment of anode and cathode work functions with the desired conduction band edge (deviation less than 0.4 eV) permits conduction of the desired carrier only. [41] Conduction and valence band edges for MEH-PPV [47] and P3HT [48] are illustrated with the work function of Au Figure 3.5b. The close alignment of the Au work function with the valence band edges in MEH-PPV and P3HT produces Schottky injection barriers of 0.25 eV and 0.1 eV respectively.

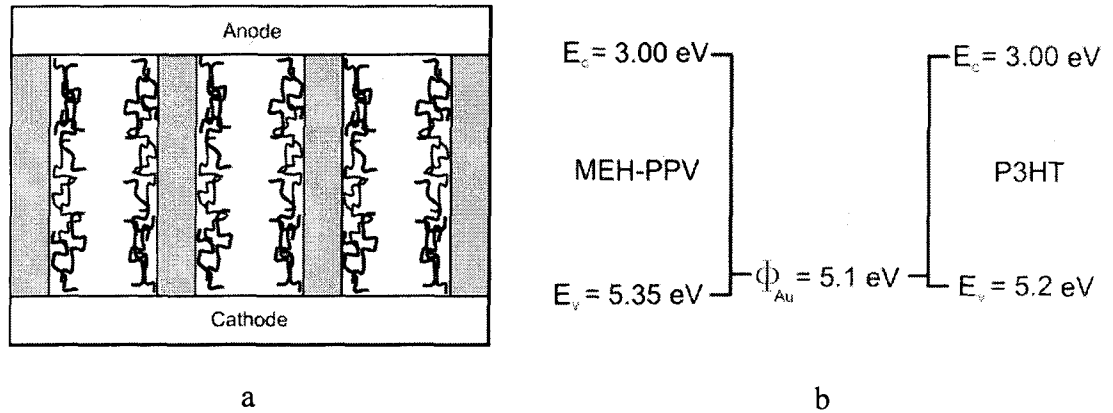


Figure 3.5. The generalized device structure used throughout this work is illustrated in a), while b) illustrates the degree of barrier height minimization due to anode and cathode material choice of Au in the construction of hole-only devices. Gray sections in a) represent the aluminum oxide template, and the squiggly lines represent incorporated polymer.

In this light, Au is used as the contacting material when examining hole-only devices for both polymers throughout this work. These devices were created by evaporation of Au onto the template surface immediately after completion of the He plasma etch. Large area continuous cathodes were formed by depositing Au through an 8 mm circular shadow mask, centered on the template. Multiple anodes were patterned on the opposite side of the template in a hexagonal pattern which produced seven devices, with diameters of 1.58 mm. Such hole-only devices are the primary type of device analyzed here, but occasionally, other device structures are examined, and they are detailed where necessary.

Analysis of measured hole current densities in single-carrier devices is carried out following thermionic-emission-diffusion theory (TED) and SCL simplifications of that model. The Mott-Gurney trap-free SCL relation (TF-SCLC) [51] for hole-only devices [42]

$$J = \frac{9}{8} \epsilon_r \epsilon_0 \mu_p \frac{V^2}{L^3} \quad (3.1)$$

is used throughout the work to approximate hole mobility. Least-squares regression is performed to fit every  $J$ - $V$  dataset recorded to (3.1) for electric fields in excess of  $2 \times 10^3$  V/cm. The lower bound is used because, in general, (3.1) does a poor job of describing  $J$  at very low fields because a combination of trap-filling and transient diffusion effects from the onset of space charge accumulation can alter current density characteristics.

Chiguvare et al. observed distinctly linear current densities at low fields which gave way to TF-SCLC at higher fields [57, 58]. Their work combined a single-carrier ohmic behavior following

$$J = q\mu_p p \frac{V}{L} \quad (3.2)$$

with (3.1) to yield an expression

$$J = q\mu_p p \frac{V}{L} + \frac{9}{8} \epsilon_0 \epsilon_r \mu_p \frac{V^2}{L^3}, \quad (3.3)$$

which they used across the entire tested field range [57, 58]. Fitting current density data to this model represented by a simple power series

$$J = aV^2 + bV \quad (3.4)$$

allows one to solve for mobility directly from  $a$ , and then obtain a carrier concentration from  $b$ . This carrier concentration is assumed to be a measure of the actual intrinsic concentration in the material, as it describes conduction before the presence of the space-charge.

The carrier concentration in the device, including the space charge is also easily determined from analysis of current density measurements. The electric field as a function of position along the device length is defined as

$$F(x) = \sqrt{F(0)^2 + \frac{2Jx}{\epsilon_0 \epsilon_r \mu}}, \quad (3.5)$$

where  $F(0)$  is the electric field at the injecting contact, and  $x$  is the position along the length of the active device material with respect to the contact [65]. Using the mobility obtained by fitting either of (3.1) or (3.3),  $F(x)$  can be determined by substitution in (3.5). It then follows from the Poisson equation that

$$p(x) = \frac{\epsilon_0 \epsilon_r}{q} \frac{dF(x)}{dx}, \quad (3.6)$$

where  $p(x)$  is the carrier concentration at position  $x$  [37]. As expected, carrier concentrations calculated using (3.5) and (3.6) are indeed far in excess of those calculated using (3.3) (see Chapter 5). Equations (3.5) and (3.6) arise from TED, and are thus universally applicable. Calculation of  $F(x)$  and  $p(x)$  allows one to quickly determine if conduction is bulk or injection limited. In the case of ohmic contacts, the electric fields calculated along the length of the device will be highly non-uniform, while those calculated for injection limited devices will be nearly constant, varying as  $V/L$  [60].

### **Electrical Testing**

Hole-only devices were tested electrically using a Keithley 236 source-measure unit. Devices were tested by sweeping the applied bias voltage from 0 V to +100 V, from +100 V to -100 V, and back to 0 V in total darkness through 3 cycles. In all cases, the cathode was grounded, and the bias was applied to individual anodes. Voltage was stepped in increments of 5 V, with a 250 ms delay time between measurements to allow for current stabilization. In all experiments, multiple devices were tested on multiple substrates in order to provide a reasonable statistical ensemble, and data from all sweeps were analyzed simultaneously.

Current-voltage characteristics photovoltaic cells (discussed in Chapter 4) were measured in both dark and solar illumination conditions using a Keithley 6487

picoammeter. Solar illumination was provided by an Oriel solar simulator replicating the Air Mass 1.5 Global solar spectrum. All measurements were made in a dark room to prevent interference from ambient illumination. Current densities were measured while sweeping from the applied bias from +5 V to -5 V in 0.25 V increments.

### **Ultraviolet-Visible Spectroscopy**

Many spectroscopic techniques can be applied in the analysis of chemical compounds, but only ultra-violet-based spectroscopic techniques provides key insight into the  $\pi$ -electron system present in conjugated, organic materials [34]. UV-Vis spectroscopy is one such technique that allows one to directly observe the energy required to excite an electron from the valence band to the conduction band, which occurs via the  $\pi$ - $\pi^*$  transition [34]. The complete UV-Vis absorption spectrum can provide insight into the molecular structure of the compound, but the leading-edge absorption energy alone is of interest in this work. The energetic onset of the absorption represents the minimum energy that an incident photon must have in order to initiate a  $\pi$ - $\pi^*$  transition [34]. This energy is approximately equal to the bandgap of the material.

The extent of conjugation within an organic system governs the conductivity [35] and the minimum absorbance energy [34]. Lowering of the absorption onset is indicative of longer effective conjugation lengths [34]. Optically-induced electronic excitation within a single molecule provides a measure of the effective conjugation length in that specific molecule. When molecules of a known type are in a dilute solution, they are relatively isolated from one another electronically, and act as a statistical ensemble of individual molecules. That is to say, the statistical probability of an intermolecular excitation is negligible, all observed excitation is intramolecular, and the observed

leading-edge absorption energy is representative of the average conjugation length along an individual molecule. Comparison of absorbance spectra for the same material with different levels of molecular ordering (i.e. in a solution vs. a thin-film) gives a qualitative view of the extent of electronic, intermolecular interaction. Increases or reductions in the effective conjugation length are indicated by energetic shifting of the absorption onset to lower or higher energies, respectively. Therefore, this technique provides an indirect means of investigating improvements in molecular order of conjugated systems, by examining changes in intermolecular,  $\pi$ -orbital overlapping through changes in effective conjugation length.

UV-Vis spectroscopy was used in this work to determine optical absorbance spectra and approximate band gaps of MEH-PPV and P3HT in various forms. Nanotube samples were examined inside the porous membrane immediately after He plasma etching, with no further modification. Thin-film samples were created by spinning the polymer solutions onto quartz slides at 1000 rpm for 60 s to produce films ~100 nm thick. Residual solvent in the film was allowed to evaporate for several hours prior to use. Nanotube-template samples, along with the thin-film samples, were analyzed by orienting them in the UV/Vis system (Shimadzu UV 1650PC) such that the incident beam was normal to the template of film surface. The absorbance spectra were obtained for optical radiation with energies between 1 eV and 6 eV.

# CHAPTER 4

## CONFINEMENT-INDUCED ENHANCEMENT OF HOLE MOBILITY IN MEH-PPV

### Introduction

Semiconducting and optoelectronic  $\pi$ -conjugated polymers have been studied for a wide range of electronic device applications, most notably light-emitting diodes [10, 11], photovoltaics [13, 14], and thin-film, field-effect transistors [4, 15, 16]. Much interest surrounding these materials has been generated due to the ability to inexpensively process and fabricate devices from them using solution based methods at ambient temperatures with techniques such as inkjet printing, spin coating, and microstamping [17, 18]. However, several key obstacles including very limited exciton lifetimes and poor charge carrier mobilities, due in part to the lack of molecular order in most thin films, must be addressed in order to enhance device performance metrics [35].

With the exception of a few small molecules and various polythiophenes, carrier mobilities above  $10^{-5} \text{ cm}^2 \text{ V}^{-1} \text{ s}^{-1}$  are rarely observed in organic semiconductors [6, 9]. Carrier transport between adjacent organic molecules, which is recognized to occur via hopping mechanisms, is primarily responsible for experimentally observed limitations of carrier mobility [9, 35]. The high-degree of molecular ordering found in materials such as pentacene [33] and self-organizing poly(3-hexylthiophene) (P3HT) leads to greater  $\pi$ - $\pi$  orbital overlapping, enhancing intermolecular transport and thus charge carrier mobilities

[9]. Replication of such ordering in field-effect transistors fabricated from the typically disordered polyfluorene copolymer, F8T2, not only demonstrated that ordering improved carrier transport, but also that mobilities measured when conduction was parallel to the length axis of the molecule were orders of magnitude higher than those perpendicular [36]. This confirmed interchain transport processes to be the limiting factor for F8T2, as was previously shown for P3HT [9]. Aside from the use of substrates that have been coated with alignment layers which act to orient the polymer chains (as in [36]), several other methods have been employed to improve molecular ordering. The most notable efforts relevant to this work include production of nanoscale fibers and tubules from various polymers using techniques such as electrospinning [74], template synthesis [72], and template wetting [102].

Developing a technique known as template synthesis, C. R. Martin demonstrated multiple order of magnitude increases in conductivity in various conducting polymers when chemically synthesized within nanoporous membranes [72]. These increases were attributed to directional orientation of the molecules such that their length axes were parallel to both the length of the fiber and the direction of externally applied electric fields [82]. Later work by Steinhart demonstrated a different process, template wetting nanofabrication, to be a simple, and effective alternative to template synthesis for the creation of such polymer nanostructures [69]. The process utilizes wetting phenomena to create uniform coatings of low surface energy materials, such as many polymer solutions and melts, on porous template materials with high surface energy such as alumina. Nanotubes and nanowires created in this manner have shown enhanced characteristics as

compared to bulk materials, including curvature induced molecular order and crystallinity of polymers within the nanopore [99].

Low- or zero-field hole mobilities in the widely studied, amorphous, photoactive polymer poly(2-methoxy-5-(2'-ethylhexyloxy)-1,4-phenylenevinylene) (MEH-PPV) are typically observed to be on the order of  $10^{-6} \text{ cm}^2 \text{ V}^{-1} \text{ s}^{-1}$ , whether measured by time-of-flight techniques [40] or current density analyses [116]. In the present work, template wetting nanofabrication is used to create MEH-PPV nanotubes with a high degree of molecular order. Optoelectronic properties in these MEH-PPV nanostructures were investigated by examination of temperature dependent, space-charge-limited (SCL) currents, simple photovoltaic devices, and by means of ultraviolet-visible (UV/Vis) spectroscopy.

## **Experimental**

### **Materials**

Anodic porous alumina membranes (Whatman, Anodisc®) were used as templates for nanofabrication. These membranes were 60  $\mu\text{m}$  thick with either 100 or 200 nm nominal pore diameters and pore densities of  $10^{10}$  and  $10^9$  pores per  $\text{cm}^2$  respectively. MEH-PPV (MW 70,000-100,000, as powder) and poly(3,4-ethylenedioxythiophene):poly(styrenesulfonate) (PEDOT:PSS, 1.3% dispersion in  $\text{H}_2\text{O}$ ) were obtained from Sigma-Aldrich, and their structures are presented in Figure 4.1. MEH-PPV wetting solutions were created by dissolving the polymer in chloroform at concentrations of 2 mg/mL for electronic device creation, and 10 mg/mL for SEM sample preparation.

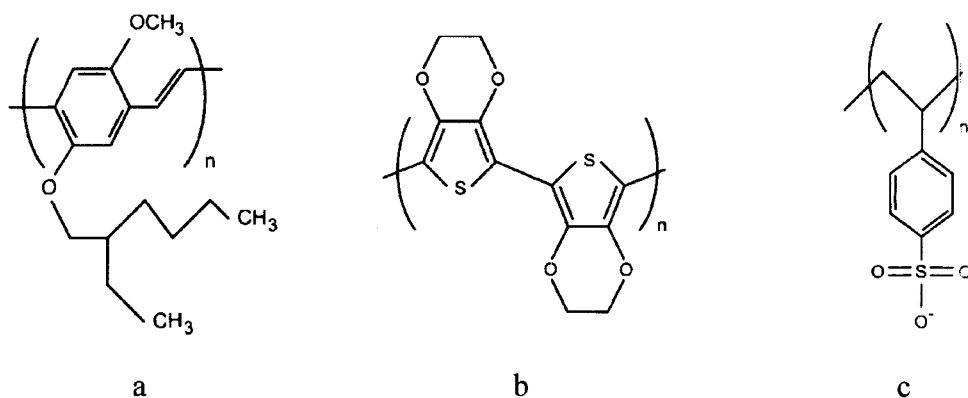


Figure 4.1. Molecular structures of a) MEH-PPV, b) PEDOT, and c) the PSS dopant present in conductive PEDOT:PSS.

## Methods

Porous alumina templates were first wetted with the MEH-PPV wetting solution. The bulk density of the polymer and template porosity were used in conjunction with the assumption of cylindrical pores to calculate the mass of polymer required to make nanotubes with wall thickness of 5 nm or less. Surface tension effects cause the polymer solution to wet the alumina template and penetrate into the nanoscale pores. Samples were left in a fume hood for several hours to allow complete evaporation of the solvent to occur, leaving behind a solid polymer film coating the pore walls of the template. Residual polymer on the outer template surfaces was removed by exposing the substrate surfaces to helium plasma at 200 mtorr. Given the low temperature and short time of the etching process, along with the high aspect ratio of the pores, the plasma has significant affect on the polymer embedded within the template [115]. In order to enable imaging of the resulting polymer nanotubes with scanning electron microscopy, several samples were etched in 25 wt. % aqueous KOH to selectively remove part of the alumina template. Examples of resulting micrographs are shown in Figure 4.2. The high yield of

the process is illustrated in a), while the tubular nature and approximate diameter (100 nm pictured) of representative nanotubules is illustrated in b).

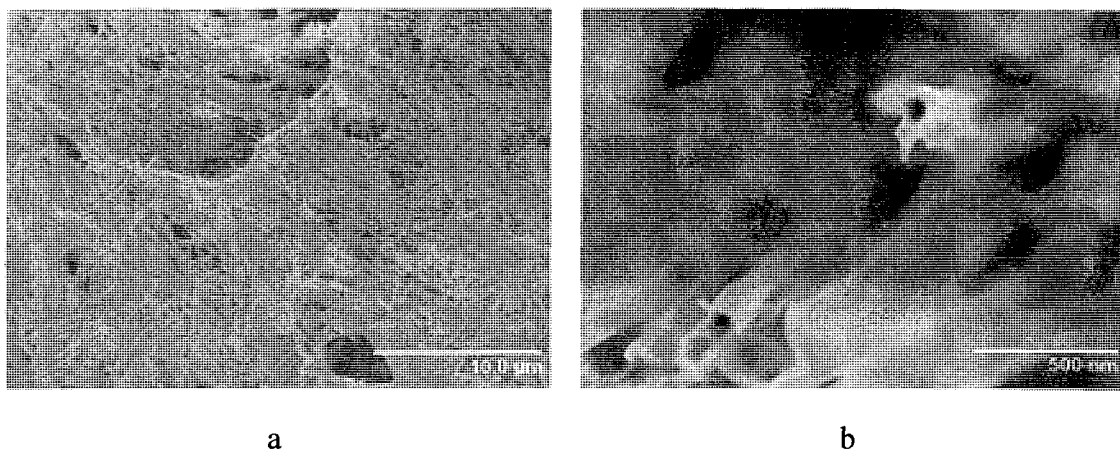


Figure 4.2. Scanning-electron micrographs of a) a mat of 100 nm MEH-PPV nanotubes, and b) open-ended 100 nm MEH-PPV nanotubes.

The examination of SCL currents in conjugated polymers has proven to be a reliable and effective means of investigating carrier transport in conjugated polymers [42, 44], and was used here to investigate these properties in the MEH-PPV nanotubes. The trap-free SCL conduction (TF-SCLC) model suggests current densities vary quadratically with the applied bias,  $V$ , by the following relation

$$J = \frac{9}{8} \epsilon_0 \epsilon_r \mu_p \frac{V^2}{L^3}, \quad (4.1)$$

where  $\epsilon_0 \epsilon_r$  is the electrical permittivity of the material,  $\mu_p$  is the hole mobility, and  $L$  is the device length, given that the barriers to charge carrier injection does not exceed a few 0.1 eV [42, 51].

In order to ensure space-charge-limited, hole-only conduction, the contact material used to form both the anode and cathode must have a work function,  $\phi_m$ , near the energy of the top of the polymer valence band,  $E_V \approx 5.3$  eV, such that the hole injection

barrier is minimized at both contacts [43]. Electrode materials of Au ( $\phi_m \approx 5.1$  eV) and indium-tin-oxide (ITO) ( $\phi_m \approx 4.8$  eV) each provide minimal hole injection barriers for MEH-PPV, while simultaneously maximizing the barrier to electron injection [65]. Hole-only devices were created by evaporating 150 nm thick Au electrodes on each side of the wetted templates after completion of the plasma etch, creating device structures as illustrated in Figure 4.3a. A shadow mask was used to create multiple contacts on the cathode side of the template, producing multiple devices per substrate.

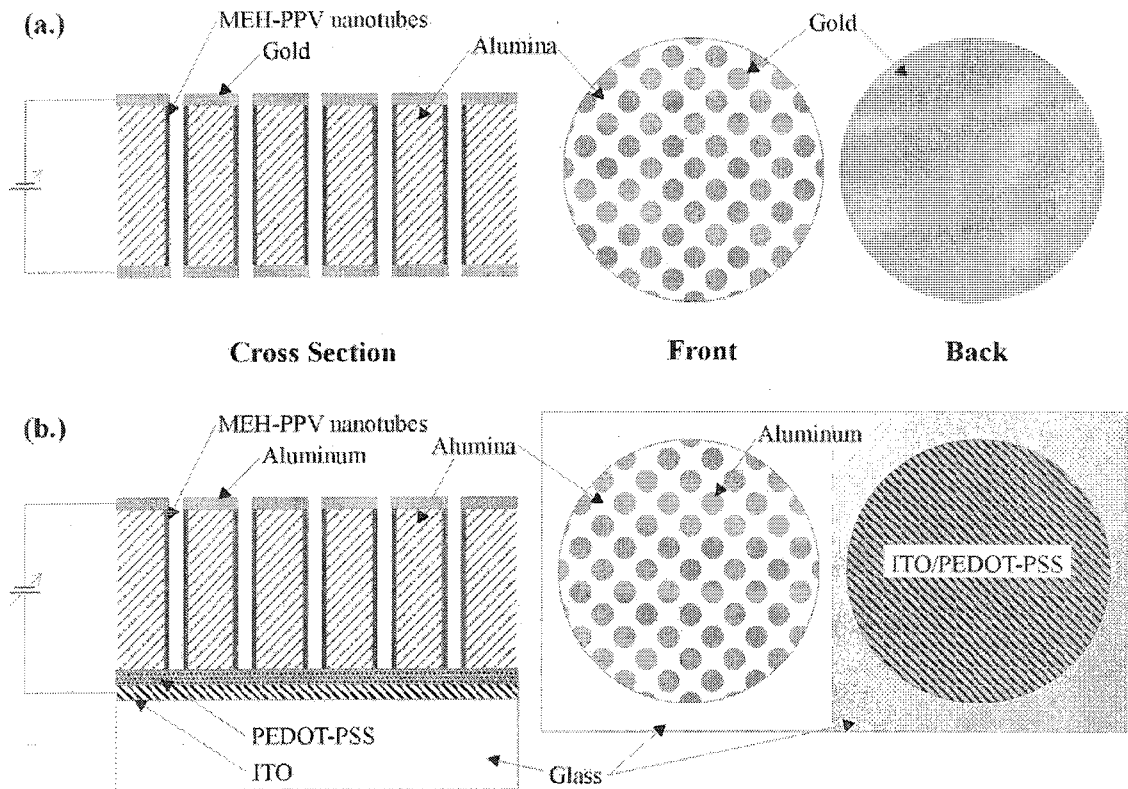


Figure 4.3. Device structures for a) hole-only and b) photovoltaic devices constructed from MEH-PPV nanotubes.

Optoelectronic properties of the MEH-PPV nanotubes were evaluated using ultraviolet-visible (UV-Vis) spectroscopy, and by investigation of a simple solar cell. UV-Vis spectroscopy was performed using a Shimadzu UV 1650PC system in order to determine the minimum optical absorption energies of the material in various forms. Nanotube-template samples, along with the thin-film samples prepared by spin coating on quartz slides, were analyzed by orienting them in the UV-Vis system such that the incident beam was normal to the largest template or film surface.

Solar cells were fabricated by forming 150 nm thick aluminum cathodes on template surfaces by thermal evaporation. Aluminum cathodes are chosen in this device structure to improve charge separation characteristics in the device. In this respect, the device structure is fundamentally different from the hole-only structure, as both carriers are present in the device. The device was completed by contacting the opposite side of the template with an indium-tin-oxide (ITO) coated glass substrate that had been spin coated with a 50 nm layer of conducting PEDOT:PSS immediately prior. The PEDOT:PSS layer acts as a conductive adhesion layer, producing a device structure illustrated in Figure 3b, similar to the one previously discussed, but here with ITO/PEDOT:PSS coated glass forming the anode opposite an aluminum cathode. For comparative purposes, traditional sandwich structured thin-film devices were also fabricated by spin coating 100 nm films of MEH-PPV onto the ITO/PEDOT:PSS coated glass. Again, individual devices were formed by patterning of a 150 nm thick Al cathode. Solar illumination was provided by an Oriel solar simulator replicating the Air Mass 1.5 Global solar spectrum. Photovoltaic behavior of the devices was investigated by measuring  $I$ - $V$  responses of both thin-film and nanotube based devices.

## Results and Discussion

Electric fields applied to polymer thin-film devices are typically far in excess of  $10^5$  V/cm, while those examined in this work are significantly lower. At high electric fields, measured current densities often deviate from those described by the TF-SCLC model, and carrier transport has been well described by the following field dependent mobility [40, 45, 63]

$$\mu(F, T) = \mu_0(T) \exp(\gamma\sqrt{F}), \quad (4.2)$$

where  $\mu_0(T)$  is a temperature dependent, low-field mobility and  $\gamma$  is a constant. In the low field regime, the exponential term in (4.2) becomes negligible, and  $\mu_0(T)$  becomes well described by the mobility in the TF-SCLC model. Observed current densities in the hole-only devices for both 100 nm and 200 nm MEH-PPV nanotubes are illustrated in Figure 4.4, along with corresponding least-square fits to TF-SCLC.

Conduction is well described by TF-SCLC throughout much of the test region, but deviations are observed at the lowest applied electric fields. Higher order field dependence of current density at these very low fields is indicative of the presence of some degree of hole trapping in the polymer. This behavior was not observed for above  $\sim 2 \times 10^3$  V/cm. Similar observations of hole trapping have been described elsewhere in very thick layers of PPV [44], and it is likely that the relatively thick nature of our device structure (60  $\mu\text{m}$  nanotubule length) explains these observations. Further, the slow rise to TF-SCLC behavior suggests that holes may be trapped throughout a broad energetic distribution, similar to previous observations by Blom for electron trapping in PPV [42].

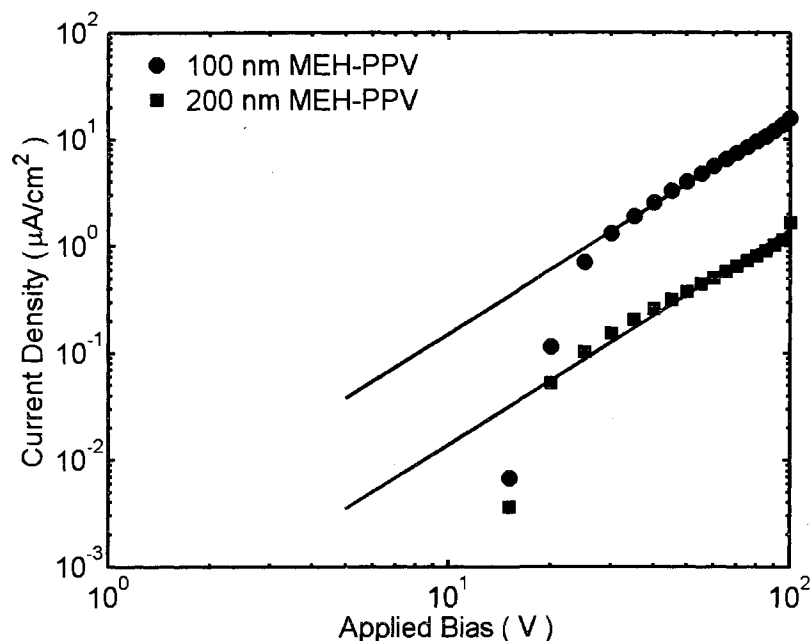


Figure 4.4.  $J$ - $V$  characteristics observed in hole-only devices fabricated from both 100 nm and 200 nm MEH-PPV nanotubes.

Hole mobilities were calculated by fitting the current density measurements obtained at electric fields above  $2 \times 10^3$  V/cm to the TF-SCLC model. Here, the device thickness was taken as the full  $60 \mu\text{m}$  thickness of the polymer coated nanoporous template. The relative permittivity,  $\epsilon_r$ , of MEH-PPV used in this calculation was found to be approximately 3 via ellipsometry [117], in agreement with values used elsewhere [42].

Calculated hole mobilities for 200 nm diameter nanotubes were found to be on the order of  $10^{-5} \text{ cm}^2 \text{ V}^{-1} \text{ s}^{-1}$ , while those of 100 nm nanotubes were two orders of magnitude higher,  $\sim 10^{-3} \text{ cm}^2 \text{ V}^{-1} \text{ s}^{-1}$ , representing significant improvement in carrier transport versus thin films ( $\sim 10^{-6} \text{ cm}^2 \text{ V}^{-1} \text{ s}^{-1}$ ) [116], and demonstrating an inverse relation between carrier mobility and pore diameter. This inverse relationship has been documented elsewhere for polypyrrole, where the conductivity of polymer synthesized within larger pores showed slight enhancement over conductivities in thin films, but increased exponentially as pore

diameter was reduced to submicron scales [72]. It is expected that the greater confinement and radius of curvature results in increased packing and molecular order of the polymer molecules resulting in greater  $\pi$ - $\pi$  overlap and reduced barriers to interchain transport.

For most charge carrier hopping models, the low-field mobility,  $\mu_0(T)$ , is thermally activated, and is well described an Arrhenius model of the form

$$\mu_0(T) = \mu_0 \exp\left(\frac{-\Delta}{kT}\right), \quad (4.3)$$

where  $\mu_0$  is a prefactor and  $\Delta$  is an activation energy [26, 63]. Current-voltage characteristics were obtained for temperatures ranging from 173 K to 295 K by submerging samples in liquid nitrogen for several minutes, and then measuring current as the samples slowly returned to room temperature. Nonlinear regression to fit this data to (4.3) for 100 nm diameter, hole-only nanotube devices gives  $\mu_0 = 365 \text{ cm}^2 \text{ V}^{-1} \text{ s}^{-1}$  and  $\Delta = 0.26 \text{ eV}$ . Resulting mobilities are shown in Figure 4.5.

The measured values of  $\mu_0(T)$  at temperatures above 250 K lie above those predicted by the Arrhenius model, suggesting that carrier transport in this temperature range may not be dominated by such thermally activated hopping mechanisms. Like calculations by Blom et al. for thin films of a similar PPV derivative resulted in an activation energy of 0.48 eV [63], significantly greater than that observed for the nanotube devices in this work. This reduction in activation energy is most likely a result of a high degree of molecular ordering within the nanopore, consistent with higher than expected values of mobility observed.

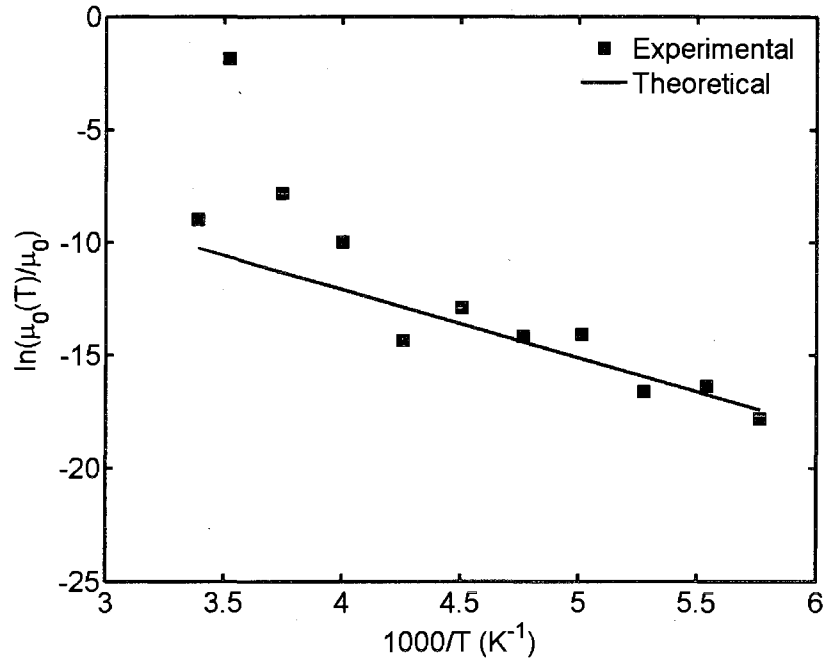


Figure 4.5. Arrhenius behavior of the low-field hole mobility in MEH-PPV nanotubes.

Figure 4.6 shows the leading edge of the UV-Vis absorption spectra, corresponding to  $\pi$ - $\pi^*$  transitions, for MEH-PPV in various forms. The band energy decreases slightly from 2.2 eV for a solution to 2.1 eV for a thin film cast from this solution. This observed red shifting is even more pronounced in nanotube based samples, as leading-edge absorption energies of 1.6 eV and 1.8 eV were recorded for 100 nm and 200 nm nanotubes, respectively. The red shift is consistent with the hypothesis that greater molecular ordering and  $\pi$ -orbital overlapping exist within the nanopore, as it suggests an increase in the effective conjugation length [34].

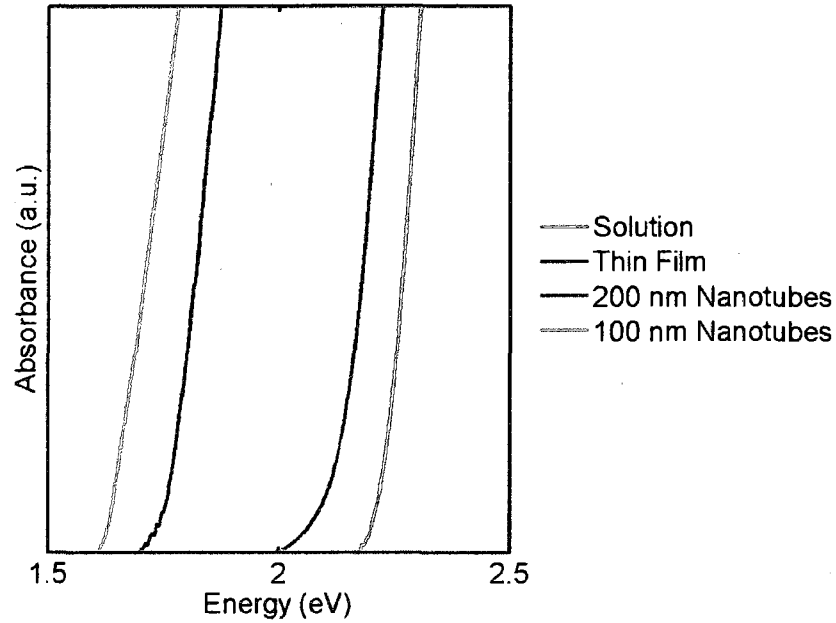


Figure 4.6. Leading edges of absorption spectra obtained for MEH-PPV in various forms created from a chloroform solution.

Photocurrent generation was observed in both 100 nm and 200 nm nanotube-based photovoltaic devices, demonstrating retention of the photoactive properties of MEH-PPV. Calculation of photovoltaic fill factor,  $FF$ , is a typical means of characterizing solar cell design and performance [37]. The measurement represents the ratio of actual to theoretically producible power (illustrated in Figure 4.7), and is described by

$$FF = \frac{V_{mp}I_{mp}}{V_{oc}I_{sc}}, \quad (4.4)$$

where  $V_{mp}$  and  $I_{mp}$  are the voltage and current at maximum power output,  $V_{oc}$  and  $I_{sc}$  are the open-circuit voltage and short-circuit current [118]. The thin-film devices produced average fill factors of 22%, comparable to values reported elsewhere of ~30% for similarly structured devices [14]. However, much higher fill factors were observed for 100 nm and 200 nm nanotube based devices, of 67 % and 59 % respectively. Current

density characteristics of MEH-PPV nanotube based photovoltaics are presented in Figure 4.8. Observations of increased fill-factor are consistent with the improvements in carrier mobility [118].

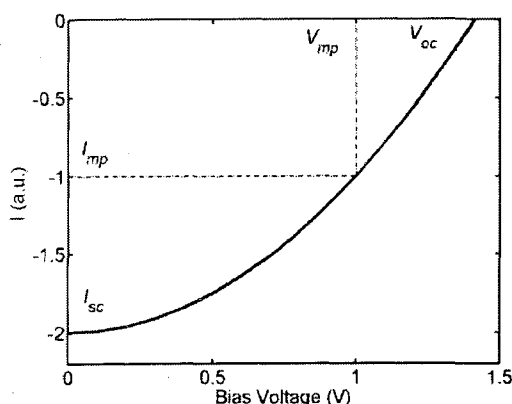


Figure 4.7. Illustration of the photovoltaic fill-factor calculation.

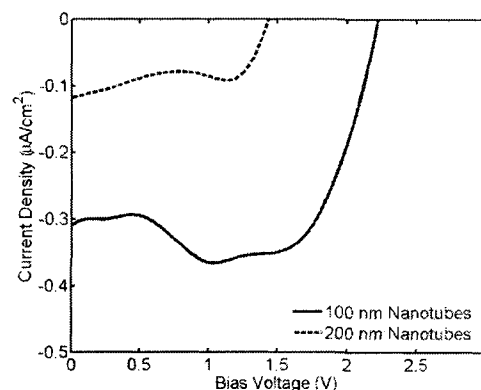


Figure 4.8. Photocurrent densities observed in MEH-PPV nanotube-based photovoltaic cells.

It is not clear exactly how the polymer chains are arranged within the membrane, as the case can be made for either perpendicular or parallel alignment with the nanotube axis. From previous observations with the template wetting process, molecules are expected to align perpendicular to the nanopore wall [99]. Given this type of structure, one would expect to observe enhanced  $\pi$ -orbital overlapping as observed in polythiophenes [9]. This should lead to improved interchain transport, which has been determined to be the rate limiting factor of bulk mobilities in other conjugated polymers [36]. It is also possible that the molecules align parallel to the tube axis as observed with polyacetylene in the template synthesis process [82], which would improve mobility by maximizing the distance free carriers travel along a single polymer chain. Carrier transport along the direction of the polymer chain is generally accepted to be much faster

than interchain hopping processes [36], and a parallel alignment would greatly reduce the frequency of these more difficult transport processes. Theoretical analysis has demonstrated that carrier mobilities along the MEH-PPV chain can achieve values on the order  $10 \text{ cm}^2 \text{ V}^{-1} \text{ s}^{-1}$  even though conjugation may be interrupted as frequently as every  $100 \text{ \AA}$  [35].

### **Conclusions**

Template wetting nanofabrication has been used to produce nanotubes from the semiconducting polymer MEH-PPV, and these structures have demonstrated electronic properties superior to those observed in thin-films of the same material. Current density characteristics for the nanotubes were found to be in good agreement with space-charge-limited conduction models, and were indicative of minor hole trapping in shallow energy levels with an asymptotic approach to the trap-free limit at increased electric fields. Hole mobilities in nanotubule devices were found to be orders of magnitude higher than those measured in thin films. Further, minimum optical absorption were reduced in the nanotube structure, increased intermolecular interaction leading to an extension of the effective conjugation length in the material. Photovoltaic behavior observed in the nanotube based devices demonstrated significant fill factor improvement when compared with similar thin-film devices. Hole mobility and fill factor both increase inversely proportional to the nanopore diameter, supporting the proposed presence of confinement-induced, molecular ordering in the nanostructured MEH-PPV.

**CHAPTER 5**

**SOLVENT EFFECTS ON SOLUTION-BASED**

**TEMPLATE WETTING FABRICATION**

**WITH SEMICONDUCTING**

**POLYMERS**

**Introduction**

Poor hole and electron mobilities inherent in disordered systems of conjugated, semiconducting polymers have been shown to limit efficiencies and performance in electronic devices such as polymer light-emitting diodes [42]. Improving electronic transport in these materials has been the focus of much research, with specific interest on enhancement of molecular order. Interchain hopping of carriers in semiconducting polymer systems has been demonstrated as the rate limiting step for carrier transport in traditional, thin-film devices, and is strongly dependent on molecular ordering [36]. Exceptionally high hole mobilities have been observed in polymer systems in which interchain  $\pi$ -orbital overlapping is enhanced [9, 36].

Morphology and molecular ordering, and consequently many other properties, often depend on the solvent used to dissolve the bulk polymer in the fabrication process [39, 119], as chain conformation in the solvent is often translated into the film [120]. However, the exact nature of these solvent effects varies depending on the polymer

system itself, and the nature of the fabrication process. For example, for polythiophene systems, solvent volatility seems to be quite important [39]. Many polythiophenes, including P3HT, have rigid, rod-like molecular structures which exhibit a self-organizing property that results in a high degree of  $\pi$  stacking between molecules [6, 9, 121, 122]. This ordering is most pronounced when devices are created by drop-casting the polymer, rather than spinning it, and is attributed to slower evaporation of the solvent [39]. Slower evaporation of solvent in turn allows molecules more time to move freely and arrange themselves [39] into presumably thermodynamically favored semi-crystalline structures, resulting in improved carrier transport properties [9].

Other polymers, like poly(phenylene vinylene)s do not exhibit rigid molecular structures [123], and often form amorphous agglomerates in poor solvents [124]. Molecular simulations show that the radius of gyration of a MEH-PPV molecule is significantly larger in chloroform than in toluene; pointing to straightened molecules in chloroform and coiled species in toluene [123]. For MEH-PPV, the effective conjugation length in the polymer system is expected to be highest when the molecule is straightened by the solvent, and is evidenced by red-shifting of optical absorbance spectra [124]. This phenomena is typically observed when comparing UV-Visible absorbance spectra of cast thin-films and solutions. Absorbance spectra of the solutions, which are significantly more disordered, are generally blue-shifted with respect to similar spectra for films. Extended effective conjugation lengths lead directly to improved carrier transport [35], and it thus becomes apparent that a solvent's ability to uncoil the polymer molecule are also of importance.

Chapter 4 demonstrated solution-based template wetting as an effective means of creating electronic nanotubes from MEH-PPV with both improved positive charge carrier (hole) transport properties and retention of optoelectronic behavior. Here, we examine the effects of solvent selection on solution-based template wetting procedures with both MEH-PPV and P3HT. Electronic transport within these structures is characterized by analysis of current-voltage characteristics, internal electric field profiles, and internal distributions of carrier concentration. UV-Visible spectroscopy is used to make quantitative approximations of electronic bandgaps and qualitative assumptions about effective conjugation lengths in the nanostructured polymer system.

## **Experimental**

### **Materials**

Regioregular poly(3-hexylthiophene-2,5-diyl) with > 98.5 % head-to-tail linkages (P3HT) and poly[2-methoxy-5-(2-ethylhexyloxy)-1,4-phenylenevinylene] (MEH-PPV,  $M_{n,avg}$  70,000 – 100,000) were obtained from Sigma-Aldrich and used as received. Solutions of each polymer were created by dissolution in either of chlorobenzene (CB), chloroform (CF), tetrahydrofuran (THF), or toluene (TOL) at a concentration of 2 mg/ml. Commercially available anodic porous aluminum oxide membranes (Whatman Co.) were used as templates. Templates were 60  $\mu\text{m}$  thick with monodisperse pore diameters of 100 nm and  $10^{10}$  pores per  $\text{cm}^2$ .

### **Methods**

Templates were wetted with solution volumes such that nanotube wall thicknesses should not exceed 5 nm, ensuring that most polymer deposited on the membrane will be from the precursor layer at the wetting front [112, 113]. With the exception of MEH-PPV

in chlorobenzene (MEH-PPV/CB), rapid spreading of the precursor film was immediately observed, and residual solvent was allowed to evaporate over the course of ~18 hours. MEH-PPV/CB samples appeared to leave thick films of residual polymer on the template surface, which is discussed in detail below. The wetting procedure was repeated so that multiple substrates were created for each of the eight sample groups. Polymer deposited on the macroscopic surfaces of the templates was removed by etching with low pressure helium plasma before further processing. Short etch times and high pore aspect ratios suggest that the plasma cannot significantly affect the polymer incorporated within the nanoporous membrane. Scanning electron microscopy was performed after the alumina membrane was partially removed from several samples by etching in 25 wt. % aqueous KOH. Note that only samples used for SEM analysis underwent this wet etching process. Resulting micrographs for both P3HT and MEH-PPV nanotubes made with wetting solutions using chloroform as the solvent are shown in Figure 5.1.

Electronic devices were fabricated by depositing metallic contacts on each side of the templates, forming device structures as illustrated in Figure 4.3a with either MEH-PPV nanotubes or P3HT nanotubes. As noted in the previous chapter, the work function,  $\phi_m$ , of the chosen contact material dictates the conduction behavior in the devices [60]. If the anode and cathode are formed from metals whose  $\phi_m$  is within a few 0.1 eV of the top of the valence band,  $E_V$ , space-charge-limited (SCL) hole conduction will dominate in the device, allowing for accurate examination of the hole transport properties [43]. Here, 150 nm thick Au ( $\phi_m \approx 5.1$  eV) [47] electrodes were formed on each side of the wetted membranes after the plasma etch was completed. This device electrode configuration

minimizes hole injection barriers,  $\phi_{Bp}$ , for MEH-PPV ( $E_V \approx 5.35$ - $5.40$  eV,  $\phi_{Bp} = 0.25$ - $0.30$  eV)[47] and P3HT ( $E_V \approx 5.2$  eV,  $\phi_{Bp} \approx 0.1$  eV) [48], while simultaneously maximizing barriers for electron injection. Note that we assume conduction is dominated by a single carrier (in this case, holes) throughout this work.

For spectroscopic analysis, templates were used directly after plasma etching. UV-Vis spectroscopy was performed using a Shimadzu UV 1650PC system in order to determine optical absorbance spectra and approximate band gaps of the material embedded within the nanoporous membranes. Nanotube-template samples were analyzed by orienting them in the UV-Vis system such that the incident beam was normal to the template or film surface. Multiple samples were created for this purpose, and averaged spectra were analyzed.

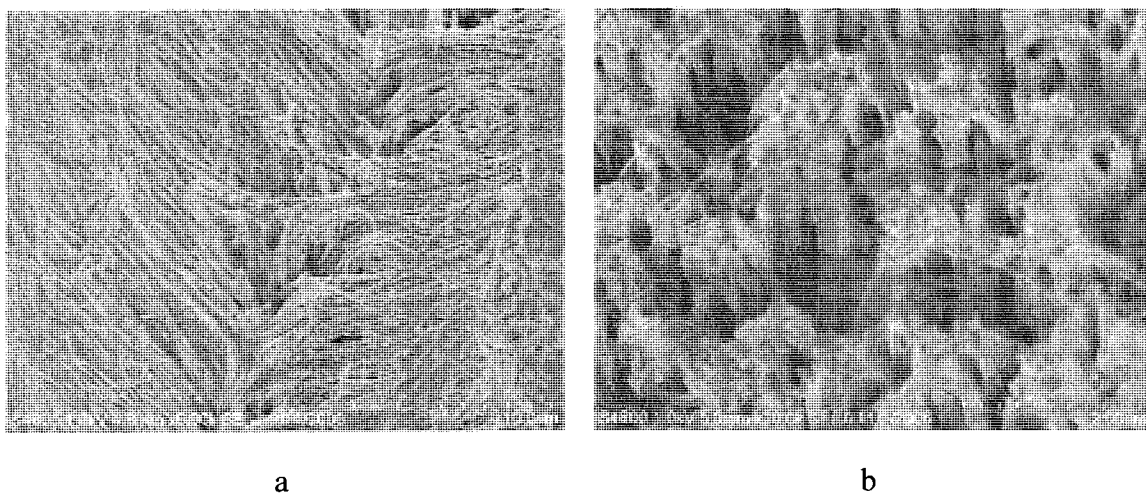


Figure 5.1. Scanning electron micrographs of a) MEH-PPV and b) P3HT nanotubes created using template wetting in 100 nm diameter alumina nanopores with chloroform as the solvent for the wetting solution.

## Device Model

Organic optoelectronic devices, such as light-emitting diodes and photovoltaic cells, are typically fabricated by sandwiching the organic layer between two conducting materials. In such structures, current density behavior is defined by both the injection properties at the contact/organic interface and the bulk transport properties of the organic material itself. Charge carriers are injected into the organic layer by means of either thermionic emission over the injection barrier, tunneling through the barrier, or a combination of the two [41]. Bulk transport properties of the material are in turn described by the free carrier mobility and the effective density of trapping states within the material [42]. While the two processes occur simultaneously under an applied bias, the least efficient mechanism will dominate the observed current density characteristics. Conduction in semiconducting polymers is generally dominated by injection mechanisms for low applied electric fields, but becomes dominated by the bulk properties at higher fields due to the buildup of injected space charge in the active layer [42].

Provided that ohmic contact with the organic layer is established and  $\phi_b$  is very small, the injecting electrodes supply a theoretically limitless supply of free carriers, which may be injected into the organic material. While this process dominates, the current density,  $J$ , is well described by a linear dependence with applied bias,  $V$ , following

$$J = qp_i\mu_p \frac{V}{L}, \quad (5.1)$$

where  $q$  is the electronic charge,  $p_i$  is the intrinsic free carrier concentration,  $\mu_p$  is the hole carrier mobility, and  $L$  is the device length or thickness [42].

Due to poor bulk transport properties, organic electronic materials are often incapable of conducting all injected charge across the device length. The difference between the injected charge and that actually transported by the material, known as space charge, becomes quite large as bias increases. The presence of space charge in the device establishes highly non-uniform internal electric fields which begin to dominate injection and limit current flow through the device [60]. Current densities in this operating regime are well described by the trap-free, space-charge-limited conduction (TF-SCLC) model

$$J = \frac{9}{8} \epsilon_0 \epsilon_r \mu_p \frac{V^2}{L^3}, \quad (5.2)$$

where  $\epsilon_0 \epsilon_r$  represents the dielectric permittivity.[51] SCLC behavior has been commonly observed in thin films of both MEH-PPV [41, 43, 45] and P3HT [57, 58, 62].

## **Results and Discussion**

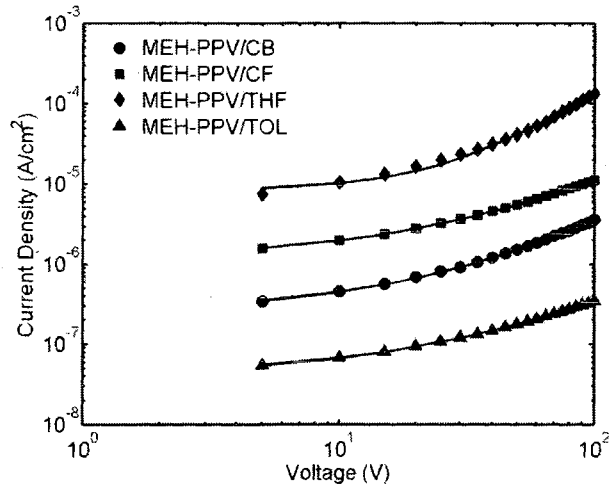
### **Electrical Characterization**

Current densities in the nanotube-based electronic devices were found to be in good agreement both the space-charge-limited conduction models described above, as  $R^2$  values for the least-squares-regression were in excess of 0.995 for the standard. Values of hole mobility were obtained by considering both the TF-SCLC behavior of current density of (5.2) individually at the upper end of the tested voltage range, and in linear combination with the ohmic behavior described in (5.1) following

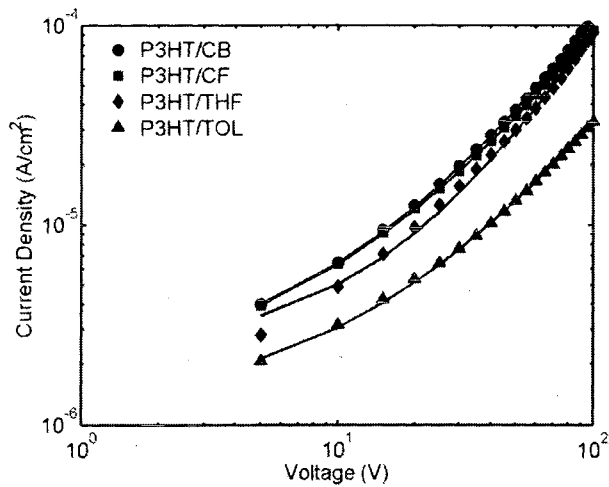
$$J = qp_i \mu_p \frac{V}{L} + \frac{9}{8} \epsilon_0 \epsilon_r \mu_p \frac{V^2}{L^3} \quad (5.3)$$

throughout the entire test region. Here,  $\epsilon_r$  is taken to be 3, which is commonly done for both PPVs [42] and polythiophenes [58]. Current densities for MEH-PPV devices vary strongly with solvent, while current densities in P3HT samples were relatively

independent of solvent. Resulting average current densities for each polymer are illustrated in Figure 5.2, along with corresponding fits to (5.3).



a



b

Figure 5.2. Average  $J$ - $V$  characteristics for electronic devices fabricated from 100 nm nanotubes of a) MEH-PPV and b) P3HT, created by template wetting using various solvents. Accompanying solid lines represent least-squares-regression fits to (5.3).

Carrier concentrations were determined using (5.3) by first solving for the mobility from the regression coefficient of the  $V^2$  term, then substituting into the coefficient of the  $V$  term and solving for  $p_i$  following [58]. Carrier concentrations found in this manner are assumed to be intrinsic, i.e. the true number of free carriers in the material at thermal equilibrium before the accumulation of space charge becomes significant. In this case, one free hole is extracted at the cathode for every one injected at the anode. The resulting average mobilities,  $\mu_{p,avg}$ , carrier concentrations,  $p_{avg}$ , and standard deviations,  $\sigma$ , thereof are shown in Table 5.1. In all cases, (5.3) yielded more conservative estimates of hole mobility than were obtained using (5.2), but the trends are consistent between the two models.

Table 5.1. Hole mobility and concentration determined from analysis of space-charge-limited currents in MEH-PPV and P3HT nanotube-based electronic devices.

Sample Group	Following (5.2)		Following (5.3)		
	$\mu_{p,avg}$ ( $\text{cm}^2 \text{V}^{-1} \text{s}^{-1}$ )	$\sigma_{\mu,avg}$ ( $\text{cm}^2 \text{V}^{-1} \text{s}^{-1}$ )	$\mu_{p,avg}$ ( $\text{cm}^2 \text{V}^{-1} \text{s}^{-1}$ )	$\sigma_{\mu,avg}$ ( $\text{cm}^2 \text{V}^{-1} \text{s}^{-1}$ )	$p_{avg}$ ( $\text{cm}^{-3}$ )
MEH-PPV/CB	3.92E-04	2.03E-04	3.24E-05	1.64E-05	2.51E+13
MEH-PPV/CF	1.20E-03	4.21E-04	2.39E-04	8.18E-05	7.71E+12
MEH-PPV/THF	1.24E-02	8.12E-03	9.31E-03	9.65E-03	4.03E+12
MEH-PPV/TOL	3.58E-05	1.69E-05	5.41E-06	2.04E-06	1.29E+13
P3HT/CB	1.33E-02	4.36E-03	7.67E-03	2.81E-03	1.82E+12
P3HT/CF	1.19E-02	4.85E-03	5.39E-03	2.48E-03	1.99E+12
P3HT/THF	8.65E-03	3.99E-03	6.70E-03	2.55E-03	1.97E+12
P3HT/TOL	3.31E-03	1.15E-03	1.38E-03	5.52E-04	2.77E+12

Carrier concentrations calculated in this manner are not representative of those within the material when space charge is included. Those concentrations are expected to be orders of magnitude higher, making the intrinsic concentration negligible. It has been

shown theoretically that carrier densities in Au/MEH-PPV/Au devices, where conduction is primarily described by SCLC, can be in excess of  $10^{16} \text{ cm}^{-3}$  near the injecting electrode, and decays across the length of the device [60]. The presence of space charge in the active layer leads to highly non-uniform internal electric fields,  $F$ , following

$$F(x) = \sqrt{F(0)^2 + \frac{2Jx}{\epsilon_0 \epsilon_r \mu_p}}, \quad (5.4)$$

where  $F(0)$  is the electric field at the injecting contact (in this case the anode),  $x$  is the distance from the injecting contact,  $\epsilon_0 \epsilon_r$  is the electric permittivity of the active medium, and  $\mu_p$  is the hole mobility [65]. Substituting the spatial derivative of the internal electric field into the Poisson equation

$$p(x) = \frac{\epsilon_0 \epsilon_r}{q} \frac{dF(x)}{dx} \quad (5.5)$$

provides the carrier concentration as a function of the distance from the injecting electrode [65].

Electric field distributions were calculated for all eight sample groups at various voltages using (5.4). The more conservative mobilities determined from regression of data to (5.3) were used, and  $F(0)$  was fixed equal to  $V_{\text{applied}}/L$  for consistent treatment of the combination of ohmic and space-charge-limited conduction processes. The distribution of carrier concentration,  $p(x)$ , was calculated using a forward difference approximation for the first derivative of the electric field,  $F'$ , following

$$F'(x_i) = \frac{F(x_{i+1}) - F(x_i)}{\Delta x} \quad (5.6)$$

with  $\Delta x = 0.01 \text{ nm}$ . Figure 5.3 illustrates results of these calculations for all sample groups at 90 volts, where SCL behavior is expected to be dominant.

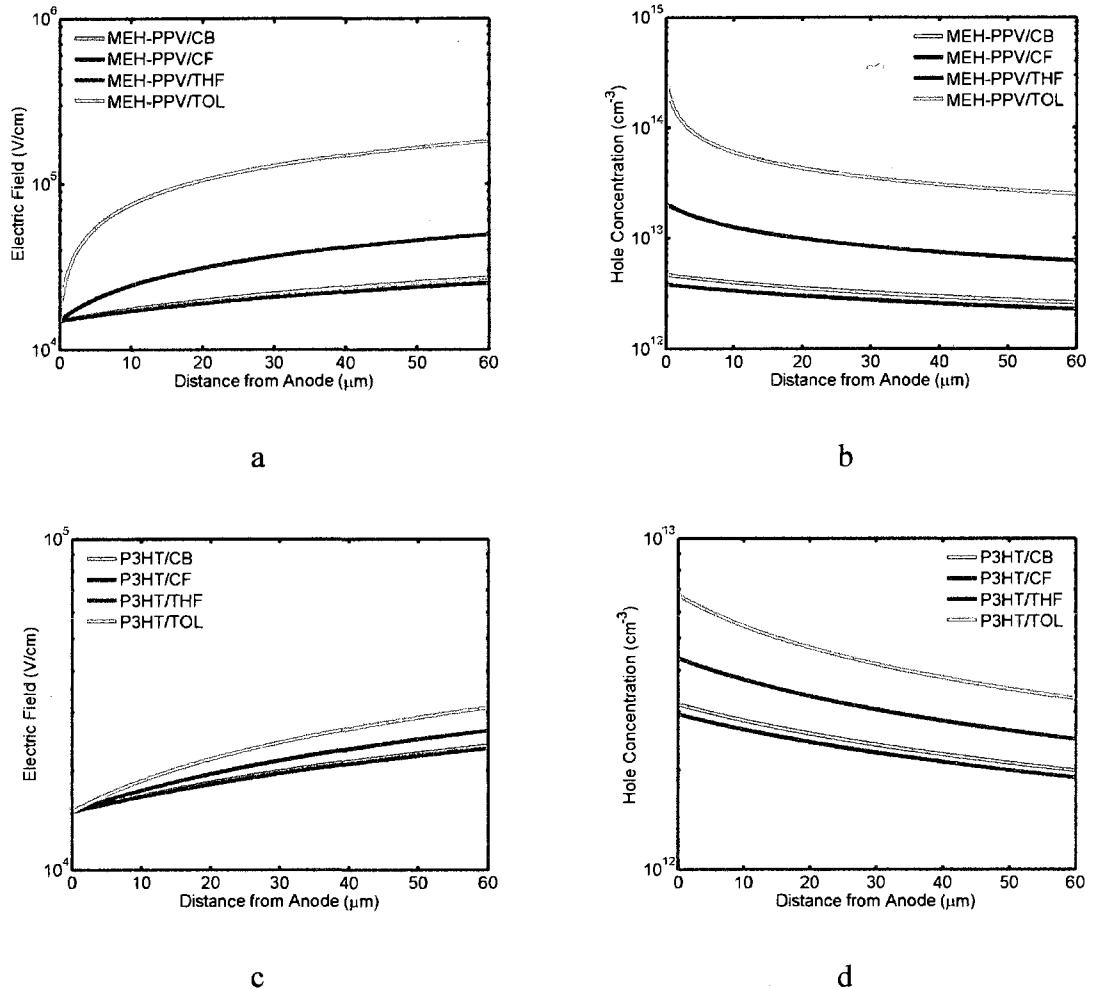
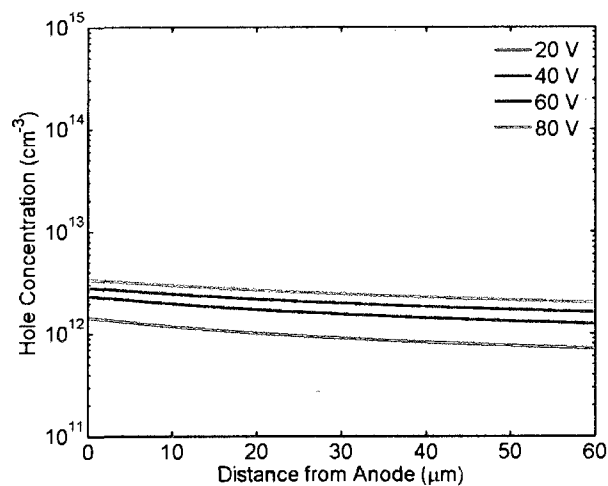


Figure 5.3. Internal electric field distributions for a) MEH-PPV and c) P3HT nanotube-based electronic devices operating at 90 V. Corresponding hole concentration distributions for b) MEH-PPV and d) P3HT are also illustrated.

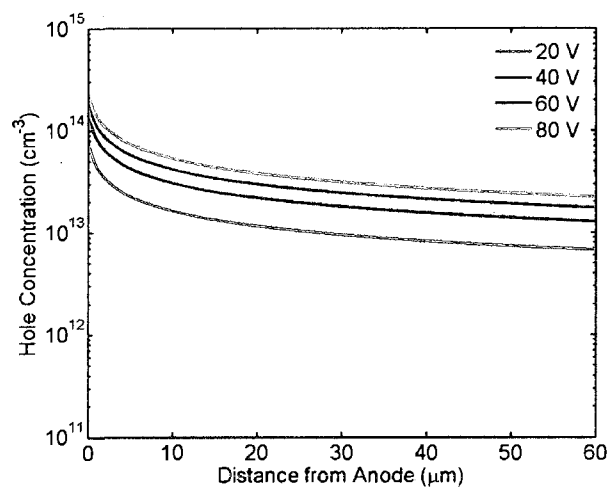
With the exception of the MEH-PPV/CB sample group, significantly more deviation of the carrier concentration and electric field distributions across the device length are observed for sample groups with lower current densities and hole mobilities. The high mobilities measured in the P3HT samples prevent formation of significant space charge accumulation, leading to approximately constant carrier concentration and electric field profiles. Further, hole concentrations calculated in this manner are in good agreement with the intrinsic values obtained for P3HT devices using (5.3).

The broad solvent dependent variation of hole mobility observed in MEH-PPV samples likewise results in a wide range of internal  $F(x)$  and  $p(x)$  profiles. Average hole mobility in MEH-PPV/TOL devices was found to be  $\sim 5 \times 10^{-6} \text{ cm}^2 \text{ V}^{-1} \text{ s}^{-1}$ , the lowest experimentally observed value of all sample groups, while the value determined for MEH-PPV/THF devices was approximately  $9 \times 10^{-3} \text{ cm}^2 \text{ V}^{-1} \text{ s}^{-1}$ . The carrier concentrations observed near the anode in MEH-PPV/TOL samples are approximately two orders of magnitude higher than the intrinsic concentrations calculated using (5.3), and both the  $F(x)$  and  $p(x)$  profiles are highly non-uniform. However,  $F(x)$  and  $p(x)$  profiles calculated for MEH-PPV/THF samples, where the highest mobilities in MEH-PPV were observed, are much more uniform, and carrier concentrations are only slightly in excess of the intrinsic calculations.

The model described by (5.3) describes a transition from an ohmic behavior that becomes dominated by SCL conduction as applied bias is increased. Based on this model, the magnitude of the carrier concentrations determined using (5.5) are expected to be approximately equal to the intrinsic values obtained from (5.3) at low applied bias. As the applied bias is increased, one then expects an increase in the carrier concentration, especially near the injecting contact, as the space charge begins to accumulate and SCL conduction becomes important. This behavior was observed in all sample groups, but variation in P3HT samples is very limited. Carrier concentrations calculated using (5.5) were very similar to the intrinsic values obtained with (5.3) when  $V$  was fixed at 20 V, then increase as applied bias is increased. Voltage dependent  $F(x)$  and  $p(x)$  profiles for MEH-PPV/THF and MEH-PPV/TOL sample groups are provided in Figure 5.4.



a



b

Figure 5.4. Voltage dependent carrier concentration profiles for a) MEH-PPV/THF and b) MEH-PPV/TOL 100 nm nanotube-based electronic devices.

### UV-Visible Spectroscopy

Examination of the leading edge of UV-Visible absorption provides information about molecular ordering within the polymer system, as discussed in Chapters 3 and 4. Energetic reduction of the absorption edge generally points to an extension of the effective conjugation length present in conjugated polymer systems [34, 119, 124].

Longer effective conjugation length should in turn lead to increased carrier mobility, and thus we expect negative correlation between the lowest absorption energies and the hole mobility.

UV-Visible absorbance spectra recorded for MEH-PPV samples (Figure 5.5a) generally agree with our observations for mobility in MEH-PPV samples. With the exception of MEH-PPV/CB spectra, the energetic onset is inversely correlated with carrier mobility. However, the resulting onsets all lie in the same general area (again excluding chlorobenzene data), making the data inconclusive for the purposes of solvent dependency. Spectra obtained for P3HT samples (Figure 5.5b) also suggest that there is little or no relationship between the effective conjugation and solvents used in this study.

### **Solubility Analysis**

The solvent dependence of mobility in nanotube-based devices is expected to stem from solvent quality – how well the solvent is at straightening the polymer chain [120, 123, 124]. In general, molecules tend to collapse into a coiled structure in poor solvents, which acts to localize free carriers [120] and prevent long range molecular ordering [124]. Neither of these effects is desirable, as both inhibit carrier transport through the material. Thus, it seems evident that solvents such as tetrahydrofuran and chloroform must act to straighten the MEH-PPV molecule, while the molecule coils in solvents like toluene. In fact, molecular simulations have shown this to be precisely the case. Recent work by Lee et. al. has shown that the MEH-PPV molecule adopts a coiled structure in toluene, while straightening in chloroform [123]. Similar work by Derosa for P3HT suggests that excessive energy is required to coil the P3HT molecule [125], and thus it is energetically favorable for the molecule to remain straight, regardless of solvent.

This property is likely responsible for the high degree of molecular ordering observed in this material.

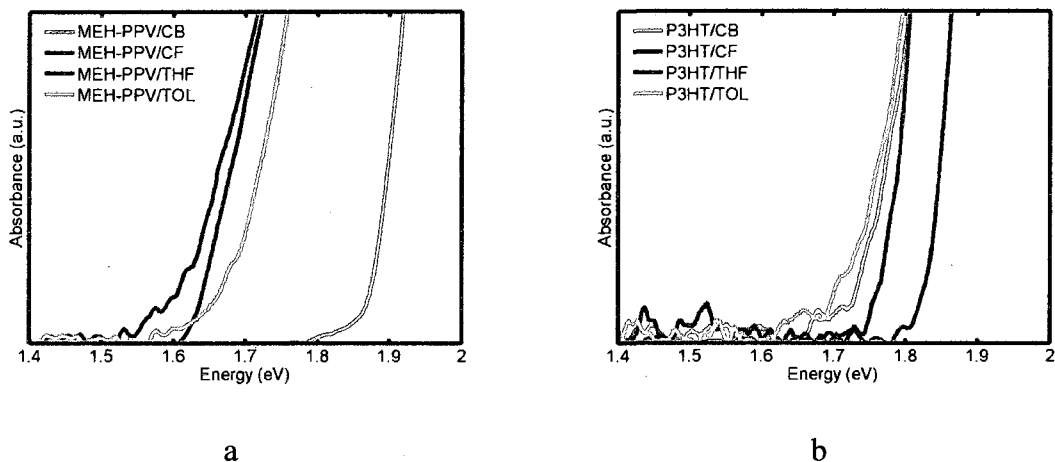


Figure 5.5. Energetic onsets of absorbance spectra for a) MEH-PPV and b) P3HT nanotubes created by template wetting from various solvents.

Analysis of calculated solubility parameters in conjunction with experimental work provides some insight into the origin of the observed enhancements in MEH-PPV mobility when dissolved in different solvents. Following group contribution methods (see Appendix) for calculating solubility and solvent interaction parameters [114], based on the Flory-Huggins theory of polymer solutions [126], provides insight into the possible conformation of conjugated polymers in various solvents. Solubility parameters provide information about the cohesive energy between components and changes in enthalpies during mixing, and are generally useful for determining appropriate solvents for various materials [127].

Solubility parameters, also known as Hildebrand parameters, are calculated following

$$\delta_t = \sqrt{\frac{U}{V}}, \quad (5.7)$$

where  $U$  is the molar cohesive energy, and  $V$  is the molar volume of the species for which the total solubility parameter,  $\delta_t$ , is being calculated [126]. Further, the total solubility parameter of a material is often described in terms of three key components contributing to solubility. The dispersion, polar, and hydrogen bonding components,  $\delta_d$ ,  $\delta_p$ , and  $\delta_h$  are related to the total solubility parameter following [126]

$$\delta_t^2 = \delta_d^2 + \delta_p^2 + \delta_h^2, \quad (5.8)$$

and fractional parameters, Fr, given by

$$Fr_d = 100 \times \frac{\delta_d^2}{\delta_t^2} \quad (5.9)$$

$$Fr_p = 100 \times \frac{\delta_p^2}{\delta_t^2} \quad (5.10)$$

$$Fr_h = 100 \times \frac{\delta_h^2}{\delta_t^2} \quad (5.11)$$

represent the percentage contribution of each component to the total parameter [128].

The total solubility parameters are calculated by summing all group contributions to molar cohesive energy and molar volume to determine  $U$  and  $V$  in (5.7) [126]. The component contributions are calculated by summing component group molar attraction constants,  $F$ , defined by

$$F_i = \sqrt{U_i V_i} \quad (5.12)$$

for the  $i$ th component ( $d$ ,  $p$ , or  $h$ ) using

$$\delta_d = \frac{\sum z F_d}{\sum z V}, \quad (5.13)$$

$$\delta_p = \frac{\sqrt{\sum z F_p^2}}{\sum z V}, \quad (5.14)$$

and

$$\delta_h = \sqrt{\delta_t^2 - \delta_d^2 - \delta_p^2} \quad (5.15)$$

to determine the values for each component [128].

Calculations using this approach allow for some estimation of the effect of the polymer's molecular weight on the solubility when the molecular termination group is included. Table 5.2 provides reported solubility parameters for solvents used in this study, along with calculated values for methyl-terminated MEH-PPV and P3HT molecules with molecular weights of 100,000 g/mol. Following [128], a ternary plot is provided in Figure 5.6 illustrating the relationship between the fractional solubility components of the polymers (again with  $M_w = 100,000$  g/mol) and the solvents used here. The relative proximity of points for each polymer and solvent in the ternary plot is indicative of solvent quality; the closer the polymer point is to a given solvent, the better the solvent is expected to be for that polymer.

Solvent interaction parameters,  $\chi$ , are commonly calculated following

$$\chi = \chi_S + \chi_H, \quad (5.16)$$

where  $\chi_S$  and  $\chi_H$  represent entropy and enthalpy terms, respectively [126]. In general, lower values of  $\chi$  suggest that the solute is more soluble in the given solvent [127], and thus the polymer chains are expected to be straighter. The entropic term is seldom calculated or measured in practice, instead relying on empirical corrections to the total term when the enthalpy term is calculated [127]. The enthalpy term is most commonly calculated following

$$\chi_{H,1} = \frac{v_i}{RT} (\delta_{t,i} - \delta_{t,j})^2, \quad (5.17)$$

where the subscripts  $i$  and  $j$  denote the values corresponding to the solvent and solute, respectively [126]. An alternative expression may be written by replacing the squared difference term in the right hand side of (5.17) with a sum of the squared differences between each component of the parameter, rather than the total parameter. The resulting equation

$$\chi_{H,2} = \frac{v_i}{RT} \left\{ (\delta_{d,i} - \delta_{d,j})^2 + (\delta_{p,i} - \delta_{p,j})^2 + (\delta_{h,i} - \delta_{h,j})^2 \right\} \quad (5.18)$$

is also examined below.

Table 5.2. Solubility parameters for MEH-PPV, P3HT, and common solvents.

<b>Material</b>	$\nu$ ( $\text{cm}^3/\text{mol}$ )	$\delta_d$ ( $\text{MPa}^{1/2}$ )	$\delta_p$ ( $\text{MPa}^{1/2}$ )	$\delta_h$ ( $\text{MPa}^{1/2}$ )	$\delta_t$ ( $\text{MPa}^{1/2}$ )
Chlorobenzene	102.1	19	4.3	2	19.6
Chloroform	80.7	17.8	3.1	5.7	19
Tetrahydrofuran	81.7	16.8	5.7	8	19.4
Toluene	106.8	18	1.4	2	18.2
MEH-PPV	89529	18.2	3.6	6.4	19.63
P3HT	80962	19.1	4.3	10.1	22.01

Solvent data collected from tables of published values in [114]. Polymer values are calculated using (5.8) and (5.13)-(5.15).

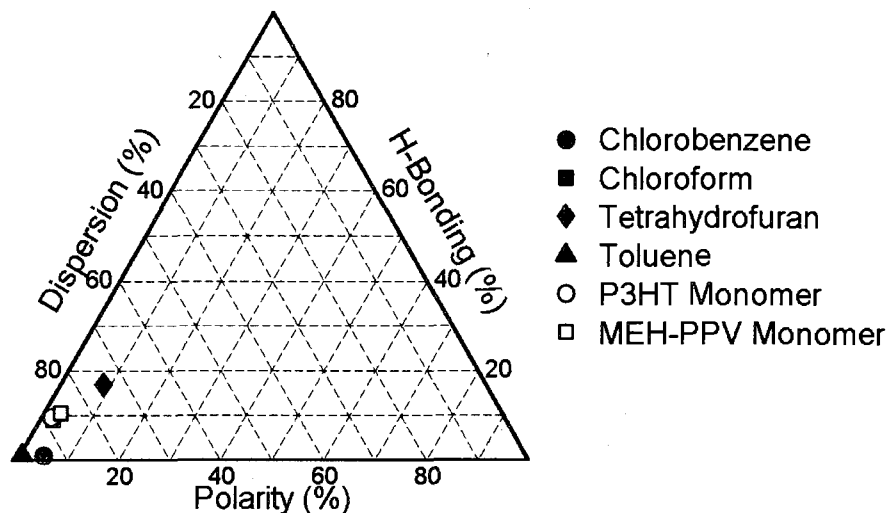


Figure 5.6. Ternary representation of the relationship between fractional solubility parameters for MEH-PPV, P3HT, and solvents used here.

Solvent interaction parameters were calculated using (5.17) and (5.18) for both MEH-PPV and P3HT molecules of varying molecular weight, assuming the polymer chains are terminated with a methyl end group. Molecular weight dependent calculations of the solubility parameters for the two polymers were calculated first, and then substituted into the solvent interaction equations. Resulting data for each polymer is presented in Figure 5.7. Solvent interaction parameter profiles change very little with solvent or molecular weight, supporting observations from molecular modeling [125]. However, results for MEH-PPV vary widely for both  $\chi_{H,1}$  and  $\chi_{H,2}$ , suggesting the material is more sensitive to solvent choice, as predicted by electrical characterization.

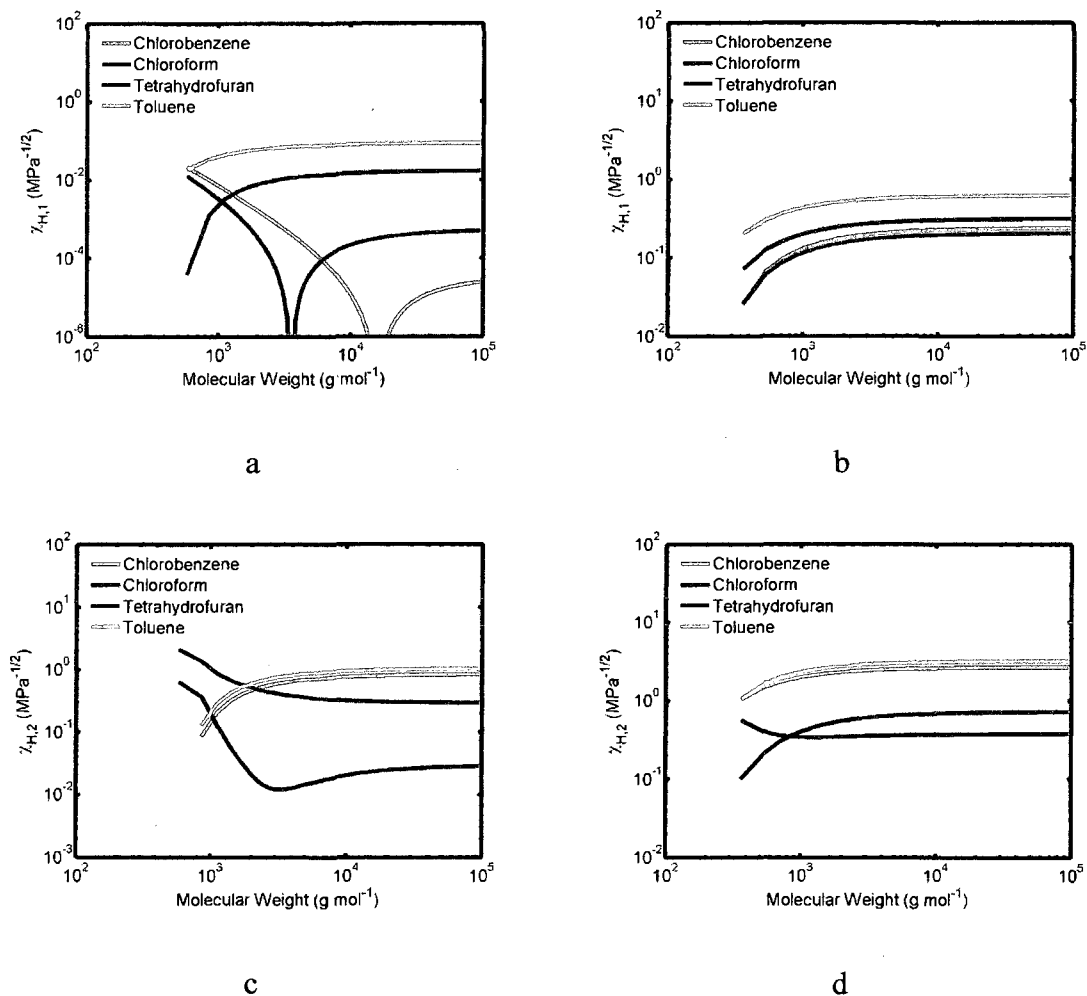


Figure 5.7. Molecular weight dependence of the solvent interaction parameters  $\chi_{H,1}$  and  $\chi_{H,2}$  for methyl-terminated MEH-PPV (a,c) and P3HT (c,d).

For both polymers, the two calculations produce differing predictions of solvent quality. For example,  $\chi_{H,1}$  calculations suggest that the best solvents for MEH-PPV are tetrahydrofuran at low molecular weights and chlorobenzene at higher molecular weights, while  $\chi_{H,2}$  calculations predict chloroform to be the best solvent for all but the very lowest molecular weights. The differences are less exaggerated for P3HT, as tetrahydrofuran is generally predicted to be the best solvent, while toluene is consistently the worst. Such

discrepancies are not uncommon between solvation models, and similar observations for MEH-PPV have been reported elsewhere [123].

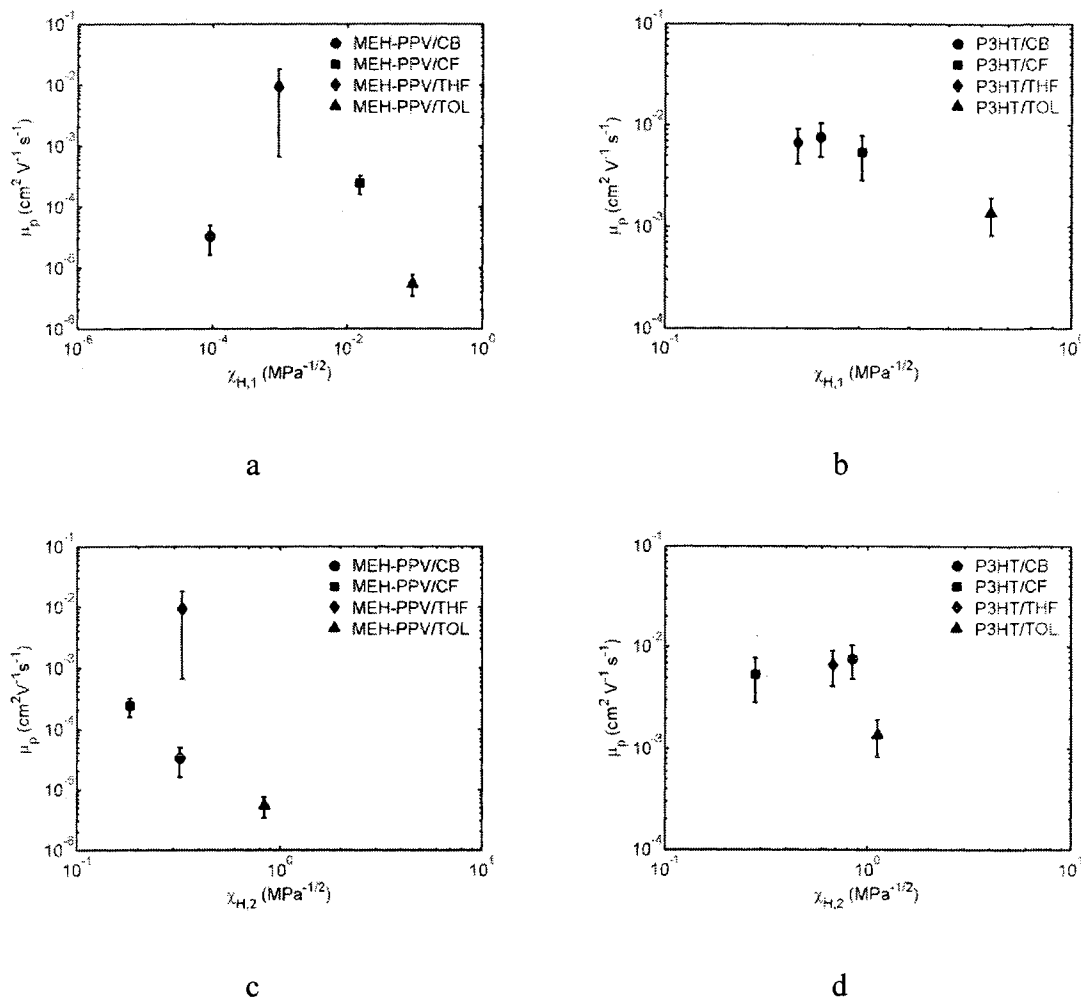


Figure 5.8. Measured hole mobilities in 100 nm nanotube-based electronic devices plotted against solvent interaction parameters calculated using (5.17) and (5.18). Mobilities for MEH-PPV and P3HT plotted versus  $\chi_{H,1}$  (a,b) and  $\chi_{H,2}$  (c,d).

In order to define the link between solvent selection and molecular ordering, hole mobilities calculated using (5.3) are plotted against the two solvent interaction parameters obtained for each polymer, assuming  $M_w = 100,000$  g/mol, in order to discern any correlations. These plots are given in Figure 5.8 for each polymer and each method of

calculating the solvent interaction parameter. In general, mobility is reasonably correlated with both  $\chi$  values for MEH-PPV, but the more common  $\chi_{H,1}$  calculation seems to provide the best correlation for each polymer.

### **Conclusions**

Solution-based template-wetting procedures have been demonstrated as an effective means of producing nanotubular structures from two of the most commonly studied semiconducting polymers, MEH-PPV and P3HT. Solvent selection has been shown to have significant effects on conduction processes, and possibly molecular order, within conjugated polymer systems. MEH-PPV, a generally amorphous material was shown to behave considerably different depending on choice of solvent. This is in agreement with other observations [119, 123, 124], and has been demonstrated here as an effective means of altering device performance. The semi-crystalline polymer, P3HT, showed little or no difference in properties due to either solvent selection or incorporation into nanoporous membranes.

Throughout experimental work, the MEH-PPV/CB sample group provided unreliable results. UV-visible spectra indicate that the MEH-PPV/CB sample group is behaving, at least optically, more like thin films of the material. Further, very thick layers residual polymer were apparent on these samples during processing, suggesting that the polymer solution may be failing to effectively infiltrate the template. However, complete wetting with chlorobenzene was observed for P3HT samples, and thus rules out wetting issues with the solvent. The assertion that little polymer enters the pore in the MEH-PPV/CB sample group is also in agreement with predictions for  $\chi_{H,1}$ , given that MEH-PPV is noted to form highly ordered aggregates when dissolved in very good solvents

[119, 124]. It is likely that these aggregates fail to enter the pores of the template during the wetting procedure, thereby leading to drastic overestimation of device area and underestimation of the true hole mobility. Further, these aggregates likely consist mostly of long chains consisting of fewer molecular defects, which would disrupt molecular ordering [124]. Therefore, it is expected that only a limited amount of polymer enters the pore in the MEH-PPV/CB sample group, and the polymer that does enter is likely of low quality.

Little difference was observed for hole mobility across the various P3HT samples, suggesting improvement in ordering originating from confinement within the nanopore is limited or non-existent for this polymer. The mobilities measured in P3HT samples were also in excellent agreement with those reportedly observed elsewhere in thin-film transistors of the same material [6, 9, 16]. However, significant improvements were observed for MEH-PPV samples. Hole mobilities obtained from MEH-PPV/THF samples were on the order of those observed in P3HT samples, and four orders of magnitude higher than mobilities typically reported in thin films of MEH-PPV [40, 116]. The lowest observed mobilities for MEH-PPV samples were observed in samples created from toluene solutions, and were on the order of previously reported values for films.

In both polymers, the highest attainable mobilities for the material when incorporated into nanoporous membranes seem to be  $\sim 10^{-2} \text{ cm}^2 \text{ V}^{-1} \text{ s}^{-1}$ . This allows one to speculate about the molecular ordering and morphology within the nanopore. Mobilities of  $\sim 10^{-2} \text{ cm}^2 \text{ V}^{-1} \text{ s}^{-1}$  are observed for highly ordered P3HT thin films when conduction is perpendicular to the length axis of the molecules in the device, and is attributed to close interactions between the polymer backbones and planar packing of the ring structures in

the chain [9]. This suggests that molecules order themselves perpendicular to the nanopore wall (as described elsewhere by Steinhart [99]), and thus perpendicular to the direction of current flow. Theoretically determined upper bounds to mobility are on the order of  $10 \text{ cm}^2 \text{ V}^{-1} \text{ s}^{-1}$  for MEH-PPV, when conduction is assumed to be dominated by intrachain processes. This mobility is far in excess of those observed in the samples examined in this work, and further support the hypothesis that the molecules must align themselves perpendicular to the nanopore wall.

## CHAPTER 6

# SOXHLET EXTRACTION OF POLYTHIOPHENE FOR IMPROVED POLYMER PURITY FOR NANOTUBE FABRICATION

### Introduction

Since the introduction of polythiophene-based electronic devices in 1986 [4], advances in synthesis procedures [129-132] have led to dramatic improvements in molecular ordering and device performance for polythiophene systems [6, 9, 39]. While various semiconducting thiophene derivatives have demonstrated higher mobilities, poly(3-hexylthiophene) (P3HT) has proven to be the most widely studied thiophene material. This is largely because of its solubility in common organic solvents and its exceptionally high carrier mobility among soluble materials [9, 39]. The high mobilities observed originate from the fact that the material forms well ordered films in which high degrees of intermolecular  $\pi$ -orbital overlapping is present [9, 39].

Synthesis of high quality materials is of the utmost importance [132], as impurities present in the material can have significant, adverse effects on device performance. Impurities in organic electronic materials can act to limit molecular ordering, trap free carriers, cause unintentional doping effects, and accelerate device degradation [18]. Key issues with synthetic processes are the wide variety of molecular weights generally present in resultant material and high content of metallic complexes

originating from residual catalyst [8]. The Rieke process [131, 132] for synthesis is one of the most commonly utilized methods for the production of P3HT, though others have been used as well (see for example, McCullough [130] and Yamato [129]), and is the process used to synthesize P3HT material distributed by Sigma-Aldrich. All commonly published synthetic procedures react halogenated 3-hexylthiophene monomers such as those illustrated in Figure 6.1 to produce P3HT. Further, the catalytic materials used in the reaction are often metallic complexes, including activated Zn [131, 132]. This leads to the presence of undesirable metallic and ionic impurities within the synthesized polymer.

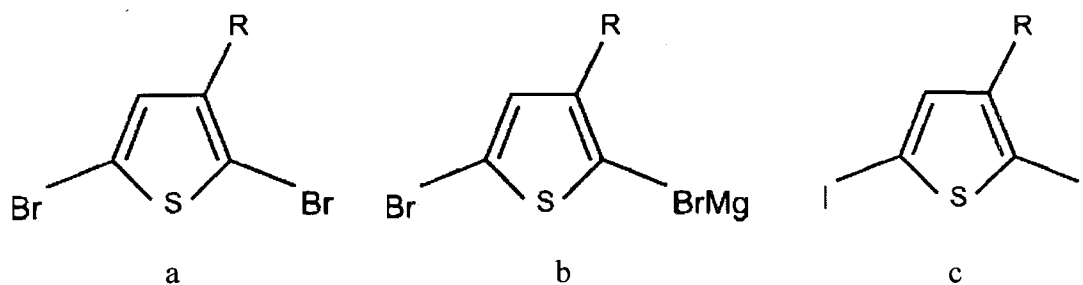


Figure 6.1. Examples of the halogenated monomers commonly reacted to produce poly(3-alkylthiophene)s including P3HT. These include a) 3-alkyl-2,5-dibromothiophene [131], b) 2-bromo-5-(bromomagnesio)-3-alkyl-thiophene [130], and c) 3-alkyl-2,5-diiodothiophene [129]. The side chain, R, is  $(\text{CH}_2)_5\text{CH}_3$  for P3HT.

Purification processes based on various extraction techniques have been developed and utilized to produce P3HT material with very low metallic content and narrow molecular weight distributions [8, 16, 121, 133]. Trznadel et al. demonstrated Soxhlet extraction as an effective means of purifying bulk P3HT after synthesis [8]. Several narrow molecular weight fractions were collected when following an extraction sequence of acetone, hexane, dichloromethane, tetrahydrofuran, and finally chloroform [8]. The acetone and chloroform fractions were noted to contain large amounts of metallic impurities and small oligomers [8]. Utilizing this Soxhlet extraction procedure,

Samitsu demonstrated that P3HT synthesized by the Rieke process (as obtained from Sigma-Aldrich) could be separated into 2 major fractions: one extracted from the bulk with dichloromethane with an average molecular weight of approximately 15,000 g/mol, and another extracted with tetrahydrofuran whose average molecular weight was approximately 110,000 g/mol [133]. The dichloromethane fraction accounted for ~12% of the mass of the original bulk polymer, and the tetrahydrofuran fraction accounted for ~84% [133]. The remaining four percent included both the acetone and hexane fractions, but the metallic content of these fractions was not commented upon [133].

The effect of Soxhlet extraction procedures on the production and properties of P3HT-based semiconducting polymer nanotubes is examined here. The extraction process is examined in terms of the Flory-Huggins theory described in Chapter 5, and the electronic properties of various fractions are examined and compared with the bulk material before purification.

## **Experimental**

### **Materials**

Regioregular poly(3-hexylthiophene-2,5-diyl), or P3HT, was obtained from both Sigma-Aldrich (with > 98.5 % head-to-tail linkages, denoted as SA-P3HT from here on) and American Dye Source (ADS306PT, denoted here as ADS-P3HT). High purity acetone, chloroform, dichloromethane, hexane, tetrahydrofuran, and toluene were all obtained from Sigma-Aldrich, and were used as received. Purification procedures were performed using a ChemGlass micro Soxhlet extractor (25 ml capacity) with a ThermoWell heating mantle. Commercially available anodic porous aluminum oxide membranes (Whatman Co.) were used as templates. Templates were 60  $\mu\text{m}$  thick with

monodisperse pore diameters of 100 nm and 200 nm, with porosities of  $10^{10}$  pores per  $\text{cm}^2$  and  $10^9$  pores per  $\text{cm}^2$ , respectively.

## Methods

Soxhlet extraction procedures (see [134, 135] for detailed applications of Soxhlet extraction for polymer fractionation) were performed following a variation of the process described by Trznadel [8]. The procedure described by Trznadel, and later used by Merlo [121] and Samitsu [133], called for extraction in each of five solvents (acetone, hexane, dichloromethane, tetrahydrofuran, and chloroform) in order, until the filtrate appeared colorless. Trznadel, who was working with P3HT synthesized in his own lab, noted that chloroform dissolved all components of the bulk and could be used to remove virtually all residual polymer in the thimble after completing the other extractions [8]. Both Merlo [121] and Samitsu [133], who performed their work with Sigma-Aldrich polymer synthesized using the Rieke process, pointed out that no polymer remained in the thimble after extraction with tetrahydrofuran, and that the final extraction with chloroform was unnecessary.

Initial testing was performed with ADS306PT following the Trznadel process exactly, but it was observed that material could still be extracted with acetone after completion of one extraction with each of acetone and hexane. It was then determined that the first two solvents be repeated. Further, the extractor was cleaned by removing the thimble and sample after each extraction, and refluxing with clean chloroform for 30 minutes. Each extraction cycle took ~12 hours, with the exception of the dichloromethane cycle, which took ~24 hours. Filtration was performed using this extraction process twice, first using a 30 mg sample of ADS306PT, then with 30 mg of SAP3HT. The

extracting solvent was allowed to evaporate from the collected samples, and the mass of each fraction was recorded.

The Flory-Huggins solubility methods described in Chapter 5 were also used to examine the extraction process. Solubility parameters for P3HT were calculated as a function of molecular weight for three possible end group combinations, and solvent interaction parameters were calculated for each of the extraction solvents. This is done to provide insight into the possible contents of each fraction.

Electronic devices are created using template wetting techniques. Wetting solutions were created using the unfiltered polymer (UNF), dichloromethane fraction (DC), and tetrahydrofuran fraction (THF) by dissolving in chloroform at a concentration of 2 mg/ml. Templates with both 100 nm and 200 nm nominal pore diameters were wetted with 100  $\mu$ l droplets, and solvent was allowed to evaporate for several hours. Residual polymer was removed from template surfaces by means of non-reactive ion etching with a 100 W He plasma, at 200 mtorr for 10 minutes on each side. Electronic contacts were created by depositing 150 nm Au layers through a shadow mask via electron beam evaporation, creating device structures as illustrated in Figure 4.3a.

## Results and Discussion

### Soxhlet Extraction

Extraction procedures are often developed and analyzed by examining the relationships between the dispersion, polarity, hydrogen bonding solubility,  $\delta$ , and fractional, Fr, parameters [128]. Here, we use these procedures, along with the two methods of calculating solvent interaction, also described in Chapter 5, to access the effects of molecular weight and molecular termination groups on solubility in the solvents used in the extraction procedure. Combinations of methyl and Br termination groups for the P3HT molecules are examined here. Due to lack of complete empirical data for group contributions to cohesive energies and molar attraction constants, the effects of iodine and MgBr terminations are not examined. Solubility parameters for solvents used in the extraction process used in this work are provided in Table 6.1, and are represented visually with a ternary plot following [128] shown in Figure 6.2 for methyl-terminated P3HT, denoted Me-(3HT)<sub>n</sub>-Me, at various molecular weights. Similar ternary plots for molecules terminated with Br at both ends, Br-(3HT)<sub>n</sub>-Br, and a combination of methyl and Br terminations, Br-(3HT)<sub>n</sub>-Me, are presented in Figure 6.3.

Table 6.1. Solubility parameters for P3HT and solvents used in the Soxhlet extraction process.

Material	$\nu$ (cm <sup>3</sup> /mol)	$\delta_d$ (MPa <sup>1/2</sup> )	$\delta_p$ (MPa <sup>1/2</sup> )	$\delta_h$ (MPa <sup>1/2</sup> )	$\delta_t$ (MPa <sup>1/2</sup> )
Acetone	74	15.5	10.4	7	19.9
Dichloromethane	102.1	18.2	6.3	6.1	20.2
Hexane	63.9	14.9	0	0	14.9
Tetrahydrofuran	131.6	16.8	5.7	8	19.5

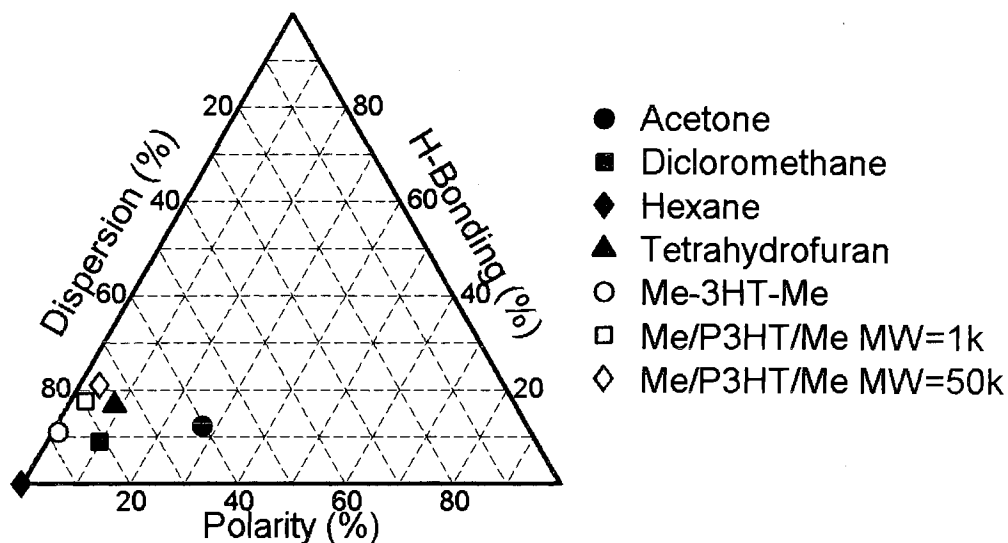


Figure 6.2. Ternary plot illustrating relative locations of extraction solvents and various molecular weights of Me-(3HT)<sub>n</sub>-Me as determined from solubility parameters.

The relative location of points for solutes (in this case, the polymers and monomers) to those of the extraction solvents is generally indicative of the solute's solubility in a given solvent. The closer the solute point is located to the solvent, the more soluble that material is expected to be in that solvent. For all termination groups examined, the ternary plotting method suggests that lower molecular weight materials are likely more soluble in dichloromethane, and that they progressively become more soluble in tetrahydrofuran as molecular weight is increased. Note, however, that the variation in solubility changes least dramatically for Br-(3HT)<sub>n</sub>-Me, and that the monomers are not always predicted to be more soluble than the polymers, as one might expect.

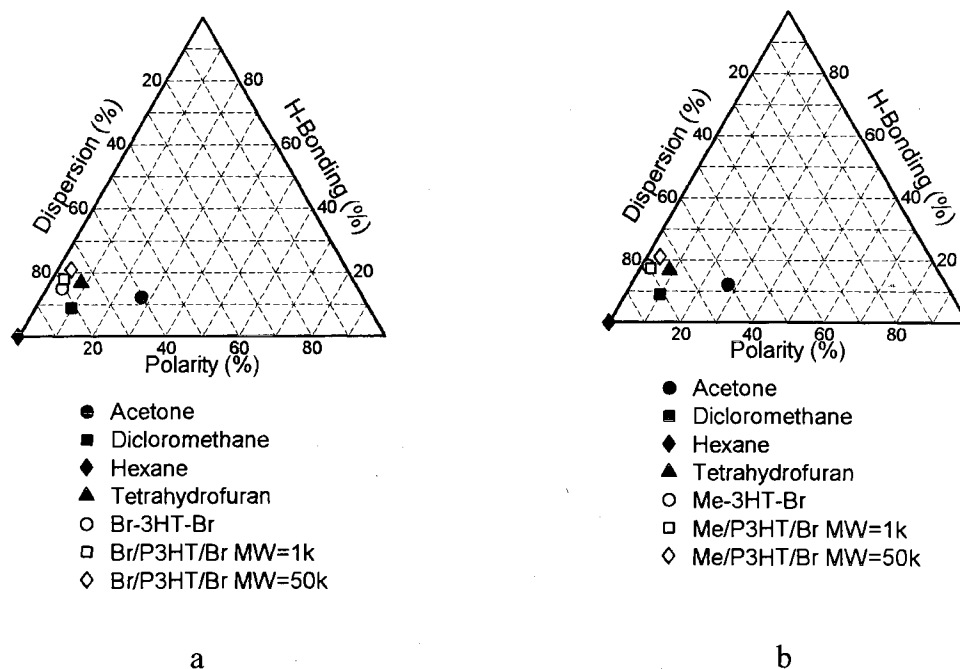


Figure 6.3. Ternary plots illustrating relative locations of extraction solvents and various molecular weights of a) Br-(3HT)<sub>n</sub>-Br and b) Br-(3HT)<sub>n</sub>-Me as determined from solubility parameters.

The various methods of calculating the solvent interaction parameter following

$$\chi_{H,1} = \frac{v_i}{RT} (\delta_{t,i} - \delta_{t,j})^2 \quad (6.1)$$

and

$$\chi_{H,2} = \frac{v_i}{RT} \left\{ (\delta_{d,i} - \delta_{d,j})^2 + (\delta_{p,i} - \delta_{p,j})^2 + (\delta_{h,i} - \delta_{h,j})^2 \right\} \quad (6.2)$$

produce significantly different results for the molecular weight dependence of solubility at room temperature. Little affect was actually observed due to changes in end group, thus only the Me-(3HT)<sub>n</sub>-Me data is examined here. Figure 6.4 illustrates the molecular weight dependence of Me-(3HT)<sub>n</sub>-Me. Solvation predictions obtained using (6.1) are in stark contrast to empirical observations. From the  $\chi_{H,1}$  calculation, we expect that P3HT is most soluble in dichloromethane, regardless of molecular weight, and that the material is more soluble in acetone than in tetrahydrofuran. Neither of these predictions are true, as

predictions are true, as the material is indeed soluble in tetrahydrofuran, and virtually insoluble in acetone. However, the predictions obtained from  $\chi_{H,2}$  calculations are in much better agreement with experiment. Solubility is predicted to be best in dichloromethane at low molecular weights, and better in tetrahydrofuran for higher molecular weights. This is in good agreement with extraction procedures performed here, and observations made elsewhere as well [8, 133].

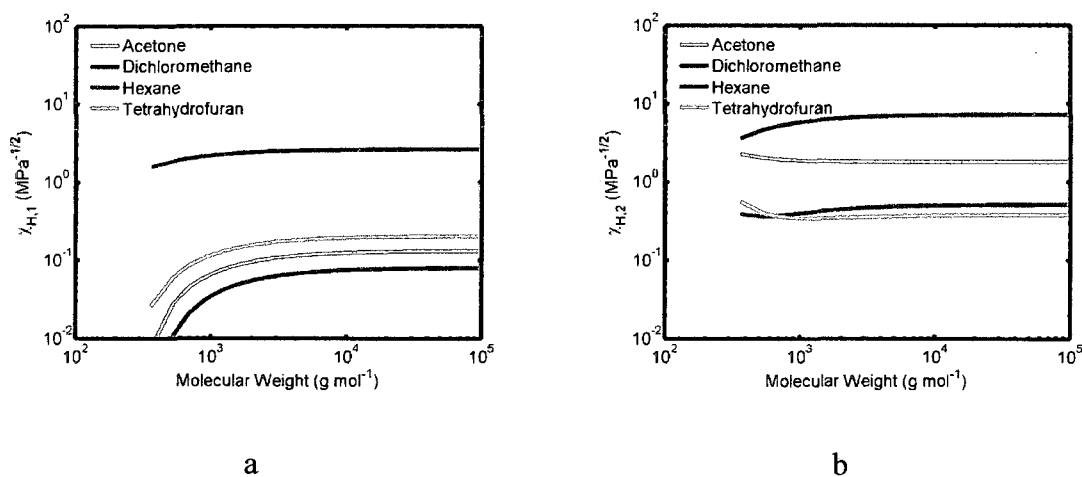


Figure 6.4. Molecular weight dependence of the solvent interaction parameters, a)  $\chi_{H,1}$  and b)  $\chi_{H,2}$ , for Me-(3HT)<sub>n</sub>-Me.

Weight percentages of material extracted for each fraction are recorded in Table 6.2 for experimental results obtained here, and in comparison with those reported in the literature. Our experimental results are in good agreement with those of Samitsu [133] for SA-P3HT, but significantly higher levels of material were extracted in the AC and HE fractions for ADS-P3HT. Due to the limited solubility predicted for P3HT in these solvents, the extracted material for these fractions is assumed to be made up of compounds other than P3HT. These contaminants are likely residual catalyst material and defective oligomers, as observed by Trznadel [8].

Table 6.2. Percentage of material extracted in each cycle of the Soxhlet extraction procedure for experimental work done here and elsewhere.

	Present Work		Samitsu[133]	Trznadel[8]
	ADS-P3HT (%)	SA-P3HT (%)	SA-P3HT (%)	Lab Made (%)
Acetone	9.7	0.6	2.6	6.5
Hexane	4.7	4.0	1.7	9.7
Dichloromethane	24.5	16.5	12.2	33.1
Tetrahydrofuran	55.0	71.3	83.6	49.2
Chloroform	-	-	-	1.6
Lost Material	6.0	7.6	-	-

### Electrical Characterization

Current densities measured in Au/P3HT/Au hole-only, electronic devices yielded consistent results from device to device, and substrate to substrate. Space-charge-limited currents were found to be in good agreement with the models applied in Chapter 5, and  $J$ - $V$  characteristics for all twelve sample groups are provided in Figure 6.5. Electronic devices created from the DC fraction exhibited consistently higher current densities than those observed in either the THF fraction or the unfiltered material, regardless of pore size or vendor. Devices created from the THF fraction also demonstrated higher current densities when compared with the unfiltered material. Hole mobilities were calculated following the procedures presented in Chapter 5 following (5.2) and (5.3). Experimentally obtained data were found to agree most closely with the behavior described by (5.3), which describes a transitional behavior from ohmic processes at low applied bias to space-charge-limited behavior at higher bias [57]. Resulting mobility data are presented in Table 6.3 and illustrated in Figure 6.6. No case presented any clear

evidence that pore size affected mobilities. In all sample groups, mobilities calculated for the DC fraction were highest, but in general, hole mobility remained on the order of  $\sim 10^{-2} \text{ cm}^2 \text{ V}^{-1} \text{ s}^{-1}$ .

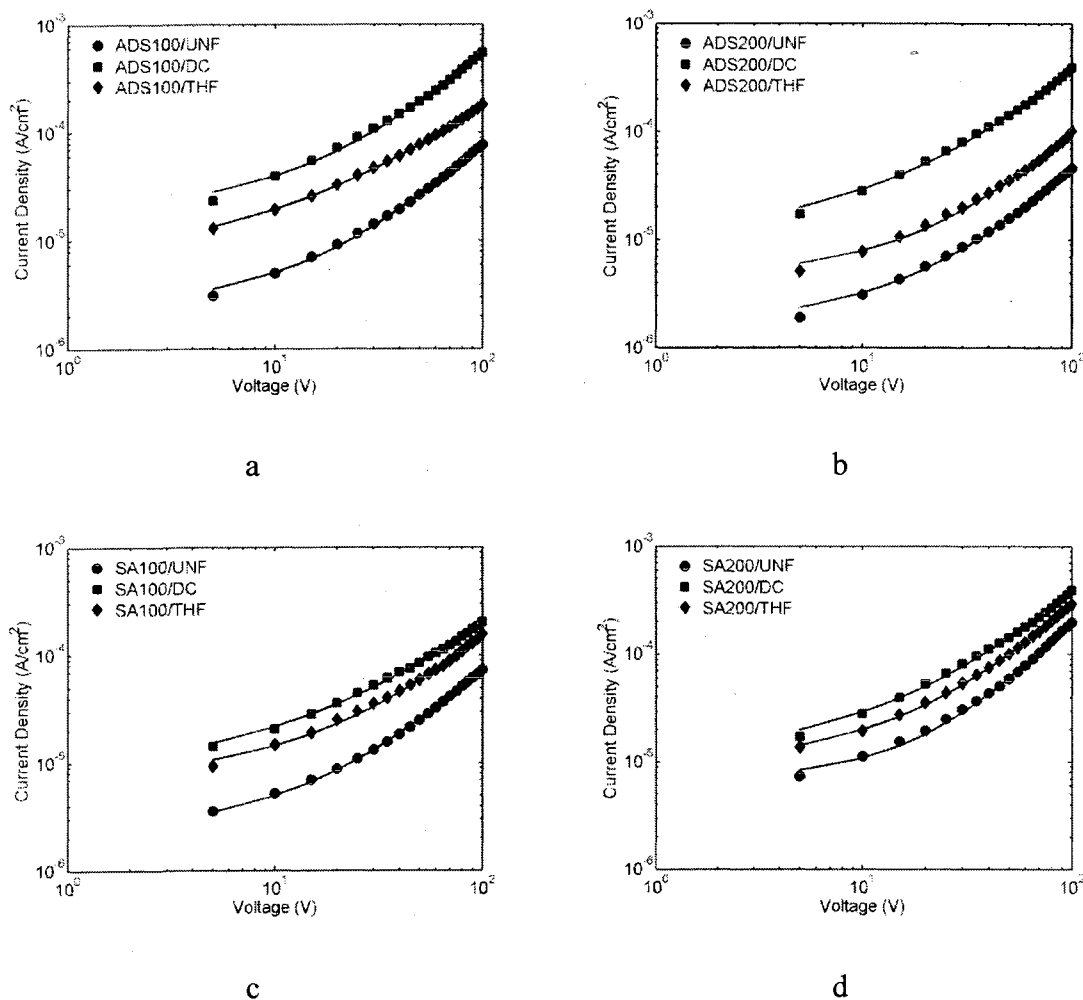


Figure 6.5.  $J$ - $V$  characteristics for nanotube-based electronic devices created with various fractions of P3HT material. Characteristics for devices created using ADS polymer are given for a) 100 nm and b) 200 nm nanotubes. Like characteristics for devices fabricated from polymer obtained from Sigma-Aldrich are provided for c) 100 nm and d) 200 nm nanotubes. Solid lines represent regression fits to (5.3).

Table 6.3. Hole mobility data for various fractions of P3HT.

Fraction	Following (5.2)		Following (5.3)	
	$\mu_{p,avg}$ ( $\text{cm}^2 \text{V}^{-1} \text{s}^{-1}$ )	$\sigma_{\mu,avg}$ ( $\text{cm}^2 \text{V}^{-1} \text{s}^{-1}$ )	$\mu_{p,avg}$ ( $\text{cm}^2 \text{V}^{-1} \text{s}^{-1}$ )	$\sigma_{\mu,avg}$ ( $\text{cm}^2 \text{V}^{-1} \text{s}^{-1}$ )
SA100/UNF	8.07E-03	3.70E-03	5.75E-03	8.35E-04
SA200/UNF	1.25E-02	3.21E-03	9.07E-03	4.95E-03
SA100/DC	9.40E-03	2.77E-03	9.32E-03	2.38E-03
SA200/DC	3.21E-02	6.13E-03	1.94E-02	1.08E-02
SA100/THF	1.04E-02	1.19E-03	5.49E-03	1.03E-03
SA200/THF	1.22E-02	4.41E-03	6.77E-03	3.34E-03
ADS100/UNF	1.05E-02	3.79E-03	4.70E-03	3.37E-03
ADS200/UNF	5.26E-03	4.41E-03	2.85E-03	2.34E-03
ADS100/DC	3.05E-02	6.13E-03	1.09E-02	7.12E-03
ADS200/UNF	3.21E-02	6.13E-03	1.60E-02	9.26E-03
ADS100/THF	1.53E-02	6.75E-03	6.79E-03	5.82E-03
ADS200/THF	1.40E-02	8.61E-03	3.85E-03	1.43E-03

The mobility enhancement for the DC fraction was strongest in ADS-P3HT, but larger standard deviations of the mobility were also observed for this material, indicative of lower purity in the bulk material. The DC fraction is known to consist of moderate molecular weight material [133], and likely contains the most narrow molecular weight distribution of all fractions [8]. Reduced molecular weight variation should lead to improved ordering of the material, as interstitial defects created by mixing of dissimilar molecular lengths disrupts long range order [18], thus the devices fabricated with the DC fraction should be most ordered. Mobilities calculated for the THF fractions are virtually identical to those of the unfiltered material. This supports the hypothesis that the DC fraction should be more ordered due to narrower molecular weight distributions, because

the THF fraction has been observed to contain a very broad range of molecular weights [8]. Further, the THF fraction likely contains any metallic impurities not removed in the AC or HE extractions.

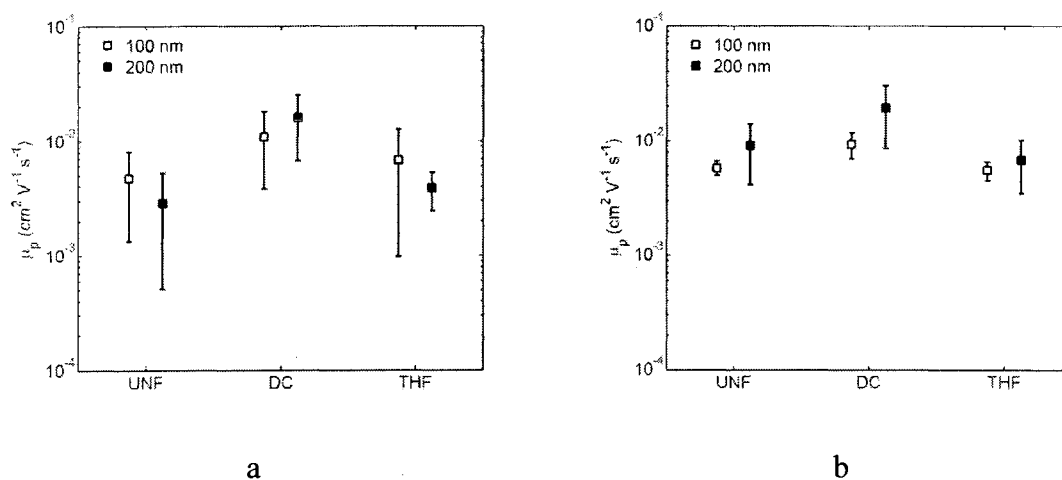


Figure 6.6. Hole mobilities for 100 nm and 200 nm nanotube-based electronic devices from various fractions of a) ADS-P3HT and b) SA-P3HT.

### Conclusion

Soxhlet extraction has been demonstrated as an effective means of purifying bulk P3HT material. The extraction process has been accurately predicted following a variation of Flory-Huggins theory for polymer solutions. Extracted P3HT was used to successfully create semiconducting polymer nanotubes, and electronic devices based on these nanotubes. Significant differences in carrier transport properties due to pore diameter of manufacturer were not observed, but material obtained from ADS was judged to have significantly higher levels of impurity than material obtained from Sigma-Aldrich. Slight improvements in hole mobility were observed for the dichloromethane

fraction in all sample groups, and is likely due to the high degree of purity in this fraction.

The prediction scheme for Soxhlet extraction processes following [128] adequately described the extraction process used in this work, when analyzed in conjunction with molecular weight dependent solvent interaction parameters calculated following (6.2). Predictions made using the standard solvent interaction expression (6.1), proved inaccurate, suggesting that (6.2) may be a more accurate approach to calculation of solubility for the purposes of developing extraction procedures. The extraction procedure produced significant quantities of material for each of the DC and THF fractions, with extracted mass percentages in good agreement with other work for SA-P3HT [133]. Higher levels of material were extracted from ADS-P3HT bulk material during the AC, HE, and DC extraction cycles, suggesting both higher impurity content, and lower average molecular weight of the bulk material.

Mobilities observed in the various forms of regioregular P3HT were consistently  $10^{-2} \text{ cm}^2 \text{ V}^{-1} \text{ s}^{-1} \sim 10^{-3} \text{ cm}^2 \text{ V}^{-1} \text{ s}^{-1}$ , which is in good agreement with values published elsewhere as observed in field effect transistors [6, 9, 39]. Significant improvement in mobility due to confinement of P3HT within the nanoporous material was not observed, reinforcing similar conclusions for P3HT from Chapter 5. Mobility was observed to be slightly improved in the DC fraction, and these results are attributed to the potentially higher degree of purity and narrower molecular weight distribution of this material. The lack of a broad range of molecular weights likely reduces any interstitial ordering defects that may occur due to dissimilar molecules.

## CHAPTER 7

### CONCLUSION

In this work, template wetting has been shown as an effective means of producing nanotubular structures from two of the most commonly studied semiconducting polymers, poly[2-methoxy-5-(2-ethylhexyloxy)-1,4-phenylenevinylene] (MEH-PPV) and poly(3-hexylthiophene) (P3HT). Nanotubes were created by wetting nanoporous aluminum oxide with solutions of these polymers, and were used in electronic devices, including “hole-only” diodes and a solar cell. The nanostructure was generally shown to enhance carrier mobility in the amorphous polymer, MEH-PPV, while mobilities were little changed in the semi-crystalline P3HT.

These semiconducting nanotubes were electronically characterized by investigation of current-voltage characteristics. In general, current-voltage characteristics were found to be best described by a space-charge-limited conduction model which accounted for ohmic behavior at low applied electric fields, and transitioned to a space-charge-limited regime at higher fields. Hole mobilities and free carrier concentrations were calculated for both polymers following these methods. Photovoltaic devices were investigated by monitoring electrical responses to exposure to the solar spectrum.

Temperature dependent behavior of mobility was investigated for MEH-PPV based devices using these space-charge-limited conduction models. Hole mobility was shown to vary across eight orders of magnitude as temperature was monitored from 77 K

to room temperature. The results were found to be in good agreement with a previously suggested Arrhenius behavior [63]. However, the activation energy determined for this work was found to be approximately half that reported in [63]. This reduction suggests that the energy required for carrier hopping is reduced in the nanostructure, contributing to the observed enhancement of mobility and indicative of confinement-induced molecular ordering.

Solvent dependence of electronic and optical properties were also examined. Solvent choice was shown to significantly affect the carrier mobility in MEH-PPV, while those measured in various P3HT sample groups showed little change. For example, MEH-PPV nanotubes created by solution-based template wetting from tetrahydrofuran solutions exhibited mobilities that were three orders of magnitude higher than those commonly observed in thin films of the material [40, 116]. The lack of change in P3HT-based samples is likely due to its rigid structure and high degree of self-ordering. Flory-Huggins analysis of polymer solutions suggests that solvents which tend to straighten MEH-PPV the most produced higher mobilities, with the exception of chlorobenzene, as discussed in Chapter 5. It is probable that the MEH-PPV system takes on an ordered structure similar to that observed in P3HT films, where the polymer backbones align face-on, when straight molecules are incorporated into the nanopore.

The effects of impurities in P3HT were examined by fractionating the polymer using a series of Soxhlet extractions. A method for determining appropriate extraction process was reviewed, and an expanded variation was shown to accurately predict the extraction process. Solutions created from various fractions of the extraction process were used to create nanotube-based electronic devices, and carrier transport properties

were examined. It was found that mobility could be improved by using the most pure fraction of material, which is obtained by extraction in dichloromethane.

The highest mobilities observed in MEH-PPV were on the order of those for P3HT ( $10^{-3} \text{ cm}^2 \text{ V}^{-1} \text{ s}^{-1} \sim 10^{-2} \text{ cm}^2 \text{ V}^{-1} \text{ s}^{-1}$ ), and suggest that an upper limit to attainable carrier transport properties may exist. The behavior is also indicative of the molecular orientation of the molecules in the nanopore, pointing to a brush-like structure inside the pore, as was observed by Steinhart [99] for the template wetting process, in which the molecule length axis is oriented normal to the nanopore wall. This would produce an ordered structure that should behave similar to P3HT films in which  $\pi$ -orbital overlapping between the backbone of adjacent molecules is maximized. This structure is commonly reported to exhibit hole mobilities on the order of  $10^{-2} \text{ cm}^2 \text{ V}^{-1} \text{ s}^{-1}$  [6, 9, 136]. Similar mobilities were later noted for ordered polyfluorene films [36], confirming that  $10^{-2} \text{ cm}^2 \text{ V}^{-1} \text{ s}^{-1}$  may be the upper limit for interchain transport in soluble polymers. This limiting case is three orders of magnitude smaller than those observed for pentacene films [30, 33], but the intermolecular spacing of pentacene molecules is much smaller than for soluble polymers, where steric effects from polymer side chains prevent close interaction.

### **Future Work**

Future work on the topic should include a more in depth study of the optical behavior of the materials when incorporated into the nanoporous membrane. Better understanding of the optical processes in the material may provide greater insight into effective conjugation lengths and molecular ordering within the nanosystem. Molecular modeling of the effects of solvation and molecular confinement on electronic behavior of the material would provide further insight into the true physical phenomena responsible

for observations made in this work. Further, the use of experimental techniques including photoluminescence and ultraviolet-photoelectron spectroscopy could be used in conjunction with ultraviolet-visible spectroscopy to gain a more thorough knowledge of the complete electronic structure of these polymers when incorporated into the nanostructure.

**APPENDIX**

**SAMPLE GROUP CONTRIBUTION**

**CALCULATION**

### Group Contribution Calculations

The group contribution method utilizes tabulated, experimental data about specific chemical groups to estimate the behavior of more complex chemical structures.[114, 126, 127] For example, molar mass,  $M$ , and molar volume,  $\mathcal{V}$ , contributions from the various chemical groups that make up a molecule can be used to approximate  $M$  and  $\mathcal{V}$  for the molecule, by simply summing up the contributions of all components in the molecule. Table A.1 provides group contributions for  $M$ ,  $\mathcal{V}$ , and molar cohesive energy,  $U$ , required for group contribution calculations of the density and total solubility parameter for a methyl-terminated poly(3-hexylthiophene) dimer (as in Figure A.1). The group contribution calculation of a parameter or constant  $X$  is typically denoted  ${}^zX$ , and

$$X = \sum {}^zX. \quad (\text{A.1})$$

Table A.1. Group contributions to molar mass, molar volume, and cohesive energy following [114].

Quantity	Structural Group	Contribution Values from [114]			Sums		
		${}^zM$ (g mol <sup>-1</sup> )	${}^z\mathcal{V}$ (cm <sup>3</sup> mol <sup>-1</sup> )	${}^zU$ (J mol <sup>-1</sup> )	$M$ (g mol <sup>-1</sup> )	$\mathcal{V}$ (cm <sup>3</sup> mol <sup>-1</sup> )	$U$ (J mol <sup>-1</sup> )
4	-CH <sub>3</sub>	15.04	33.5	4710	60.16	134	18840
10	-CH <sub>2</sub> -	14.03	16.1	4940	140.3	161	49400
6	>C=	12.01	-5.5	4310	72.06	-33	25860
2	-CH=	13.02	13.5	4310	26.04	27	8620
2	-S-	32.1	12	14510	64.2	24	29020
2	5-atom ring closure	0	16	1050	0	32	2100
4	Ring conjugation (per $\pi$ -bond)	0	-2.2	1670	0	-8.8	6680
<b>Totals</b>					<b>362.76</b>	<b>336.2</b>	<b>140520</b>

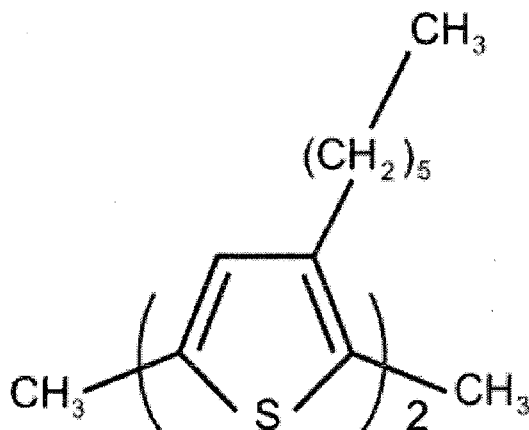


Figure A.1. Molecular structure of a P3HT dimer.

Using the sums of all contributions to  $M$ ,  $\mathcal{V}$ , and  $U$ , the density can be calculated following

$$\rho = \frac{M}{\mathcal{V}}, \quad (\text{A.2})$$

and the total solubility parameter,  $\delta_t$ , is found by

$$\delta_t = \sqrt{\frac{U}{\mathcal{V}}} \quad (\text{A.3})$$

yielding  $\rho = 1.079 \text{ g cm}^{-3}$  and  $\delta_t = 20.44 \text{ MPa}^{1/2}$ .

## REFERENCES

- [1] C. K. Chiang, C. R. Fincher, Y. W. Park, A. J. Heeger, H. Shirakawa, E. J. Louis, S. C. Gau, and A. G. MacDiarmid, "Electrical Conductivity in Doped Polyacetylene," *Physical Review Letters*, vol. 39, p. 1098, 1977.
- [2] C. K. Chiang, M. A. Druy, S. C. Gau, A. J. Heeger, E. J. Louis, A. G. MacDiarmid, Y. W. Park, and H. Shirakawa, "Synthesis of highly conducting films of derivatives of polyacetylene,  $(CH)_x$ ," *J. Am. Chem. Soc.*, vol. 100, pp. 1013-1015, 1978.
- [3] A. G. MacDiarmid and A. J. Heeger, "Organic Metals and Semiconductors: The Chemistry of Polyacetylene,  $CH_x$ , and its derivatives," *Synthetic Metals*, vol. 1, pp. 101-118, 1979.
- [4] A. Tsumura, H. Koezuka, and T. Ando, "Macromolecular electronic device: Field-effect transistor with a polythiophene thin film," *Applied Physics Letters*, vol. 49, pp. 1210-1212, 1986.
- [5] H. E. Katz and A. J. Lovinger, "A soluble and air-stable organic semiconductor with high electron mobility," *Nature*, vol. 404, p. 478, 2000.
- [6] C. D. Dimitrakopoulos and D. J. Masecaro, "Organic thin-film transistors: A review of recent advances," *IBM Journal of Research and Development*, vol. 45, pp. 11-27, 2001.
- [7] X. Wu, T.-A. Chen, and R. D. Rieke, "Synthesis of regioregular head-to-tail poly[3-(alkylthio)thiophenes]. A highly electroconductive polymer," *Macromolecules*, vol. 28, p. 2101, 1995.
- [8] M. Trznadel, A. Pron, M. Zagorska, R. Chrzaszcz, and J. Pielichowski, "Effect of molecular weight on spectroscopic and spectroelectrochemical properties of regioregular poly(3-hexylthiophene)," *Macromolecules*, vol. 31, pp. 5051-5058, 1998.

- [9] H. Sirringhaus, P. J. Brown, R. H. Friend, M. M. Nielsen, K. Bechgaard, B. M. W. Langeveld-Voss, A. J. H. Spiering, R. A. J. Janssen, E. W. Meijer, P. Herwig, and D. M. de Leeuw, "Two-dimensional charge transport in self-organized, high-mobility conjugated polymers," *Nature*, vol. 401, pp. 685-688, 1999.
- [10] J. H. Burroughes, D. D. C. Bradley, A. R. Brown, R. N. Marks, K. Mackay, R. H. Friend, P. L. Burns, and A. B. Holmes, "Light-emitting diodes based on conjugated polymers," *Nature*, vol. 347, pp. 539-541, 1990.
- [11] D. Braun and A. J. Heeger, "Visible light emission from semiconducting polymer diodes," *Applied Physics Letters*, vol. 58, pp. 1982-1984, 1991.
- [12] G. Yu and C. Zhang, "Dual-function semiconducting polymer devices: Light-emitting and photodetecting diodes," *Applied Physics Letters*, vol. 64, p. 1540, 1994.
- [13] R. N. Marks, J. J. M. Halls, D. D. C. Bradley, R. H. Friend, and A. B. Holmes, "Photovoltaic response in poly(p-phenylene vinylene) thin-film devices," *Journal of Physics Condensed Matter*, vol. 6, pp. 1379-1394, 1994.
- [14] M. Granstrom, K. Petritsch, A. C. Arias, A. Lux, M. R. Andersson, and R. H. Friend, "Laminated fabrication of polymeric photovoltaic diodes," *Nature*, vol. 395, pp. 257-260, 1998.
- [15] A. Assadi, C. Svensson, M. Willander, and O. Inganas, "Field-effect mobility of poly(3-hexylthiophene)," *Applied Physics Letters*, vol. 53, pp. 195-197, 1988.
- [16] Z. Bao, Y. Feng, A. Dodabalapur, and V. R. Raju, "High-Performance Plastic Transistors Fabricated by Printing Techniques," *Chemistry of Materials*, vol. 9, p. 1299, 1997.
- [17] J. M. Shaw and P. F. Seidler, "Organic electronics: Introduction," *IBM Journal of Research and Development*, vol. 45, pp. 3-8, 2001.
- [18] S. R. Forrest, "The path to ubiquitous and low-cost organic electronic appliances on plastic," *Nature*, vol. 428, pp. 911-918, 2004.

- [19] R. J. Visser, "Application of polymer light-emitting materials in light-emitting diodes, backlights and displays," *Philips Journal of Research*, vol. 51, pp. 467-477, 1998.
- [20] J. H. Schon, C. Kloc, and B. Batlogg, "Perylene: A promising organic field-effect transistor material," *Applied Physics Letters*, vol. 77, pp. 3776-3778, 2000.
- [21] A. L. Briseno, S. C. B. Mannsfeld, P. J. Shamberger, F. S. Ohuchi, Z. Bao, S. A. Jenekhe, and Y. Xia, "Self-Assembly, Molecular Packing, and Electron Transport in n-Type Polymer Semiconductor Nanobelts," *Chem. Mater.*, vol. 20, pp. 4712-4719, 2008.
- [22] L.-L. Chua, J. Zaumseil, J.-F. Chang, E. C. W. Ou, P. K. H. Ho, H. Sirringhaus, and R. H. Friend, "General observation of n-type field-effect behaviour in organic semiconductors," *Nature*, vol. 434, pp. 194-199, 2005.
- [23] W. E. Howard and O. F. Prache, "Microdisplays based upon organic light-emitting diodes," *IBM Journal of Research and Development*, vol. 45, pp. 115-127, 2001.
- [24] P. W. M. Blom and M. J. M. De Jong, "Device operation of polymer light-emitting diodes," *Philips Journal of Research*, vol. 51, pp. 479-494, 1998.
- [25] K. M. Coakley and M. D. McGehee, "Conjugated Polymer Photovoltaic Cells," *Chem. Mater.*, vol. 16, pp. 4533-4542, 2004.
- [26] N. Karl, "Introduction," in *Organic Electronic Materials: Conjugated Polymers and Low Molecular Weight Organic Solids*, R. Farchioni and G. Grosso, Eds. Berlin: Springer-Verlag, 2001, pp. 215-239.
- [27] R. H. Friend, R. W. Gymer, A. B. Holmes, J. H. Burroughes, R. N. Marks, C. Taliani, D. D. C. Bradley, D. A. Dos Santos, J. L. Bredas, M. Logdlund, and W. R. Salaneck, "Electroluminescence in conjugated polymers," *Nature*, vol. 397, pp. 121-128, 1999.
- [28] J. Paloheimo, H. Stubb, P. Yli-Lahti, and P. Kuivalainen, "Field-effect conduction in polyalkylthiophenes," *Synthetic Metals*, vol. 41, pp. 563-566, 1991.

- [29] S. F. Nelson, Y. Y. Lin, D. J. Gundlach, and T. N. Jackson, "Temperature-independent transport in high-mobility pentacene transistors," *Applied Physics Letters*, vol. 72, 1998.
- [30] I. Kyriassis, C. D. Dimitrakopoulos, and S. Purushothaman, "High-performance bottom electrode organic thin-film transistors," *IEEE Transactions on Electron Devices*, vol. 48, pp. 1060-1064, 2001.
- [31] V. Capek and I. Muzikante, "Electronic States in Organic Molecular Crystals," in *Organic Electronic Materials: Conjugated Polymers and Low Molecular Weight Organic Solids*, R. Farchioni and G. Grosso, Eds. Berlin: Springer-Verlag, 2001, pp. 241-282.
- [32] M. Steinhart, J. H. Wendorff, A. Greiner, R. B. Wehrspohn, K. Nielsch, J. Schilling, J. Choi, and U. Gosele, "Polymer nanotubes by wetting of ordered porous templates," *Science*, vol. 296, p. 1997, 2002.
- [33] J. H. Schon, S. Berg, C. Kloc, and B. Batlogg, "Ambipolar Pentacene Field-Effect Transistors and Inverters," *Science*, vol. 287, p. 1022, 2000.
- [34] J. McMurry, *Organic Chemistry*. Pacific Grove: Brooks/Cole, 1999.
- [35] Y.-S. Chen and H.-F. Meng, "Intrachain carrier transport in conjugated polymer with structural and chemical defects," *Physical Review B*, vol. 66, p. 035202, 2002.
- [36] H. Sirringhaus, R. J. Wilson, R. H. Friend, M. Inbasekaran, W. Wu, E. P. Woo, M. Grell, and D. D. C. Bradley, "Mobility enhancement in conjugated polymer field-effect transistors through chain alignment in a liquid-crystalline phase," *Applied Physics Letters*, vol. 77, pp. 406-408, 2000.
- [37] S. M. Sze and K. K. Ng, *Physics of Semiconductor Devices*. Hoboken, NJ: John Wiley & Sons, Inc., 2007.
- [38] B. G. Streetman and S. Banerjee, *Solid State Electronic Devices*, Fifth ed. Upper Saddle River, New Jersey: Prentice Hall, 2000.

- [39] Z. Bao, A. Dodabalapur, and A. J. Lovinger, "Soluble and processable regioregular poly(3-hexylthiophene) for thin film field-effect transistor applications with high mobility," *Applied Physics Letters*, vol. 69, p. 4108, 1996.
- [40] I. H. Campbell, D. L. Smith, C. J. Neef, and J. P. Ferraris, "Consistent time-of-flight mobility measurements and polymer light-emitting diode current-voltage," *Applied Physics Letters*, vol. 74, p. 2809, 1999.
- [41] I. H. Campbell, P. S. Davids, D. L. Smith, N. N. Barashkov, and J. P. Ferraris, "Schottky energy barrier dependence of charge injection in organic light-emitting diodes," *Applied Physics Letters*, vol. 72, pp. 1863-1865, 1998.
- [42] P. W. M. Blom, M. J. M. de Jong, and J. J. M. Vlegaar, "Electron and hole transport in poly(p-phenylene vinylene) devices," *Applied Physics Letters*, vol. 68, p. 3308, 1996.
- [43] I. D. Parker, "Carrier tunneling and device characteristics in polymer light-emitting diodes," *Journal of Applied Physics*, vol. 75, pp. 1656-1666, 1994.
- [44] H. Antoniadis, M. A. Abkowitz, and B. R. Hsieh, "Carrier deep-trapping mobility-lifetime products in poly(p-phenylene vinylene)," *Applied Physics Letters*, vol. 65, p. 2030, 1994.
- [45] G. G. Malliaras, J. R. Salem, P. J. Brock, and C. Scott, "Electrical characteristics and efficiency of single-layer organic light-emitting diodes," *Physical Review B*, vol. 58, p. R13411, 1998.
- [46] A. J. Campbell, M. S. Weaver, D. G. Lidzey, and D. D. C. Bradley, "Bulk limited conduction in electroluminescent polymer devices," *Journal of Applied Physics*, vol. 84, p. 6737, 1998.
- [47] I. H. Campbell, T. W. Hagler, D. L. Smith, and J. P. Ferraris, "Direct measurement of conjugated polymer electronic excitation energies using metal/polymer/metal structures," *Physical Review Letters*, vol. 76, p. 1900, 1996.
- [48] M. Onoda, K. Tada, A. A. Zakhidov, and K. Yoshino, "Photoinduced charge separation in photovoltaic cell with heterojunction of p- and n-type conjugated polymers," *Thin Solid Films*, vol. 331, pp. 76-81, 1998.

- [49] P. R. Emtage and J. J. O'Dwyer, "Richardson-Schottky Effect in Insulators," *Physical Review Letters*, vol. 16, p. 356, 1966.
- [50] C. D. Child, "Discharge From Hot CaO," *Physical Review (Series I)*, vol. 32, p. 492, 1911.
- [51] N. F. Mott and R. W. Gurney, *Electronic Processes in Ionic Crystals*, Second ed.: Oxford University Press, 1948.
- [52] A. Rose, "Space-Charge-Limited Currents in Solids," *Physical Review*, vol. 97, p. 1538, 1955.
- [53] R. W. Smith and A. Rose, "Space-Charge-Limited Currents in Single Crystals of Cadmium Sulfide," *Physical Review*, vol. 97, p. 1531, 1955.
- [54] W. Shockley and R. C. Prim, "Space-Charge Limited Emission in Semiconductors," *Physical Review*, vol. 90, p. 753, 1953.
- [55] G. C. Dacey, "Space-Charge Limited Hole Current in Germanium," *Physical Review*, vol. 90, p. 759, 1953.
- [56] M. A. Lampert, "Simplified Theory of Space-Charge-Limited Currents in an Insulator with Traps," *Physical Review*, vol. 103, p. 1648, 1956.
- [57] Z. Chiguvare, J. Parisi, and V. Dyakonov, "Current limiting mechanisms in indium-tin-oxide/poly(3-hexylthiophene)/aluminum thin film devices," *Journal of Applied Physics*, vol. 94, pp. 2440-2448, 2003.
- [58] D. Chirvase, Z. Chiguvare, M. Knipper, J. Parisi, V. Dyakonov, and J. C. Hummelen, "Electrical and optical design and characterisation of regioregular poly(3-hexylthiophene-2,5-diyl)/fullerene-based heterojunction polymer solar cells," *Synthetic Metals*, vol. 138, pp. 299-304, 2003.
- [59] C. R. Crowell and S. M. Sze, "Current transport in metal-semiconductor barriers," *Solid State Electronics*, vol. 9, pp. 1035-1048, 1966.
- [60] P. S. Davids, I. H. Campbell, and D. L. Smith, "Device model for single carrier organic diodes," *Journal of Applied Physics*, vol. 82, pp. 6319-6325, 1997.

- [61] P. W. M. Blom, M. J. M. De Jong, and M. G. Van Munster, "Electric-field and temperature dependence of the hole mobility in poly(p-phenylene vinylene)," *Physical Review B: Condensed Matter*, vol. 55, p. 656, 1997.
- [62] V. R. Nikitenko, H. Heil, and H. von Seggern, "Space-charge limited current in regioregular poly-3-hexyl-thiophene," *Journal of Applied Physics*, vol. 94, pp. 2480-2485, 2003.
- [63] P. W. M. Blom and M. J. M. de Jong, "Electrical characterization of polymer light-emitting diodes," *IEEE Journal on Selected Topics in Quantum Electronics*, vol. 4, pp. 105-112, 1998.
- [64] G. G. Malliaras and J. G. Scott, "Roles of injection and mobility in organic light emitting diodes," *Journal of Applied Physics*, vol. 83, pp. 5399-5403, 1998.
- [65] P. W. M. Blom, D. W. Black, and M. C. J. M. Vissenberg, "Contact-Limited Hole Current in Poly(p-phenylenevinylene)," in *Organic Electronic Materials: Conjugated Polymers and Low Molecular Weight Organic Solids*, R. Farchioni and G. Grosso, Eds. Berlin: Springer-Verlag, 2001, pp. 505-524.
- [66] P. N. Murgatroyd, "Theory of space-charge-limited current enhanced by Frenkel effect," *J. Phys. D: Appl. Phys.*, vol. 3, pp. 152-157, 1970.
- [67] S. Iijima, "Helical microtubules of graphitic carbon," *Nature*, vol. 354, p. 56, 1991.
- [68] M. Steinhart, R. B. Wehrspohn, U. Gosele, and J. H. Wendorff, "Nanotubes by template wetting: A modular assembly system," *Angewandte Chemie - International Edition*, vol. 43, pp. 1334-1344, 2004.
- [69] M. Steinhart, J. H. Wendorff, and R. B. Wehrspohn, "Nanotubes à la Carte: Wetting of Porous Templates," *ChemPhysChem*, vol. 4, pp. 1171-1176, 2003.
- [70] M. Steinhart, S. Murano, A. K. Schaper, T. Ogawa, M. Tsuji, U. Gosele, C. Weder, and J. H. Wendorff, "Morphology of polymer/liquid-crystal nanotubes: Influence of confinement," *Advanced Functional Materials*, vol. 15, pp. 1656-1664, 2005.

- [71] D. H. Reneker and I. Chun, "Nanometre diameter fibres of polymer, produced by electrospinning," *Nanotechnology*, vol. 7, pp. 216-223, 1996.
- [72] C. R. Martin, "Nanomaterials: a membrane-based synthetic approach," *Science*, vol. 266, pp. 1961-1966, 1994.
- [73] A. Formhals, "Process and Apparatus for Preparing Artificial Threads," U. S. P. Office, Ed. Germany: Scriber-Gastell, R., 1934.
- [74] D. Li, A. Babel, S. A. Jenekhe, and Y. Xia, "Nanofibers of conjugated polymers prepared by electrospinning with a two-capillary spinneret," *Advanced Materials*, vol. 16, pp. 2062-2066, 2004.
- [75] S. Megelski, J. S. Stephens, D. B. Chase, and J. F. Rabolt, "Micro- and Nanostructured Surface Morphology on Electrospun Polymer Fibers," *Macromolecules*, vol. 35, pp. 8456-8466, 2002.
- [76] H. Hou, Z. Jun, A. Reuning, A. Schaper, J. H. Wendorff, and A. Greiner, "Poly(p-xylylene) Nanotubes by Coating and Removal of Ultrathin Polymer Template Fibers," *Macromolecules*, vol. 35, pp. 2429-2431, 2002.
- [77] A. L. Yarin, S. Koombhongse, and D. H. Reneker, "Bending instability in electrospinning of nanofibers," *Journal of Applied Physics*, vol. 89, p. 3018, 2001.
- [78] D. Sun, C. Chang, S. Li, and L. Lin, "Near-Field Electrospinning," *Nano Lett.*, vol. 6, pp. 839-842, 2006.
- [79] A. Babel, D. Li, Y. Xia, and S. A. Jenekhe, "Electrospun nanofibers of blends of conjugated polymers: Morphology, optical properties, and field-effect transistors," *Macromolecules*, vol. 38, pp. 4705-4711, 2005.
- [80] C. R. Martin, "Membrane-Based Synthesis of Nanomaterials," *Chem. Mater.*, vol. 8, pp. 1739-1746, 1996.
- [81] Z. Cai and C. R. Martin, "Electronically conductive polymer fibers with mesoscopic diameters show enhanced electronic conductivities," *J. Am. Chem. Soc.*, vol. 111, pp. 4138-4139, 1989.

- [82] W. Liang and C. R. Martin, "Template-synthesized polyacetylene fibrils show enhanced supermolecular order," *J. Am. Chem. Soc.*, vol. 112, pp. 9666-9668, 1990.
- [83] C. R. Martin, L. S. Van Dyke, Z. Cai, and W. Liang, "Template synthesis of organic microtubules," *J. Am. Chem. Soc.*, vol. 112, pp. 8976-8977, 1990.
- [84] Z. Cai, J. Lei, W. Liang, V. Menon, and C. R. Martin, "Molecular and supermolecular origins of enhanced electric conductivity in template-synthesized polyheterocyclic fibrils. 1. Supermolecular effects," *Chem. Mater.*, vol. 3, pp. 960-967, 1991.
- [85] R. V. Parthasarathy and C. R. Martin, "Template-Synthesized Polyaniline Microtubules," *Chem. Mater.*, vol. 6, pp. 1627-1632, 1994.
- [86] S. Demoustier-Champagne, J. Duchet, and R. Legras, "Chemical and electrochemical synthesis of polypyrrole nanotubules," *Synthetic Metals*, vol. 101, pp. 20-21, 1999.
- [87] J. Joo, K. T. Park, B. H. Kim, M. S. Kim, S. Y. Lee, C. K. Jeong, J. K. Lee, D. H. Park, W. K. Yi, S. H. Lee, and K. S. Ryu, "Conducting polymer nanotube and nanowire synthesized by using nanoporous template: Synthesis, characteristics, and applications," *Synthetic Metals*, vol. 135-136, pp. 7-9, 2003.
- [88] B. H. Kim, M. S. Kim, K. T. Park, J. K. Lee, D. H. Park, J. Joo, S. G. Yu, and S. H. Lee, "Characteristics and field emission of conducting poly (3,4-ethylenedioxythiophene) nanowires," *Applied Physics Letters*, vol. 83, pp. 539-541, 2003.
- [89] J. L. Duvail, P. Retho, V. Fernandez, G. Louarn, P. Molinie, and O. Chauvet, "Effects of the Confined Synthesis on Conjugated Polymer Transport Properties," *J. Phys. Chem. B*, vol. 108, pp. 18552-18556, 2004.
- [90] L. Dauginet-De Pra and S. Demoustier-Champagne, "Investigation of the electronic structure and spectroelectrochemical properties of conductive polymer nanotube arrays," *Polymer*, vol. 46, pp. 1583-1594, 2005.
- [91] J. Joo, B. H. Kim, D. H. Park, H. S. Kim, D. S. Seo, J. H. Shim, S. J. Lee, K. S. Ryu, K. Kim, J. I. Jin, T. J. Lee, and C. J. Lee, "Fabrication and applications of

- conducting polymer nanotube, nanowire, nanohole, and double wall nanotube," *Synthetic Metals*, vol. 153, pp. 313-316, 2005.
- [92] B. H. Kim, D. H. Park, J. Joo, S. G. Yu, and S. H. Lee, "Synthesis, characteristics, and field emission of doped and de-doped polypyrrole, polyaniline, poly(3,4-ethylenedioxythiophene) nanotubes and nanowires," *Synthetic Metals*, vol. 150, pp. 279-284, 2005.
- [93] C. J. Brumlik and C. R. Martin, "Template synthesis of metal microtubules," *J. Am. Chem. Soc.*, vol. 113, pp. 3174-3175, 1991.
- [94] C. J. Brumlik, C. R. Martin, and K. Tokuda, "Microhole array electrodes based on microporous alumina membranes," *Anal. Chem.*, vol. 64, pp. 1201-1203, 1992.
- [95] C. A. Foss, G. L. Hornyak, J. A. Stockert, and C. R. Martin, "Optical properties of composite membranes containing arrays of nanoscopic gold cylinders," *J. Phys. Chem.*, vol. 96, pp. 7497-7499, 1992.
- [96] C. A. Foss, G. L. Hornyak, J. A. Stockert, and C. R. Martin, "Template-Synthesized Nanoscopic Gold Particles: Optical Spectra and the Effects of Particle Size and Shape," *J. Phys. Chem.*, vol. 98, pp. 2963-2971, 1994.
- [97] J. D. Klein, R. D. Herrick, D. Palmer, M. J. Sailor, C. J. Brumlik, and C. R. Martin, "Electrochemical fabrication of cadmium chalcogenide microdiode arrays," *Chem. Mater.*, vol. 5, pp. 902-904, 1993.
- [98] D. H. Park, B. H. Kim, M. K. Jang, K. Y. Bae, S. J. Lee, and J. Joo, "Synthesis and characterization of polythiophene and poly (3-methylthiophene) nanotubes and nanowires," *Synthetic Metals*, vol. 153, pp. 341-344, 2005.
- [99] M. Steinhart, S. Senz, R. B. Wehrspohn, U. Gosele, and J. H. Wendorff, "Curvature-Directed Crystallization of Poly(vinylidene difluoride) in Nanotube Walls," *Macromolecules*, vol. 36, pp. 3646-3651, 2003.
- [100] C. Barrett, D. Iacopino, D. O'Carroll, G. De Marzi, D. A. Tanner, A. J. Quinn, and G. Redmond, "Synthesis of Pentacene Nanotubes by Melt-Assisted Template Wetting," *Chemistry of Materials*, vol. 19, pp. 338-340, 2007.

- [101] J. Cannon, S. Selmic, and S. Gold, "Optoelectronic Polymer Nanowires by Templating Process," in *AIChE Annual Meeting*, San Francisco, CA, 2006.
- [102] G. A. O'Brien, A. J. Quinn, D. A. Tanner, and G. Redmond, "A single polymer nanowire photodetector," *Advanced Materials*, vol. 18, pp. 2379-2383, 2006.
- [103] S. Moynihan, D. Iacopino, D. O'Carroll, P. Lovera, and G. Redmond, "Template Synthesis of Highly Oriented Polyfluorene Nanotube Arrays," *Chemistry of Materials*, vol. 20, pp. 996-1003, 2008.
- [104] S. Schlitt, A. Greiner, and J. H. Wendorff, "Cylindrical Polymer Nanostructures by Solution Template Wetting," *Macromolecules*, vol. 41, pp. 3228-3234, 2008.
- [105] S. Hotta, S. D. D. V. Rughooputh, A. J. Heeger, and F. Wudl, "Spectroscopic studies of soluble poly(3-alkylthienylenes)," *Macromolecules*, vol. 20, pp. 212-215, 1987.
- [106] Y. Furukawa, A. Sakamoto, and M. Tasumi, "Raman and infrared studies on the molecular structures of poly(1,4-phenylenevinylene) and poly(2,5-thienylenevinylene)," *The Journal of Physical Chemistry*, vol. 93, pp. 5354-5356, 1989.
- [107] S. Shi and F. Wudl, "Synthesis and characterization of a water-soluble poly(p-phenylenevinylene) derivative," *Macromolecules*, vol. 23, pp. 2119-2124, 1990.
- [108] A. W. Adamson and A. P. Gast, *Physical Chemistry of Surfaces*, Sixth ed. New York: Wiley-Interscience, 1997.
- [109] P.-G. de Gennes, F. Brochard-Wyart, and D. Quere, *Capillarity and wetting phenomena: drops, bubbles, pearls, waves*. New York: Springer, 2003.
- [110] J. S. Rowlinson and B. Widom, *Molecular Theory of Capillarity*. Oxford: Clarendon Press, 1982.
- [111] K. Grundke, "Wetting, Spreading and Penetration," in *Handbook of Applied Surface and Colloid Chemistry*. vol. 2, K. Holmberg, Ed.: John Wiley & Sons, Ltd, 2002, pp. 119-142.

- [112] D. Ausserré, A. M. Picard, and L. Léger, "Existence and Role of the Precursor Film in the Spreading of Polymer Liquids," *Physical Review Letters*, vol. 57, p. 2671, 1986.
- [113] L. Leger, M. Erman, A. M. Guinet-Picard, D. Ausserre, and C. Strazielle, "Precursor Film Profiles of Spreading Liquid Drops," *Physical Review Letters*, vol. 60, p. 2390, 1988.
- [114] A. F. M. Barton, *CRC Handbook of Solubility Parameters and Other Cohesion Parameters*, 2nd ed. Boca Raton: CRC Press, 1991.
- [115] D. K. Chambers, B. Raut, D. Qi, C. B. O'Neal, and S. Selmic, "The effect of helium plasma etching on polymer-based electronic devices," *Thin Solid Films*, p. Accepted for publication., 2009.
- [116] I. H. Campbell, D. L. Smith, C. J. Neef, and J. P. Ferraris, "Charge transport in polymer light-emitting diodes at high current density," *Applied Physics Letters*, vol. 75, pp. 841-843, 1999.
- [117] F. Khatkhatay and S. Selmic, "Unpublished results.," 2007.
- [118] M. A. Green, *Solar Cells: Operating Principles, Technology and System Applications*: Prentice Hall, 1982.
- [119] B. J. Schwartz, "CONJUGATED POLYMERS AS MOLECULAR MATERIALS: How Chain Conformation and Film Morphology Influence Energy Transfer and Interchain Interactions," *Annual Review of Physical Chemistry*, vol. 54, pp. 141-172, 2003.
- [120] S. Lee, J. Y. Lee, and H. Lee, "Solvent effects on the characteristics of conductive and luminescent polymers," *Synthetic Metals*, vol. 101, pp. 248-249, 1999.
- [121] J. A. Merlo and C. D. Frisbie, "Field effect transport and trapping in regioregular polythiophene nanofibers," *Journal of Physical Chemistry B*, vol. 108, pp. 19169-19179, 2004.
- [122] X. T. Hao, T. Hosokai, N. Mitsuo, S. Kera, K. K. Okudaira, K. Mase, and N. Ueno, "Control of the interchain  $\pi$ - $\pi$  interaction and electron density

distribution at the surface of conjugated poly(3-hexylthiophene) thin films," *Journal of Physical Chemistry B*, vol. 111, pp. 10365-10372, 2007.

- [123] C. K. Lee, C. C. Hua, and S. A. Chen, "Single-chain and aggregation properties of semiconducting polymer solutions investigated by coarse-grained Langevin dynamics simulation," *Journal of Physical Chemistry B*, vol. 112, pp. 11479-11489, 2008.
- [124] R. Traiphol, N. Charoenthai, T. Srihirin, T. Kerdcharoen, T. Osotchan, and T. Maturros, "Chain organization and photophysics of conjugated polymer in poor solvents: Aggregates, agglomerates and collapsed coils," *Polymer*, vol. 48, pp. 813-826, 2007.
- [125] P. Derosa, "Unpublished results.," 2009.
- [126] J. M. Prausnitz, R. N. Lichtenhaler, and E. G. Azevedo, *Molecular Thermodynamics of Fluid-Phase Equilibria*, Third ed. Upper Saddle River, New Jersey: Prentice Hall, 1999.
- [127] E. A. Grulke, *Polymer Process Engineering*, First ed. Englewood Cliffs, New Jersey: Prentice Hall, 1994.
- [128] L. J. Fitzpatrick and J. R. Dean, "Extraction Solvent Selection in Environmental Analysis," *Analytical Chemistry*, vol. 74, pp. 74-79, 2002.
- [129] T. Yamamoto, A. Morita, Y. Miyazaki, T. Maruyama, H. Wakayama, Z. H. Zhou, Y. Nakamura, T. Kanbara, S. Sasaki, and K. Kubota, "Preparation of pi-conjugated poly(thiophene-2,5-diyl), poly(p-phenylene), and related polymers using zerovalent nickel complexes. Linear structure and properties of the pi-conjugated polymers," *Macromolecules*, vol. 25, pp. 1214-1223, 1992.
- [130] R. D. McCullough, S. Tristram-Nagle, S. P. Williams, R. D. Lowe, and M. Jayaraman, "Self-orienting head-to-tail poly(3-alkylthiophenes): new insights on structure-property relationships in conducting polymers," *J. Am. Chem. Soc.*, vol. 115, pp. 4910-4911, 1993.
- [131] R. D. Rieke and T. A. Chen, "Regiocontrolled synthesis utilizing highly reactive zinc leads to poly(alkylthiophene) with the highest regioregularity, the smallest band gap, and the highest intrinsic conductivity," *Polymer Preprints, Division of Polymer Chemistry, American Chemical Society*, vol. 34, p. 426, 1993.

- [132] T. A. Chen, X. Wu, and R. D. Rieke, "Regiocontrolled synthesis of poly(3-alkylthiophenes) mediated by Rieke zinc. Their characterization and solid-state properties," *Journal of the American Chemical Society*, vol. 117, p. 233, 1995.
- [133] S. Samitsu, T. Shimomura, S. Heike, T. Hashizume, and K. Ito, "Effective production of poly(3-alkylthiophene) nanofibers by means of whisker method using anisole solvent: Structural, optical, and electrical properties," *Macromolecules*, vol. 41, pp. 8000-8010, 2008.
- [134] K. M. Scholsky, "Fractionation of low molecular weight polyethylene by high-pressure Soxhlet extraction," *Journal of Applied Polymer Science*, vol. 47, pp. 1633-1641, 1993.
- [135] R. Paukkeri and A. Lehtinen, "Fractionation of polypropylenes using Soxhlet extraction methods," *Polymer*, vol. 35, pp. 1673-1679, 1994.
- [136] A. Babel and S. A. Jenekhe, "Morphology and field-effect mobility of charge carriers in binary blends of poly(3-hexylthiophene) with poly[2-methoxy-5-(2-ethylhexoxy)-1,4-phenylenevinylene] and polystyrene," *Macromolecules*, vol. 37, pp. 9835-9840, 2004.